



Qualification of innovative floating substructures for 10MW wind turbines and water depths greater than 50m

Project acronym LIFES50+
Grant agreement 640741
Collaborative project
Start date 2015-06-01
Duration 47 months

Deliverable D4.8 Validation of advanced models and methods for cascading into simpler models

Lead Beneficiary DTU
Due date 2018-12-31
Delivery date 2019-01-02
Dissemination level Public
Status Final
Classification Unrestricted

Keywords Numerical models, advanced, validation, floating wind turbines
Company document number [Click here to enter text.](#)



The research leading to these results has received funding from the European Union Horizon2020 programme under the agreement H2020-LCE-2014-1-640741.

Disclaimer

The content of the publication herein is the sole responsibility of the publishers and it does not necessarily represent the views expressed by the European Commission or its services.

While the information contained in the documents is believed to be accurate, the authors(s) or any other participant in the LIFES50+ consortium make no warranty of any kind with regard to this material including, but not limited to the implied warranties of merchantability and fitness for a particular purpose.

Neither the LIFES50+ Consortium nor any of its members, their officers, employees or agents shall be responsible or liable in negligence or otherwise howsoever in respect of any inaccuracy or omission herein.

Without derogating from the generality of the foregoing neither the LIFES50+ Consortium nor any of its members, their officers, employees or agents shall be liable for any direct or indirect or consequential loss or damage caused by or arising from any information advice or inaccuracy or omission herein.

Document information

Version	Date	Description
1	Click today	<p>Draft</p> <p>Prepared by Pegalajar-Jurado, A.; Madsen, F.J.; Sarlak, H.; Bredmose, H.; Lemmer, F.; Faerron-Guzman, R.; Borisade, F.; Kretschmer, M.</p> <p>Reviewed by Thys, M.; Andersen, H.S.; Marley, M.; Rodriguez-Arias, R.; Galvan, J.; Nava, V.</p> <p>Approved by Bredmose, H.</p>
2	Click today	<p>Final version submitted to project coordinator</p> <p>Prepared by Pegalajar-Jurado, A.; Madsen, F.J.; Sarlak, H.; Bredmose, H.; Lemmer, F.; Faerron-Guzman, R.; Borisade, F.; Kretschmer, M.</p> <p>Reviewed by Bredmose, H.</p> <p>Approved by Enter names</p>
3	2018-12-28	<p>Final version for QA before submission to EC</p> <p>Prepared by Pegalajar-Jurado, A.; Madsen, F.J.; Sarlak, H.; Bredmose, H.; Lemmer, F.; Faerron-Guzman, R.; Borisade, F.; Kretschmer, M.</p> <p>Reviewed by Jan Arthur Norbeck</p> <p>Approved by Petter Andreas Berthelsen</p>

Authors	Organization
Pegalajar-Jurado, A.	DTU
Madsen, F.J.	DTU
Sarlak, H.	DTU
Bredmose, H.	DTU
Lemmer, F.	USTUTT
Faerron-Guzman, R.	USTUTT
Borisade, F.	USTUTT
Kretschmer, M.	USTUTT

Contributors	Organization
Yu, W.	USTUTT
Müller, K.	USTUTT

Definitions & Abbreviations	
DoF	Degree of freedom
PSD	Power spectral density
QTF	Quadratic transfer function
DLC	Design load case
CFD	Computational fluid dynamics
VOF	Volume of fluid
RANS	Reynolds-averaged Navier-Stokes
MBS	Multi-body system
OMA	Operational modal analysis
RAO	Response-amplitude operator
FOWT	Floating offshore wind turbine
BEM	Blade-element momentum
GDW	Generalized dynamic wake

Executive Summary

The design process for floating wind turbine substructures can be aided by application of design models at different levels of fidelity. This is due to the generic proportionality between model accuracy and computational effort. The present deliverable of LIFES50+ focuses on the validation of advanced models developed in work package 4. The validation is made against model test data, mainly from the Ocean Basin tests within LIFES50+. The deliverable further gives examples of cascading (application) of results from the advanced models into models of lower fidelity.

The model validation consists of

- Validation of the inclusion of floater flexibility in dynamic response calculations in the HAWC2 aero-elastic model. The methods ability to predict response at the natural structural flexibility is demonstrated in a generic setup with a flexible monopile subjected to loads from steep waves.
- Validation of a second-order FAST model for the OO-Star Wind Floater Semi 10MW with full QTF quadratic wave forcing and damping calibration in the modal space. It is demonstrated that a good match can be obtained if a sea-state dependent damping calibration is applied. The second-order forcing of the Newman approximation is found to be generally smaller than the one obtained from full QTF analysis.
- Validation of an OpenFOAM hydrodynamic CFD setup for the OO-Star Wind Floater Semi 10MW. A good agreement is found for a heave decay test. A simplified mooring representation is developed and a further good match for surge motion in a regular wave case is shown.
- Validation of a second-order FAST model for the Nautilus-DTU10 floater with full QTF quadratic wave forcing. A damping approach based on calibrated Morison drag coefficients is utilized and a generally good match is found for pink noise tests. For larger sea states, the combined role of forcing and damping of the Morison drag term is found to prevent a good calibration for all degrees of freedom.
- Validation of an Ansys CFX hydrodynamic CFD setup for the Nautilus-DTU10 floater. Forced heave motion is utilized to compute added mass and damping coefficients. A good match with linear potential flow theory is found for the added mass. Free heave decay is compared to test results and the effect of viscous flow separation is discussed.
- Validation of an OMA (Operational Modal Analysis) based method for damping detection. The method is applied to the ocean basin tests of the Nautilus-DTU10 floater in combination with a QTF-driven second-order hydrodynamic model. The damping levels found by OMA agree well with those based on modal calibration for pink noise tests. Differences are found for the extreme sea states and are discussed in relation to the assumptions associated with OMA theory.
- Validation of a free vortex aerodynamic model against wind tunnel tests of POLIMI for a scaled model of the 10MW DTU reference wind turbine. Detailed comparison of aerodynamic damping from oscillatory tests are presented. It is found that the free vortex approach is generally more accurate than the BEM (Boundary Element Momentum) method.

Contents

1	Introduction	8
2	Validation of elastic modes against flexible monopile tests.....	10
2.1	Experimental Setup	10
2.2	Numerical Model Setup.....	11
2.3	Limitations of the study.....	11
2.4	Response in waves.....	12
2.5	Conclusions	15
3	Validation of second-order hydrodynamics in a state-of-the-art model of the OO-Star Wind Floater Semi 10MW	16
3.1	Introduction	16
3.2	Full second-order solution.....	16
3.3	Global linear damping from diagonal elements	17
3.4	Global linear damping from modal analysis	21
3.5	Discussion and conclusion	30
4	Validation of OpenFOAM CFD for the OO-Star Wind Floater Semi 10MW	31
4.1	Methodology of solving flow and body motion equations.....	31
4.2	Numerical set up.....	33
4.3	Selection of test cases.....	38
4.4	Concluding remarks	43
5	Validation of second-order hydrodynamics in a state-of-the-art model of the NAUTILUS-DTU10	44
5.1	Introduction	44
5.2	Comparison of decay tuned model for different hydrodynamics modelling approaches	47
5.3	Newman approximation and QTF results.....	48
5.4	Sensitivity of Morison drag coefficients in decay tests.....	50
5.5	Test 4210 Pink Noise – $H_s=2$ m, $T_p = [4.5,18]$ s	52
5.6	Test 6241 DLC1.6 – PM, $H_s = 7.7$ m, $T_p = 12.4$ s.....	54
5.7	Computational Time.....	58
5.8	Conclusion.....	59
5.9	Further work	59
6	Validation of CFX for the NAUTILUS-DTU10	61
6.1	Introduction	61
6.2	Simulation environment and setup	61
6.3	Forced oscillation tests	64
6.4	Free-decay test.....	72

6.5	Conclusions	76
7	Damping detection by Operational Modal Analysis for the NAUTILUS-DTU10.	77
7.1	Introduction	77
7.2	Environmental conditions.....	78
7.3	The numerical model.....	78
7.4	Results and discussion.....	85
7.5	Conclusions	91
8	Validation of aerodynamic models.....	93
8.1	Experimental Data Basis	93
8.2	Simulation Model and Setup	93
8.3	Model Check	94
8.4	Model Validation for Moving Platform	96
8.5	Identification of Phenomena.....	100
8.6	Simulation-Time.....	103
8.7	Summary of Aerodynamic validation	103
9	Conclusions	105
10	References	108

1 Introduction

Accurate design of floaters for offshore wind application can be aided by combination of numerical tools of different level of fidelity. This has been the basis for work package 4 of LIFES50+, illustrated in Figure 1. In pre-design efficient models with low CPU cost can speed up the initial design iterations, while the design validation must be carried out by state-of-the-art models of higher accuracy and CPU cost. In the design validation at component level, advanced models can be applied to provide details on load mechanisms at larger accuracy and CPU cost.

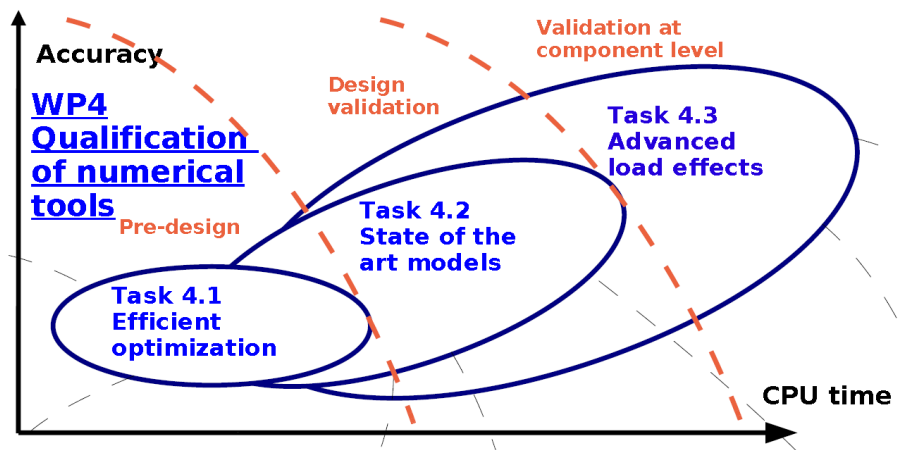


Figure 1: CPU-time versus accuracy for design models. Task division in LIFES50+ WP4.

Simplified models have been presented in D4.1 *Simplified numerical models for up-scaled design*, while State-of-the-art models have been presented in D4.5 *State-of-the-art models for the two public 10MW floater concepts*. Advanced models were presented in D4.7 *Models for advanced load effects and loads at component level*. The role of the present deliverable D4.8 *Validation of advanced models and methods for cascading into simpler models* is to present the validation of these advanced models against generic or experimental data from the LIFES50+ project. Further, the deliverable demonstrates methods for application of the advanced model results within models of lower CPU cost.

The validation of models is done in the following sections, for the following floaters and data sets:

Section	Model	Structure / data set
2	Elastic substructure deformation	Flexible monopile DHI-DTU Wave Loads data (2013)
3	Modal based damping vs diagonal damping matrices Newman vs full QTF	OO floater L50+ Sintef Ocean basin tests
4	OpenFOAM CFD for wave-driven platform motion	OO floater L50+ SINTEF Ocean basin tests
5	Second-order forcing Newman vs QTF. Morison-based damping	Nautilus floater L50+ SINTEF Ocean basin tests
6	Ansys CFX CFD for wave-driven platform motion	Nautilus floater L50+ SINTEF Ocean basin tests
7	Damping detection by Operational Modal Analysis and second-order hydrodynamics	Nautilus floater L50+ SINTEF Ocean basin tests
8	Free vortex method vs BEM	Scaled DTU 10MW rotor L50+ POLIMI wind tunnel tests

The methods for cascading are not described in isolated sections but are inherent of the model developments. They can be summarized as follows

Section	Model	Model levels
3,5	QTF vs Newman <ul style="list-style-type: none"> The Newman forcing model can be applied with same efficiency as linear forcing once its accuracy has been found to be sufficient 	Advanced -> State-of-the-art Advanced -> Simplified
3,5,7	Tuning of damping (modal, Morison, OMA) <ul style="list-style-type: none"> The results of the damping calibration and OMA detection method can be applied in simplified models 	Advanced -> State-of-the-art Advanced -> Simplified State-of-the-art -> Simplified
4,6	Hydrodynamic CFD <ul style="list-style-type: none"> The CFD models are applied for decay tests. The detected damping can potentially replace physical model tests for damping detection 	Advanced -> State-of-the-art Advanced -> Simplified
8	BEM and Free vortex method <ul style="list-style-type: none"> The aerodynamic analysis for forced motion can replace the wind tunnel tests and provide aerodynamic damping for simplified models with parameterized aerodynamic damping 	State-of-the-art -> Simplified Advanced -> Simplified

The report is structured around the sections outlined above. Sub-conclusions for each model validation are provided in each subsection. An overall summary with perspectives for further work is provided in section 9.

2 Validation of elastic modes against flexible monopile tests

The methodology to include substructure elasticity within dynamic calculations presented in D4.7 is validated here. Due to the lack of appropriate model scale floating wind turbine tests that include the elasticity of a floating substructure, the validation study was carried out considering a 1:80 scale model monopile dataset from the Wave Loads Project [1]. Whilst this study is limited in terms of validating the full extent of the proposed methodology, it enables a generic verification of the implementation of the super element and hydro-elastic modelling within HAWC2 and WAMIT.

The section is organized as follows: First a brief description of the experimental setup is given, followed by the numerical model setup and a discussion of the model limitations. Simulation results for two cases are then presented and discussed.

2.1 Experimental Setup

The 1:80 scale model flexible monopile was tested at DHI Denmark as part of the Wave Loads project [2]. Results and re-computations of the data set has been presented earlier as part of the Wave Loads project [1] and the OC5 project [3]. The wave basin setup consisted of the monopile installed on a sloping bed, as illustrated in Figure 2. The water depth at the wave maker was 0.78 metres and the water depth at the monopile for the load cases considered here was 0.51 metres, corresponding to 40.8 metres in prototype scale. Table 1 presents the model setup. The monopile was instrumented with a number of accelerometers placed at different heights, and a force gauge at the base. Further details may be found in [1].

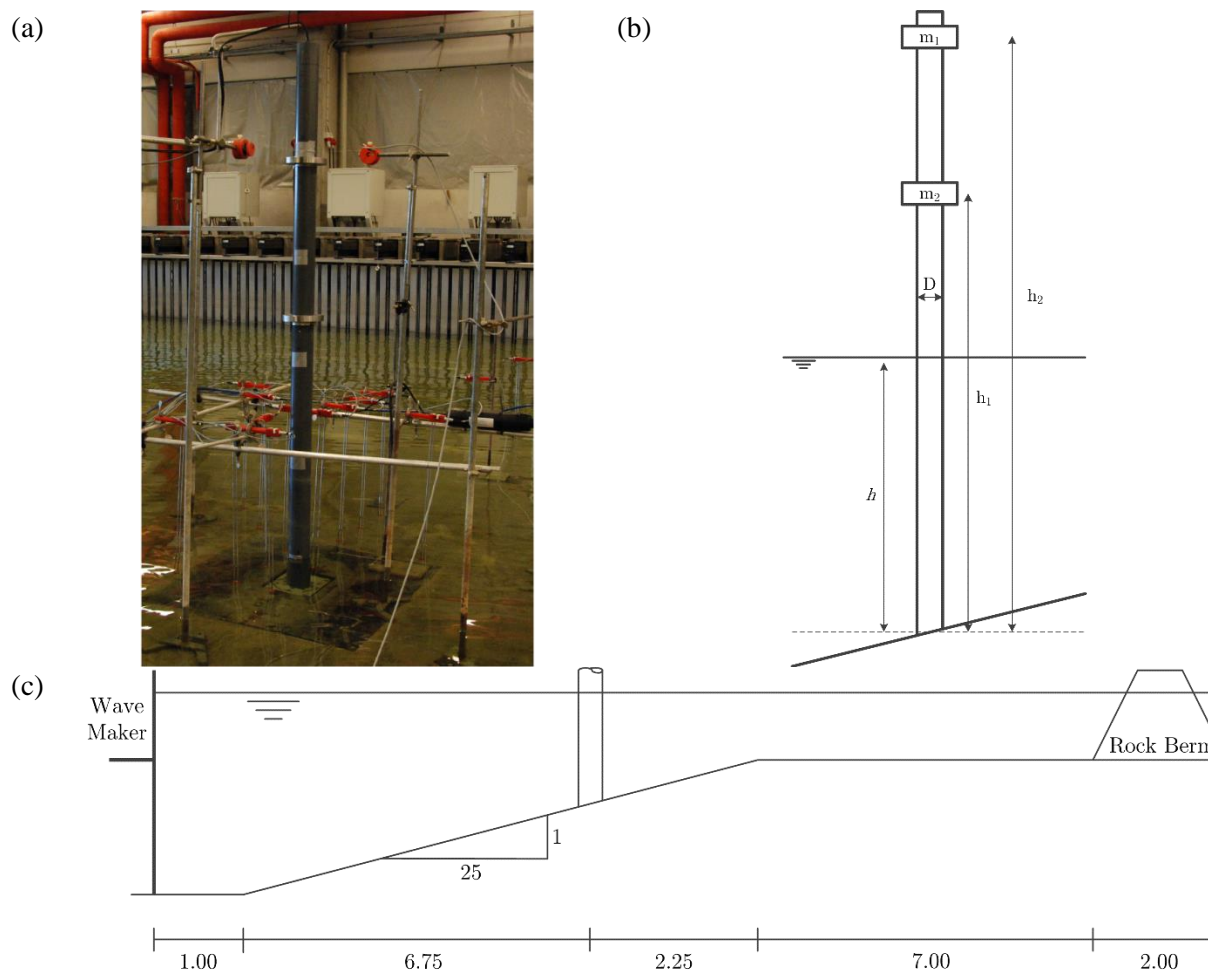


Figure 2: (a) Scale model monopile installed in the DHI Denmark wave basin; (b) Layout of the monopile; (c) side view of the wave basin

Table 1: Monopile characteristics

Parameter	Model Scale (1:80)	Prototype Scale
Diameter, D [m]	0.075	6.0
Wall thickness [cm]	0.18	14.4
Estimated EI [Nm ²]	1026	4.2×10^{10}
Estimated damping ratio [-]	0.017	0.017
Section density [kg/m]	0.64	4096
Monopile height [m]	2.0	160
m_1 [kg]	1.786	9.37×10^5
m_2 [kg]	1.784	9.36×10^5
h_1 [m]	1.6075	128.6
h_2 [m]	1.0875	87.0
f_1 [Hz]	2.5	0.28
f_2 [Hz]	18	2.0

2.2 Numerical Model Setup

The numerical model was set up following the methodology described in D4.7. First a beam-type finite element model of the model scale monopile was constructed in HAWC2, using the Morison equation and strip theory to represent hydrodynamic inertial characteristics. The solution of the eigenvalue problem of this model gave eigen frequencies that were in agreement with the measured natural frequencies corresponding to the first two bending modes. Due to the relative placement of these natural frequencies with respect to the wave frequency range (c.f. Table 1), only the first eigen mode was considered in the further analysis.

The first eigen mode identified in the first phase of the analysis, was then used in the framework of the HAWC2-flex WAMIT for time domain computations of the structural response. Note that the reduced order model of the monopile had 7 degrees of freedom (DOFs), namely the 6-rigid body DOFs and one flexible DOF. The 6-rigid body DOFs were constrained such that only the flexible DOF was free to vibrate within the dynamic calculations. When carrying out dynamic calculations, the measured wave elevation from the experiments was used as input to hydrodynamic load calculations. The WAMIT pre-computation defines linear transfer functions from the complex Fourier amplitudes of the waves to the forcing of the individual modes. In this way, the wave input is fully nonlinear with higher-harmonic frequency content. The force model, though, is linear, so all frequency content is converted to force by the linear transfer function. This limitation is discussed further below. The stresses can be obtained in post-processing by imposing the simulated response in the FEM model used in the first phase.

2.3 Limitations of the study

The simple setup of a monopile fixed to the sea bed was chosen due to a) its simple form and b) to the availability of data. No open data sets for flexible response of a floating wind turbine structure are available to the author's knowledge. The simple setup of the monopile has the advantage of easier interpretation of the results and limited uncertainty in model setup and calibration.

The validation of the solver for this setup, however, is also associated with a number of limitations:

- The experiments were made to study ringing and impulsive excitation of monopile turbines in storm waves. The natural frequency of the monopile (2Hz in model scale; 0.28 Hz in full scale) is thus outside of the primary wave range. The dynamic excitation of the structure is therefore

a result of nonlinear wave effects which are only partially covered in the model. The model is driven by the measured free surface elevation which does contain the fully nonlinear wave frequency content. This is next passed through the WAMIT generated linear transfer functions for modal forcing. This introduces in-completeness for the nonlinear wave content and is thus likely to lead to in-accurate results for the structural excitation.

- Linked to the linear basis of the WAMIT description, the force integration is only carried out up to the still water level and viscous drag loads are neglected. Also, this will lead to discrepancies in the forcing.

As a result, the present validation should be seen as a step on the path towards a full validation of the solver. Besides the nonlinear excitation loads, the model will also deflect quasi-statically to the external forcing and the model frame work will allow sectional loads to be determined. These sectional loads are a result of the external forcing and the predicted deflections. The comparison of them to the measured ones thus provides a first attempt for a model validation.

2.4 Response in waves

Three load cases were considered, namely one regular wave condition and two irregular wave conditions. Table 2 details the parameters for these wave conditions. All results are shown in terms of representative time series and power spectra. For the irregular wave cases, also exceedance probability curves for the shear force at sea bed are shown, obtained by a simple wave-by-wave analysis. For these exceedance probability curves, a low-pass filtering at 5 Hz was conducted prior to the peak extraction to avoid high-frequency oscillations.

Table 2: Environmental conditions

	Model Scale		Prototype Scale	
	H, H _s [m]	T, T _p [s]	H, H _s [m]	T, T _p [s]
Regular waves (R1)	0.100	1.565	8	14.0
Irregular waves (I1)	0.104	1.409	8.3	12.6
Irregular waves (I2)	0.138	1.565	11.0	14.0

2.4.1 Regular Waves R1

Figure 3 presents the in-line shear force at the monopile base for the regular waves R1 condition. From the time series of free surface elevation, a difference in the mean value is observed. This discrepancy is due to a non-zero mean of the measured signal, which was ignored by the numerical model.

For the shear force at the sea bed, a 25% difference in the PSD amplitude, equivalent to 14% difference in Fourier amplitude occurs. Here the difference is associated with an under-prediction in the HAWC2 results. This is likely due to the only linear hydrodynamic description that involves only hydrodynamic loading up to the still water level and neglects viscous drag loads.

Higher harmonics are excited due to higher harmonics present in the measured wave-elevation which is used as input.

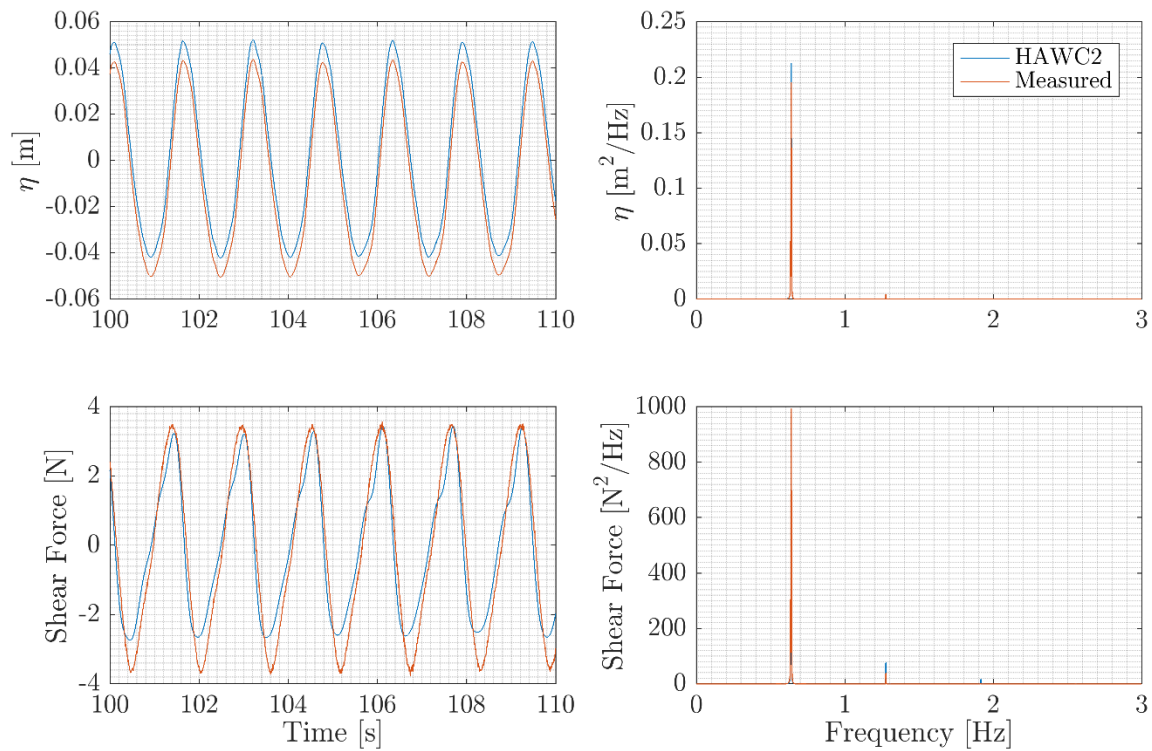


Figure 3: Wave elevation and shear force at the monopile base in the regular wave condition.

2.4.2 Irregular Waves I1

Figure 4 presents the in-line shear force at the monopile base for the irregular waves I1 condition. The comparison of wave elevation between HAWC2 and the measurements only differs by a mean offset similarly as for the R1 case.

From the spectral plot, HAWC2 tends to under-predict the shear force response about the peak wave frequency and over-predict the response at higher frequencies. The under-prediction could be due to the fact that HAWC2 only considers hydrodynamic loads up to the mean water level. The over-prediction cause is less clear – WAMIT includes diffraction effects that would be more pronounced at the higher frequencies and these effects should not be over-estimated by WAMIT. There could be some nonlinear damping in the measurements, although there is no clear physical indication to this in this frequency range.

In terms of the exceedance probability curves, the model is in fair agreement with the measurements. The shear force peaks are generally under-predicted by HAWC2, with the largest difference of 16.9% being at the lowest probability. This can be linked to the model limitations of incomplete nonlinear wave forcing description and the omission of loads above the still water level and the omission of drag loads.

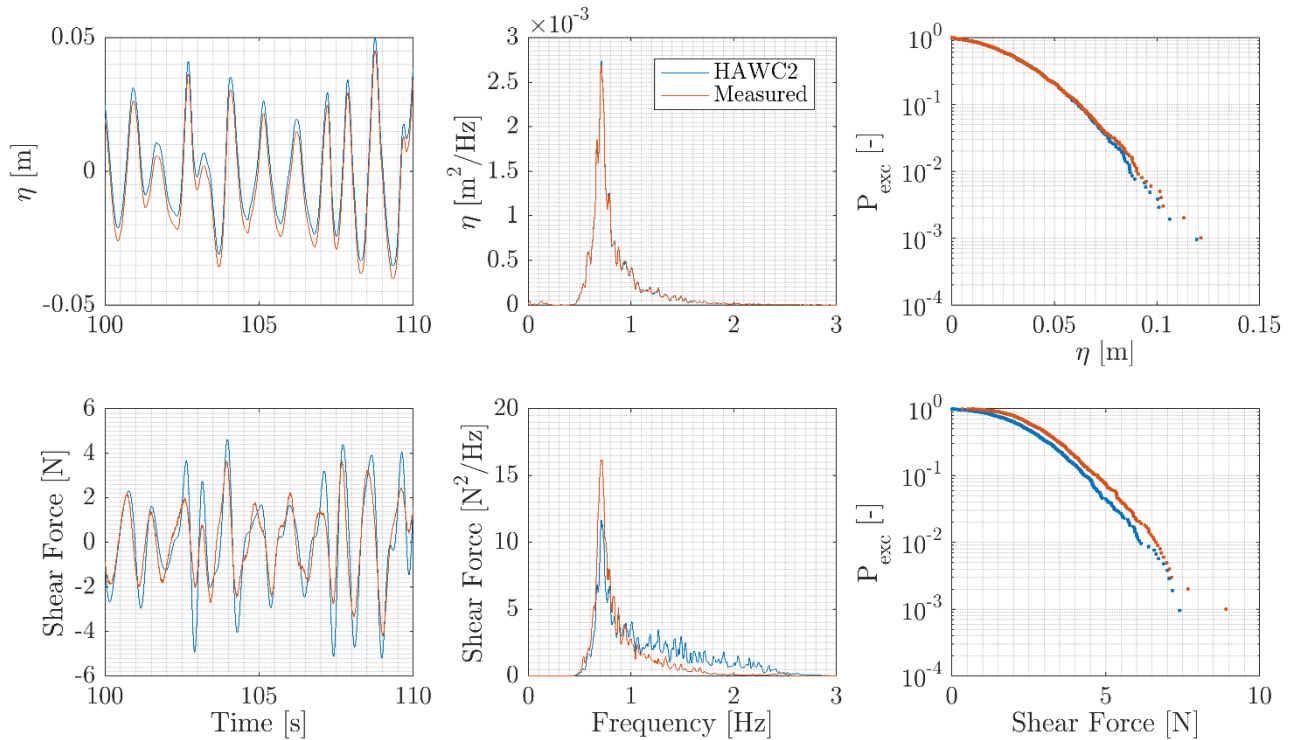


Figure 4: Wave elevation and shear force at the monopile base for the irregular waves I1 condition.

2.4.3 Irregular Waves I2

Figure 5 presents the shear force at the monopile base in line with wave propagation for the irregular waves I2 condition. In the frequency domain, the same trend as for the I1 condition can be seen for the shear force: the response at the wave peak frequency is under-predicted while the response towards higher frequencies is over-predicted.

The exceedance probability curves for bed shear force are in better agreement here. This is surprising since the sea state I2 is stronger than I1. One would thus expect larger deviations from the measurements in comparison to the smaller sea state response. In this case the HAWC2 and measured shear force curves cross over a few times. The largest peak is over-predicted by 8% by HAWC2.

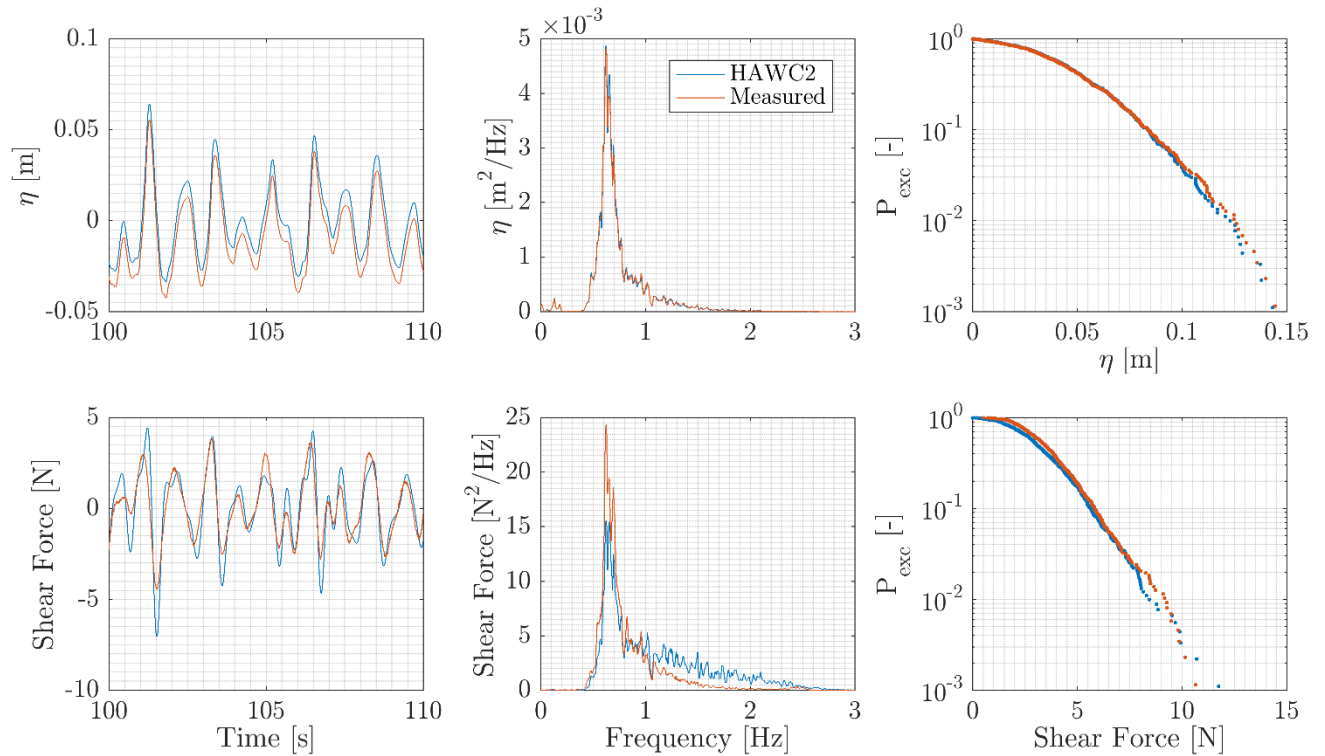


Figure 5: Wave elevation and shear force at the monopile base for the irregular waves I2 condition.

2.5 Conclusions

The present results show in a generic setting that the coupled HAWC2-WAMIT approach for flexible substructure modes is able to predict sectional loads in the substructure for irregular wave forcing. The model accuracy is limited due to the omission of nonlinear wave forcing effects and the omission of viscous drag loads. Despite these limitations, response outside of the primary wave spectrum was seen, thus illustrating that the flexible solver is able to predict dynamic response at the natural frequency of the structure.

Further and more accurate validation of the model would ideally be for a floating structure with a natural frequency within the forcing range. Such a validation is much more complex due to the presence of both rigid and flexible response modes. This is therefore left for future work.

3 Validation of second-order hydrodynamics in a state-of-the-art model of the OO-Star Wind Floater Semi 10MW

3.1 Introduction

In D4.6 [4] the OO-Star FAST model was adapted and compared to test results of pink noise waves, DLC 1.6 (severe sea state) and DLC 6.1 (extreme sea state). The model was extended to include second-order hydrodynamics through the Newman's approximation. Since the full QTF calculation requires considerable computational effort as it may cover a large number of frequency combinations, the Newman's approximation is typically used for estimating the second-order wave forces. The approach is based on the knowledge of the main diagonal of the QTF matrix only (the slow-drift force in regular waves).

In this study the model is extended to also include the full second-order solution, where a similar damping calibration approach as in D4.6 is utilized, in order to compare the two forcing models across the four load cases. Next a modal analysis approach is adapted in order to determine and calibrate a more realistic constant global damping matrix for both models.

The study is based on the planar motion (surge, heave and pitch) of the ocean basin load cases in D3.4 [5] where only waves are applied. For each sea state, the response in each of the planar DoFs (surge, heave and pitch) will be shown in terms of a representative portion of the time series (left column), a Power Spectral Density (PSD) plot (central column) and an exceedance probability plot (right column). To avoid initial transient effects the first 1800 s were discarded from both the PSD and the exceedance probability calculations. Furthermore, the PSD signals were smoothened by applying a moving-average filter with 20 points. Each response plot is followed by a table comparing test and model response in each planar DoF in terms of the mean $\bar{\xi}$, standard deviation σ and value at the 95% percentile $\xi^{95\%}$. The relative error in σ and $\xi^{95\%}$ is also shown. Lastly the second-order wave forces from the Newman approximation and the full second-order solution are presented in the same way as the responses, but with peak-to-peak (or Quantile-Quantile) plots instead of exceedance probability plots in order to emphasise the difference in the forcing models.

In the following “Newman” will refer to the model based on the Newman's approximation and “full QTF” will refer to the full second-order solution.

3.2 Full second-order solution

As also described in Section 7.3.5 the vector of wave excitation loads contains first- and second-order components and according to Pinkster [6], the second-order loads are due to five components:

1. the first-order relative wave elevation;
2. the quadratic interaction of the first-order velocity potential with itself;
3. the second-order velocity potential;
4. the interaction of the first-order potential and the first-order motion;
5. and the interaction of the first-order rotations with the first-order body accelerations.

As mentioned in Simos et al. [7], the first-order motion is sensitive to the amount of damping in the system. Since the viscous damping is expected to change with the sea state, the second-order analysis would have to be carried out for each sea state due to the dependence of the second-order solution on the first-order motion. This would require a few iterations of the 2nd-order solution for each sea state. Therefore, for the present work the contributions of the first-order motion to the second-order loads (items 4 and 5 in the list above) are not considered. This also allows a more general solution of the

second-order problem, which is independent on the motion and can thus be re-used for different environmental conditions, including cases with wind forcing. This simplification is expected to have small effect for mild sea states, but it may lead to an underprediction of the second-order loads for severe sea states. On the other hand, computation of the Quadratic Transfer Functions (QTFs) including the first-order solution with insufficient damping may lead to overestimation of the second-order loads [8]. Further details on the theory behind first- and second-order radiation diffraction theory can be found in Newman [9], Pinkster [6] and Lee [10].

Following the same approach as for the NAUTILUS (see section 7.3.5), the time-domain implementation of the second-order hydrodynamic loads has been verified against FAST v8 [11]. Full difference-frequency QTF matrices were computed in WAMIT for the six DoF, considering 50 angular frequencies in the range 0.0628-3.1416 rad/s, which corresponds to periods in the range 2-100 s. The sum-frequency loads were not included as they are expected to have negligible effects on the semisubmersible considered here (see [12], [8]). Taking advantage of symmetry, one half of the floater was discretized with 6585 panels (see Figure 64, right).

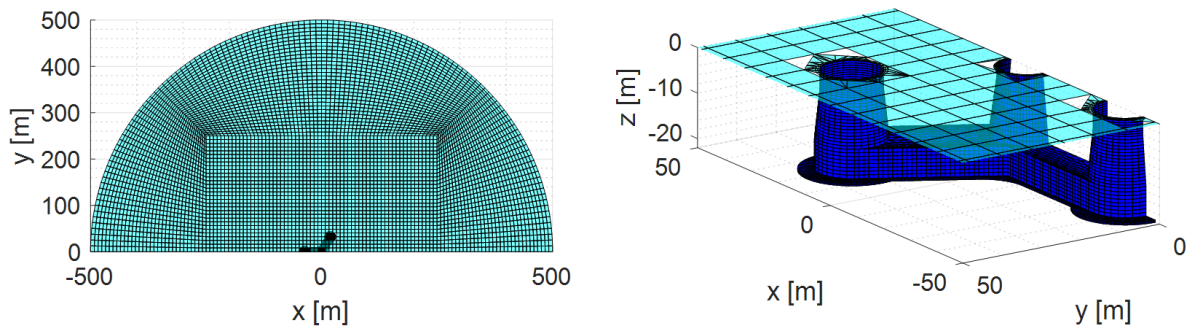


Figure 6: Panel discretization of the free surface (left) and the floater (right) for the OO Semi WAMIT analysis.

Similarly a reduced convergence study of the discretization of the free surface was conducted, where two parameters were varied: the radius of the partition inside which the integration of the quadratic forcing over the free surface is done numerically, RINNER; and the size of the free-surface panels relative to the body panel size at the free surface, SCALE. Results for RINNER values of 100, 300, 500 and 1000 m (keeping SCALE at 4) and SCALE values of 1, 2, 4 and 8 (keeping RINNER at 500 m) were compared for angular frequencies corresponding to 1.00, 1.05, 1.10 and 1.35 rad/s [13]. The convergence study suggested that, although the effect of the free surface was small, a discretization with RINNER=500 and SCALE=4 was appropriate. The agreement between the QTF results obtained with direct and indirect methods was also interpreted as a sign of numerical convergence with respect to panel resolution [14].

3.3 Global linear damping from diagonal elements

In D4.6 it was shown how a diagonal global linear damping matrix could be calibrated for each sea state such that the standard deviation in each degree of freedom is matched for a subset of the full time series.

The same method was then adapted to the model based on the full second-order solution (full Quadratic Transfer Function) in order to establish a comparison with the Newman approximation. D4.6 described how, by adding a global linear damping matrix, \mathbf{B}_1^* , and a quadratic damping matrix, \mathbf{B}_2^* , to the equations of motion of the floater, see Equation (3.1), the hydrodynamic damping could be calibrated based on the physical decay tests.

$$(\mathbf{M} + \mathbf{A}_\infty)\ddot{\xi} + \int_0^t \mathbf{K}(t - \tau) \dot{\xi}(\tau) d\tau + \mathbf{B}_1^* \dot{\xi} + \mathbf{B}_2^* |\dot{\xi}| \dot{\xi} + \mathbf{C}\xi = F_{exc} + F_{moor} + F_{visc} \quad (3.1)$$

where $\xi = [\xi_1, \xi_2, \dots, \xi_6]^T$ correspond to the system six degrees of freedom; surge, sway, heave, roll, pitch and yaw. \mathbf{M} illustrates the mass and inertia matrix of the combined system, \mathbf{A}_∞ is the resulting infinite-frequency limit of the added mass matrix, $\mathbf{K}(t) = \frac{2}{\pi} \int_0^\infty \mathbf{B}_{rad}(\omega) \cos(\omega t) d\omega$ in the convolution integral denotes the retardation kernel (based on radiation damping \mathbf{B}_{rad} only), and \mathbf{C} the hydrostatic stiffness matrix. Furthermore, the forces acting on the combined system are the wave excitation loads F_{exc} , the mooring reactions F_{moor} and the viscous effects F_{visc} .

The \mathbf{B}_1^* and \mathbf{B}_2^* denote a constant additional linear- and quadratic global damping matrices respectively in addition to the wave radiation damping and the drag computed by the Morison equation. In D4.6 it was shown how the elements along the main diagonals of \mathbf{B}_1^* and \mathbf{B}_2^* were added and initially calibrated by matching the model free decay tests. The values along the main diagonals were obtained iteratively through trial and error. In the HydroDyn-module of FAST the user can specify the elements of these global damping matrices

Then, it was shown that additional negative damping was needed for increasing sea state and these sea state dependencies have also been investigated in for example [15], [16], [17] and [18]. Thus, the global linear damping terms for the in-plane motions (surge, heave and pitch) in \mathbf{B}_1^* , were further calibrated for each load case by matching the standard deviation of the responses for the model and for the experiments. It was decided to adjust the additional linear damping terms through \mathbf{B}_1^* , as the Morison drag term introduces both forcing and damping. By increasing the drag coefficients not only the damping increases, but also the excitation. Due to the long duration of the tests, it was decided to do the calibrations based on shorter versions of the load cases, i.e. 1000 s (without transient). A better match is likely obtained for longer simulations.

The damping matrices \mathbf{B}_1^* and \mathbf{B}_2^* for the Newman based model were similarly applied to the full QTF model, in order to emphasize the effect of including the full QTF. In Figure 7 the results from calibration process in D4.6 is presented and it shows how the linear diagonal damping terms changes with significant wave height. The negative damping is compensating for the missing wave excitation forces, which increases with H_s . In the following comparison study the results from the pink noise waves and DLC 6.1 (2) will be presented.

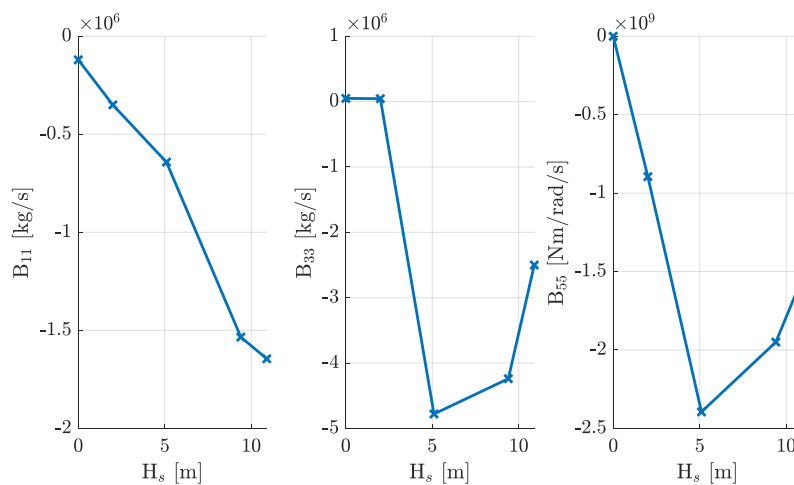


Figure 7: Global calibrated linear damping in-plane diagonals for different sea states

3.3.1 Pink Noise – $H_s = 2$ m, $T_p = [4.5, 18.2]$ s

Figure 8 shows the planar response to pink noise waves with $H_s = 2$ m and $T_p = [4.5, 18.2]$ s with corresponding result statistics presented in

Table 3.

It is seen from the figure that both models are matching the experiments very well in surge and heave with errors in the standard deviations being below 5% and the 95% percentiles being within 8% of the test results. Also, it can be seen from the heave PSD that a significant peak at the heave natural frequency is not captured by both models even though the response is matched well. This is because calibration by matching the standard deviation σ of the responses will ensure that the area under the global spectrum $S_{\xi,j}(\omega)$ will be the same, as $\sigma_{\xi,j}^2 = \int_0^\infty S_{\xi,j}(\omega) d\omega$. This means that the energy can be distributed slightly different in the PSD, but overall probability of exceedance will be matched.

For both models a significant error in the standard deviations of the pitch response of -11.6% can be seen, implying that the additional linear damping term for the pitch motion in \mathbf{B}_1^* needs some fine-adjustment.

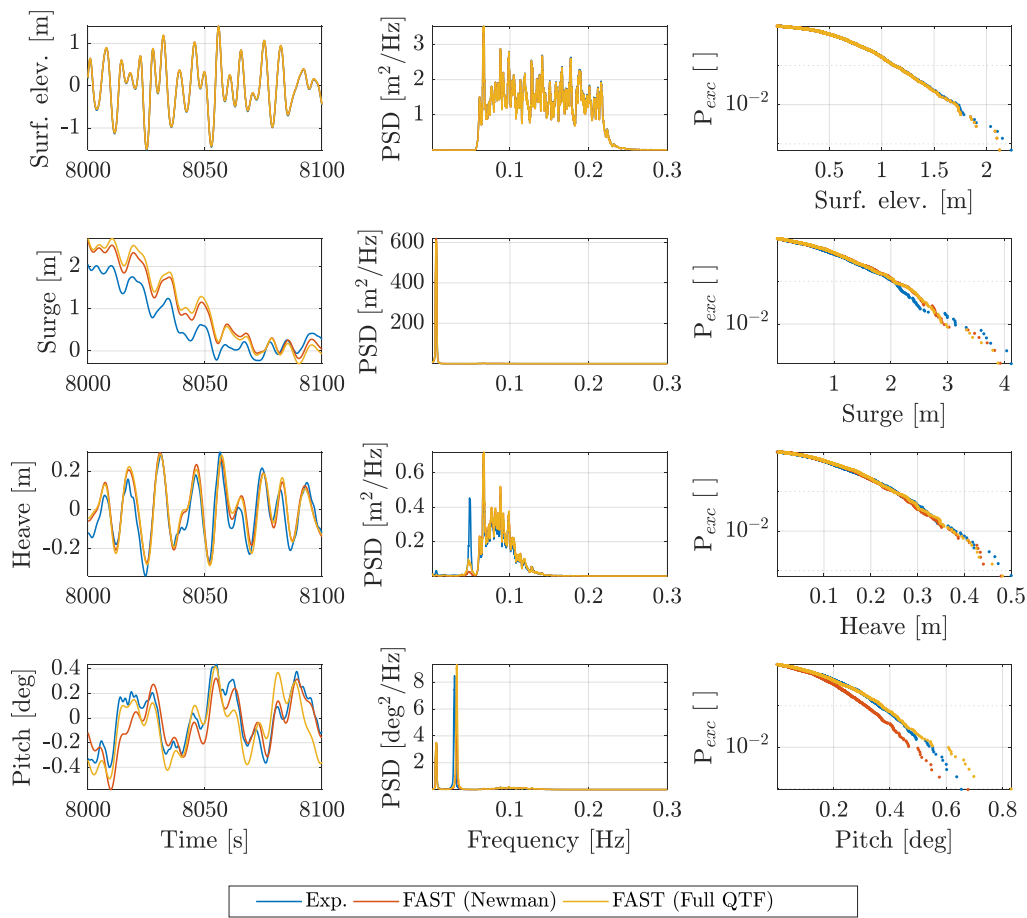


Figure 8: Time, frequency and exceedance probability plots for the pink noise waves

Table 3: Results statistics for pink noise waves

Newman	$\bar{\xi}_{test}$	$\bar{\xi}_{model}$	σ_{test}	σ_{model}	<i>Error</i> [%]	$\xi_{test}^{95\%}$	$\xi_{model}^{95\%}$	<i>Error</i> [%]
Surge [m]	0.77	0.72	1.13	1.19	4.94	2.27	2.44	7.20
Heave [m]	-0.02	0.00	0.13	0.12	-0.58	0.30	0.29	-3.11
Pitch [deg]	-0.02	-0.04	0.19	0.17	-11.64	0.42	0.37	-12.77
Full QTF	$\bar{\xi}_{test}$	$\bar{\xi}_{model}$	σ_{test}	σ_{model}	<i>Error</i> [%]	$\xi_{test}^{95\%}$	$\xi_{model}^{95\%}$	<i>Error</i> [%]
Surge [m]	0.77	0.73	1.13	1.18	4.04	2.27	2.45	7.70
Heave [m]	-0.02	0.00	0.13	0.13	0.95	0.30	0.30	-0.52
Pitch [deg]	-0.02	-0.04	0.19	0.20	3.48	0.42	0.43	1.62

3.3.2 DLC 6.1 (2) – $H_s = 9.4$ m, $T_p = 16$ s

The planar response to irregular waves is shown in Figure 9 for DLC 6.1 with $H_s = 9.4$ m, $T_p = 16$ s with corresponding result statistics presented in Table 4.

It is observed that, when the same damping matrices as for the Newman based model is applied to the full QTF model, the surge and pitch motions are over-predicted. The sudden change in response from the mild pink noise waves to the 50-year wave is likely due the increased resonant pitch response. This arrives from the structure having a low natural period in pitch, i.e. far from the diagonal in the QTF matrix and due to the surge/pitch coupling the surge response is similarly affected. The heave response for both models predicts very similar results with an error in the standard deviations of ~8% and within 5% in the 95% percentile, which is due to the heave motion being dominated by the waves.

The effect of including the full QTF matrix will be investigated in the following, by individually calibrating the global additional damping matrices in the modal space and by analysing the response and the second-order forces from both models.

Table 4: Results statistics for DLC 6.1 (2)

Newman	$\bar{\xi}_{test}$	$\bar{\xi}_{model}$	σ_{test}	σ_{model}	<i>Error</i> [%]	$\xi_{test}^{95\%}$	$\xi_{model}^{95\%}$	<i>Error</i> [%]
Surge [m]	2.57	4.77	3.28	3.21	-2.31	7.45	7.77	4.40
Heave [m]	-0.56	0.06	1.08	1.17	7.62	2.50	2.62	4.79
Pitch [deg]	0.68	-0.19	0.82	0.81	-1.17	1.97	2.00	1.91
Full QTF	$\bar{\xi}_{test}$	$\bar{\xi}_{model}$	σ_{test}	σ_{model}	<i>Error</i> [%]	$\xi_{test}^{95\%}$	$\xi_{model}^{95\%}$	<i>Error</i> [%]
Surge [m]	2.57	5.20	3.28	3.71	13.00	7.45	8.87	19.10
Heave [m]	-0.56	0.05	1.08	1.17	8.34	2.50	2.58	3.13
Pitch [deg]	0.68	-0.24	0.82	1.15	39.90	1.97	2.84	44.66

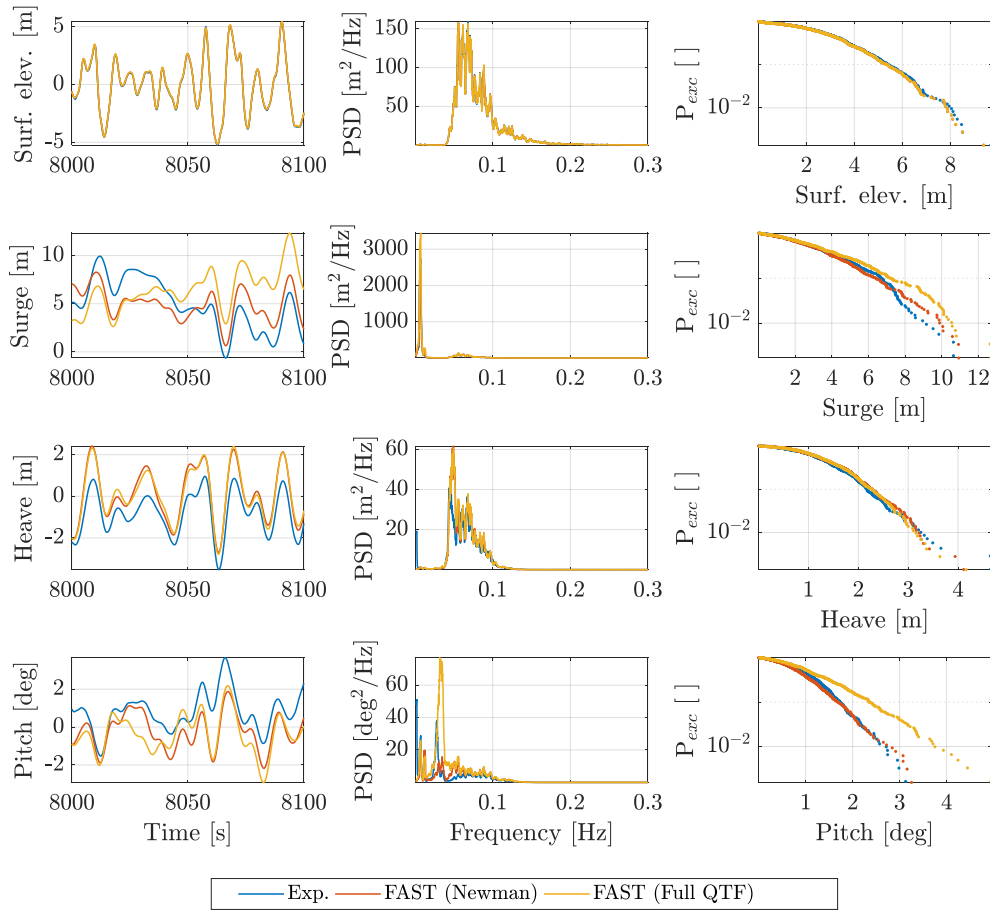


Figure 9: Time, frequency and exceedance probability plots for DLC 6.1 (2)

3.4 Global linear damping from modal analysis

The method of calibrating the diagonals in the linear global damping matrix is a decent approach, since it is fast and efficient, but it neglects the coupling between the various degrees of freedom. In order to include the coupling effects for especially the surge/pitch, a similar approach as seen in Section 7.3.4 is used, where a constant linear global damping matrix \mathbf{B} is built in the modal space. The modal damping coefficients b_n for each mode are calibrated and then by utilizing the modal vectors of the numerical model, these can be transformed back to the physical space creating the \mathbf{B} matrix. The numerical model's system matrix \mathbf{D}_{num} is built as

$$\mathbf{D}_{num} = (\mathbf{M} + \mathbf{A}_0)^{-1}(\mathbf{C}_{hst} + \mathbf{C}_{moor}) \quad (3.2)$$

where \mathbf{M} is the mass matrix, \mathbf{A}_0 is the zero-frequency limit of the added mass matrix, \mathbf{C}_{hst} is the hydrostatic restoring matrix and \mathbf{C}_{moor} is the mooring restoring matrix, resulting from the linearization of the mooring system around the equilibrium position in still water. The diagonalization of \mathbf{D}_{num} provides a set of eigenvectors contained in the columns of Ψ_{num} , which is used to diagonalize the model's mass m_n and stiffness matrices c_n :

$$[m_n] = \Psi_{num}^T (\mathbf{M} + \mathbf{A}_0) \Psi_{num} \quad (3.3)$$

$$[c_n] = \Psi_{num}^T (\mathbf{C}_{hst} + \mathbf{C}_{moor}) \Psi_{num} \quad (3.4)$$

For each mode, the modal damping coefficient is thus computed as $b_n = 2\zeta_n\sqrt{m_n k_n}$. Finally, the diagonal matrix of modal damping coefficients $[b_n]$ is transformed back to the physical space by virtue of

$$\mathbf{B} = (\Psi_{num}^T)^{-1} [b_n] \Psi_{num}^{-1}. \quad (3.5)$$

The six modal damping ratios ζ_n are calibrated until the standard deviation σ of the computed response in the in-plane DoF (surge, heave and pitch) is as close as possible to the standard deviation of the measured response. In both signals the first 1800 s are discarded in the computation of standard deviation. By working with modal damping coefficients, the damping in each DoF is independently calibrated with only one parameter.

The calibration process is done for both the Newman based model and the full QTF model to study and the result from the calibrations are two constant linear global damping matrices \mathbf{B} for each sea state. An example of one of these damping matrices determined from the modal analysis can be seen in Table 5.

Figure 10 shows the in-plane modal damping ratios as function of significant wave height. As expected the Newman based model has similarly trends, as for the global calibrated linear damping diagonals, recall Figure 7. However it can be seen that the full QTF solution compensate for the missing wave excitation forces in the model, thus much less negative damping is needed for heave and pitch. The reason for the similar results for surge, is likely due to the high natural period in surge, hence close to the diagonal in the QTF matrix, and thus close to the Newman approximations.

Table 5: Example of an additional linear damping matrix determined from the modal analysis for the OO-Star Wind Floater. Case: pink noise waves – full QTF model

Linear	1 (Surge)	2 (Sway)	3 (Heave)	4 (Roll)	5 (Pitch)	6 (Yaw)
1 (Surge)	-1.79E+05	0	0	0	-1.72E+06	0
2 (Sway)	0	-1.79E+05	0	1.72E+06	0	0
3 (Heave)	0	0	7.10E+05	0	0	0
4 (Roll)	0	1.72E+06	0	-8.37E+08	0	0
5 (Pitch)	-1.72E+06	0	0	0	-8.37E+08	0
6 (Yaw)	0	0	0	0	0	4.02E+09

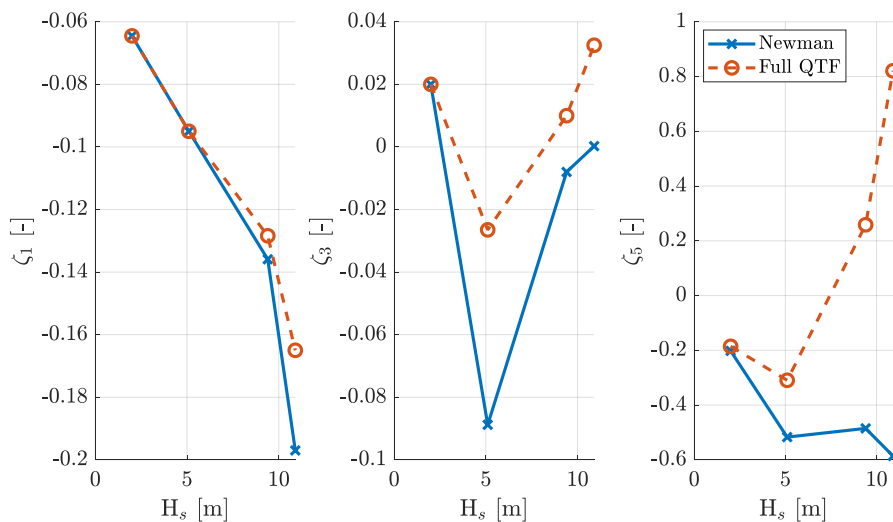


Figure 10: Calibrated in-plane modal damping ratios as function of sea state

3.4.1 Pink Noise – $H_s = 2$ m, $T_p = [4.5, 18.2]$ s

The in-plane response to the pink noise wave with $H_s = 2$ m and $T_p = [4.5, 18.2]$ s is shown in Figure 11 and corresponding result statistics are presented in Table 6.

Similar to the previous approach, it can be seen that the surge and pitch are dominated by resonance at the natural frequency, while the linear wave loads dominate the heave response for the two models. Again it is observed that the peak at the heave natural frequency in the tests is not captured by the numerical models, though more resonant response is captured by the full QTF solution. This is most likely due to the axial Morison drag coefficient for the central heave plate being slightly over-predicted.

However the responses for both models are matched very well with errors in the standard deviations all being within 3% and errors in the 95% percentiles up to 3.2% for heave and pitch. But a slight overprediction of 6-7% is observed for both surge responses in the 95% percentile.

Figure 12 present the in-plane 2nd-order wave forces for the pink noise load case. It is evident that the full QTF solution introduces much more forcing compared to the Newmans approxiamtion. It is observed that the force in surge is matched well up to ~ 0.5 Hz for the full QTF solution. This agrees well with the fact that the calibrated damping ratio for surge is almost identical to the Newman based model due to the resonant nature of the surge response, i.e natural frequency close to the diagonal in the QTF matrix. The heave on the other hand is dominated by the linear waves, hence a good match in the response is obtained for both models eventhough the full QTF solution introduces significantly higher second-order forces. The mild sea state for the pink noise waves is most likely the reason to that the pitch responses for both models are matched.

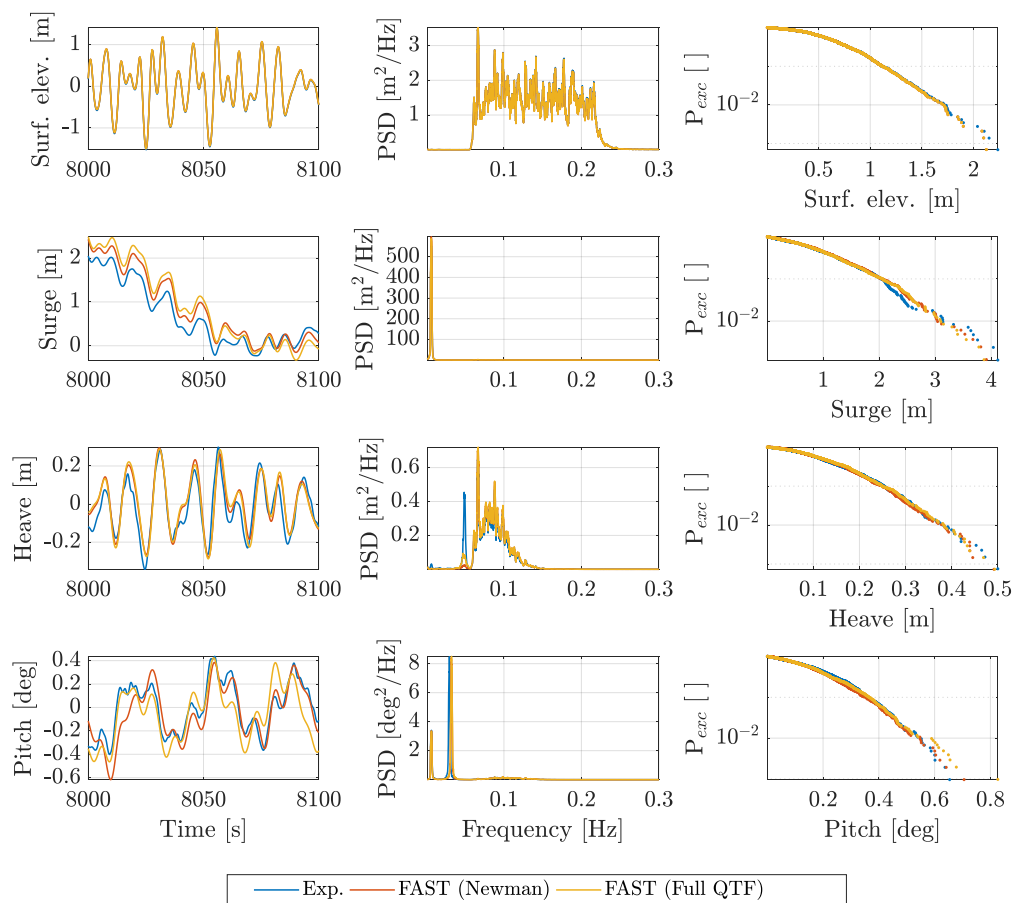
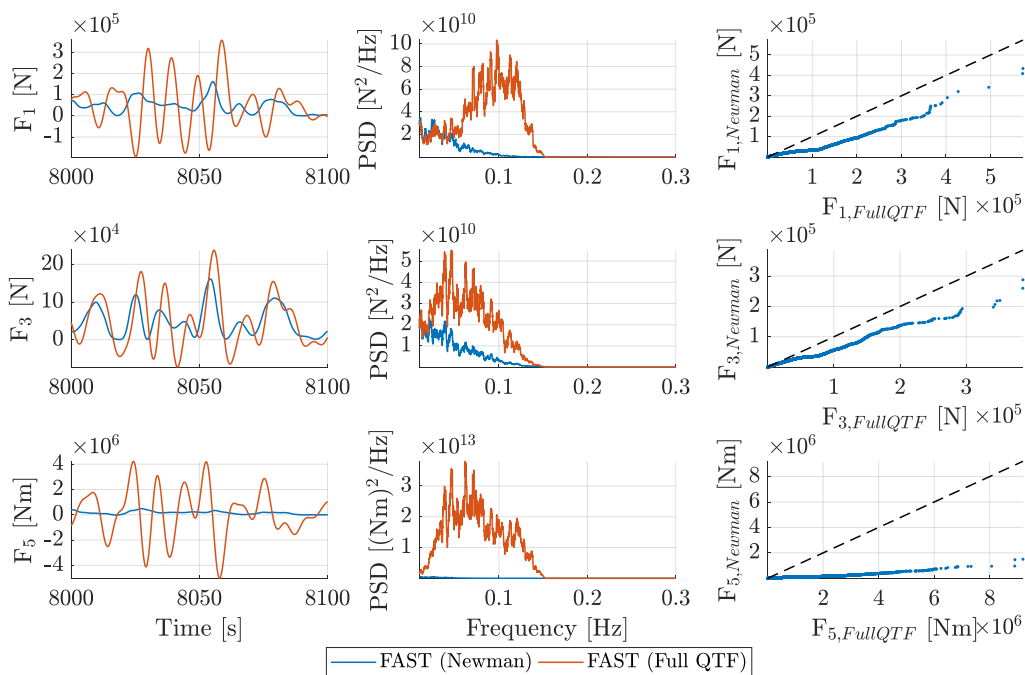


Figure 11: Time, frequency and exceedance probability plots for the response in pink noise waves – modal calibrated

Table 6: Results statistics for pink noise waves – modal calibrated

Newman	$\bar{\xi}_{test}$	$\bar{\xi}_{model}$	σ_{test}	σ_{model}	Error [%]	$\xi_{test}^{95\%}$	$\xi_{model}^{95\%}$	Error [%]
Surge [m]	0.77	0.69	1.13	1.16	2.90	2.27	2.41	5.94
Heave [m]	-0.02	0.00	0.13	0.12	-0.87	0.30	0.30	-3.10
Pitch [deg]	-0.02	-0.04	0.19	0.19	-2.03	0.42	0.41	-2.77
Full QTF	$\bar{\xi}_{test}$	$\bar{\xi}_{model}$	σ_{test}	σ_{model}	Error [%]	$\xi_{test}^{95\%}$	$\xi_{model}^{95\%}$	Error [%]
Surge [m]	0.77	0.70	1.13	1.15	2.13	2.27	2.43	6.94
Heave [m]	-0.02	0.00	0.13	0.13	0.92	0.30	0.30	-0.48
Pitch [deg]	-0.02	-0.04	0.19	0.19	0.67	0.42	0.42	0.10


Figure 12: Time, frequency and peak-to-peak plots for the 2nd-order wave forces in pink noise waves – modal calibrated

3.4.2 DLC 1.6 – $H_s = 10.9$ m, $T_p = 15$ s

The in-plane response to DLC 1.6 (severe sea state) is shown in Figure 13 and corresponding result statistics are presented in Table 7.

A good match in all response standard deviations for both models are obtained with the errors being below 4% but both models also tend to deviate for the maximum values. This is evident from the error in the 95% percentiles, where for the Newman based model an overprediction of ~5% is obtained compared to 4% for the full QTF solution. However the Newman based model underpredicts the 95% percentile for the pitch by ~9.5% and the full QTF solution model overpredicts by ~15.6%. This could likely be solved by a few more iterations in the calibration procedure.

It should be noted that in the time series, for the particular window shown, a difference in phase is observed for the wave frequency range. It was checked that this is not a general tendency for the full time series.

Figure 14 present the in-plane 2nd-order wave forces for the pink noise load case. It is again evident that the full QTF solution introduces more forcing, which is missing in the Newman based model and thus result in the need of negative diagonal damping terms.

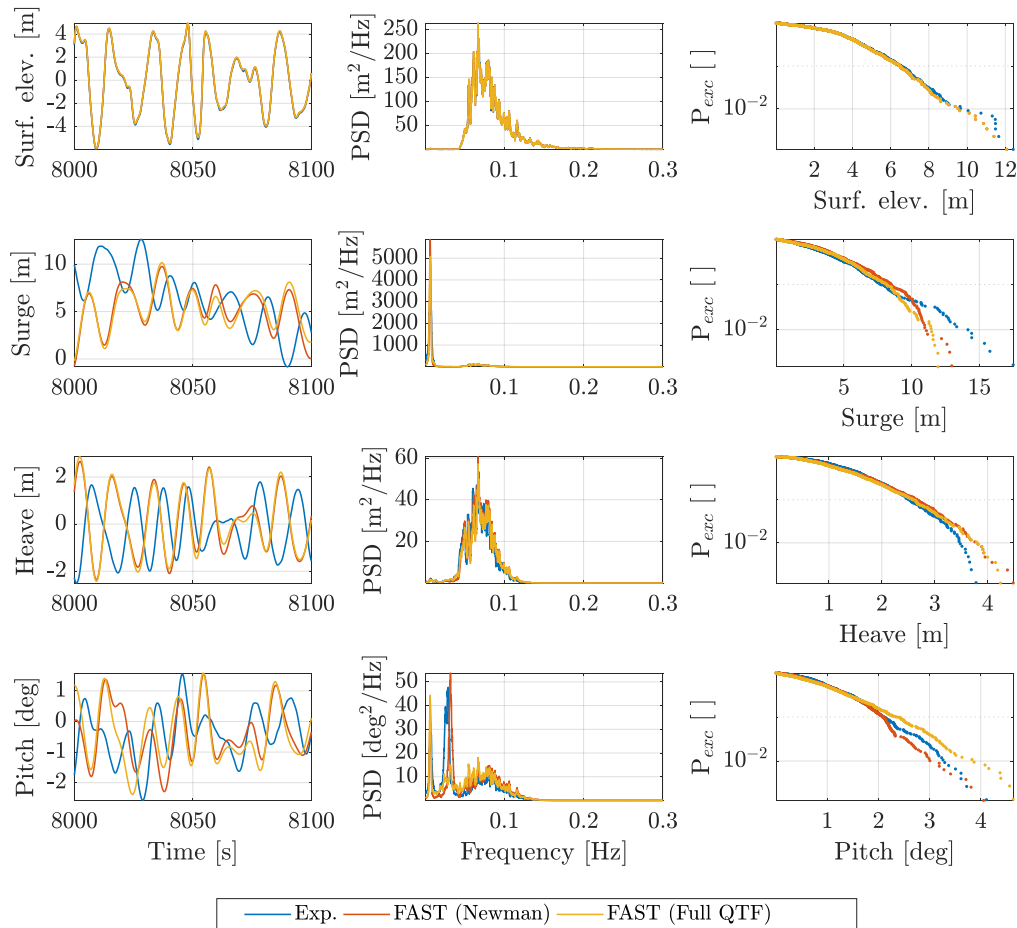


Figure 13: Time, frequency and exceedance probability plots for the response in DLC 1.6 – modal calibrated

Table 7: Results statistics for DLC 1.6 – modal calibrated

Newman	$\bar{\xi}_{test}$	$\bar{\xi}_{model}$	σ_{test}	σ_{model}	Error [%]	$\xi_{test}^{95\%}$	$\xi_{model}^{95\%}$	Error [%]
Surge [m]	5.28	3.36	4.15	4.19	0.84	9.44	9.87	4.56
Heave [m]	-0.20	0.15	1.18	1.22	3.15	2.89	3.03	4.89
Pitch [deg]	-0.19	-0.24	0.98	1.00	2.03	2.50	2.26	-9.45
Full QTF	$\bar{\xi}_{test}$	$\bar{\xi}_{model}$	σ_{test}	σ_{model}	Error [%]	$\xi_{test}^{95\%}$	$\xi_{model}^{95\%}$	Error [%]
Surge [m]	5.28	3.76	4.15	4.13	-0.55	9.44	9.12	-3.43
Heave [m]	-0.20	0.14	1.18	1.20	1.01	2.89	3.01	4.15
Pitch [deg]	-0.19	-0.28	0.98	0.96	-1.32	2.50	2.89	15.62

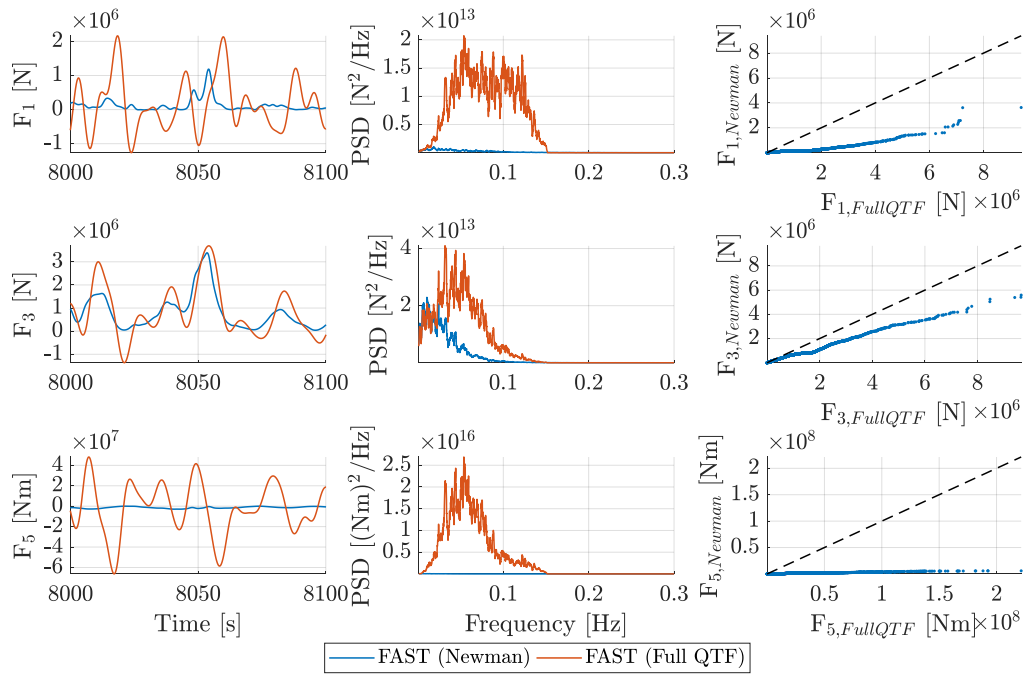


Figure 14: Time, frequency and peak-to-peak plots for the 2nd-order wave forces in DLC 1.6 – modal calibrated

3.4.3 DLC 6.1 (1) – $H_s = 5.1$ m, $T_p = 9$ s

The in-plane response to DLC 6.1 (1) (extreme sea state) is shown in Figure 15 and corresponding result statistics are presented in Table 8. Figure 16 present the in-plane 2nd-order wave forces for the pink noise load case.

Both models predict a good match in standard deviation and 95% percentile for the surge response with an maximum error of 4% and 1% for the Newman- and full QTF based model respectively. However deviations between the two models arise in heave and pitch response. It is seen that the Newman based model overpredicts the standard deviation of the heave response by ~5% whereas the full QTF solution matches well with the experiments. Similiarly when looking at the standard deviation of the pitch response the Newman approximation underpredicts by 10% and the full QTF solution by 4%. This deviation in the heave and pitch might be related to the wave peak period being approximately half the natural period of the heave (~21 s). This results in an increased resonant response in the vertical plane, emphasised from the heave PSD plot, which is not an advisable application of the Newman's approximation [14].

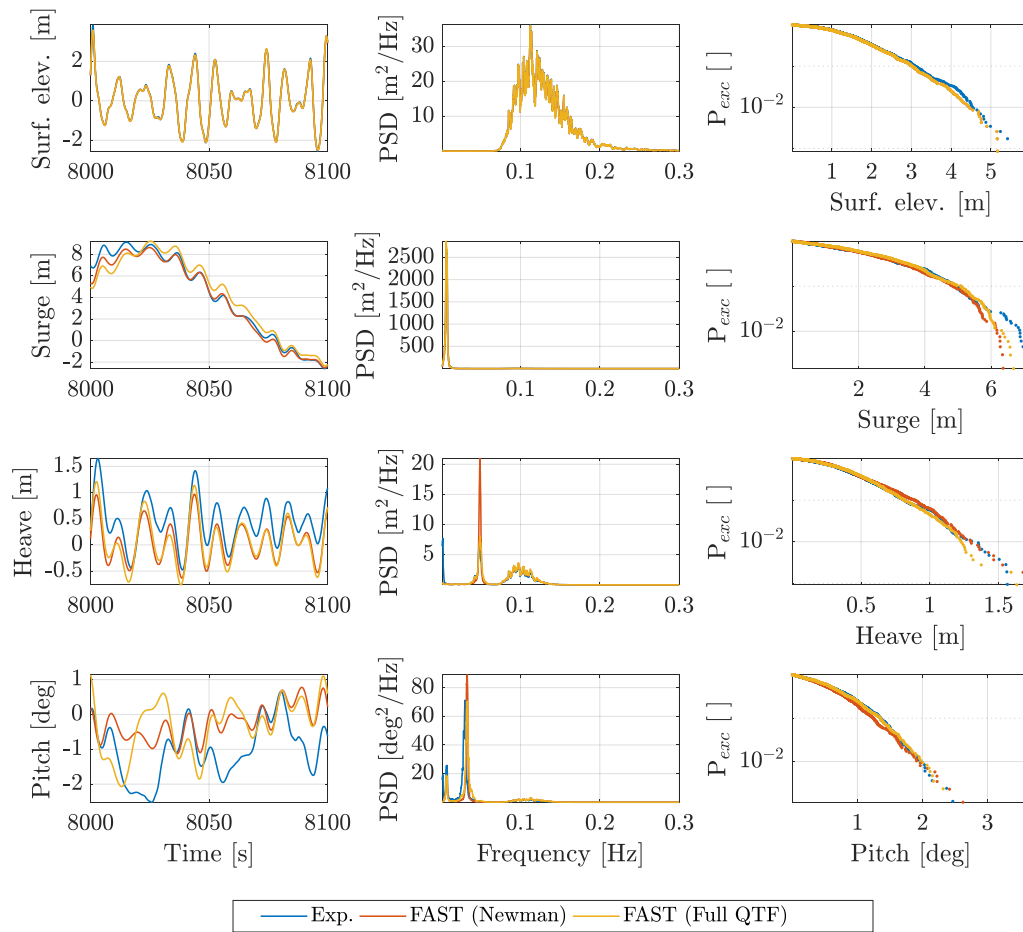


Figure 15: Time, frequency and exceedance probability plots for the response in DLC 6.1 (1) – modal calibrated

Table 8: Results statistics for DLC 6.1 (1) – modal calibrated

Newman	$\bar{\xi}_{test}$	$\bar{\xi}_{model}$	σ_{test}	σ_{model}	Error [%]	$\xi_{test}^{95\%}$	$\xi_{model}^{95\%}$	Error [%]
Surge [m]	3.66	3.38	2.89	-3.64	-3.64	5.46	5.45	-0.08
Heave [m]	0.29	0.05	0.38	0.40	5.35	1.04	1.04	-0.14
Pitch [deg]	-0.70	-0.19	0.72	0.65	-10.23	1.55	1.49	-3.56
Full QTF	$\bar{\xi}_{test}$	$\bar{\xi}_{model}$	σ_{test}	σ_{model}	Error [%]	$\xi_{test}^{95\%}$	$\xi_{model}^{95\%}$	Error [%]
Surge [m]	3.66	3.42	2.89	2.93	1.43	5.46	5.62	2.94
Heave [m]	0.29	0.05	0.38	0.38	-0.38	1.04	0.98	-6.19
Pitch [deg]	-0.70	-0.20	0.72	0.70	-3.64	1.55	1.54	-0.47

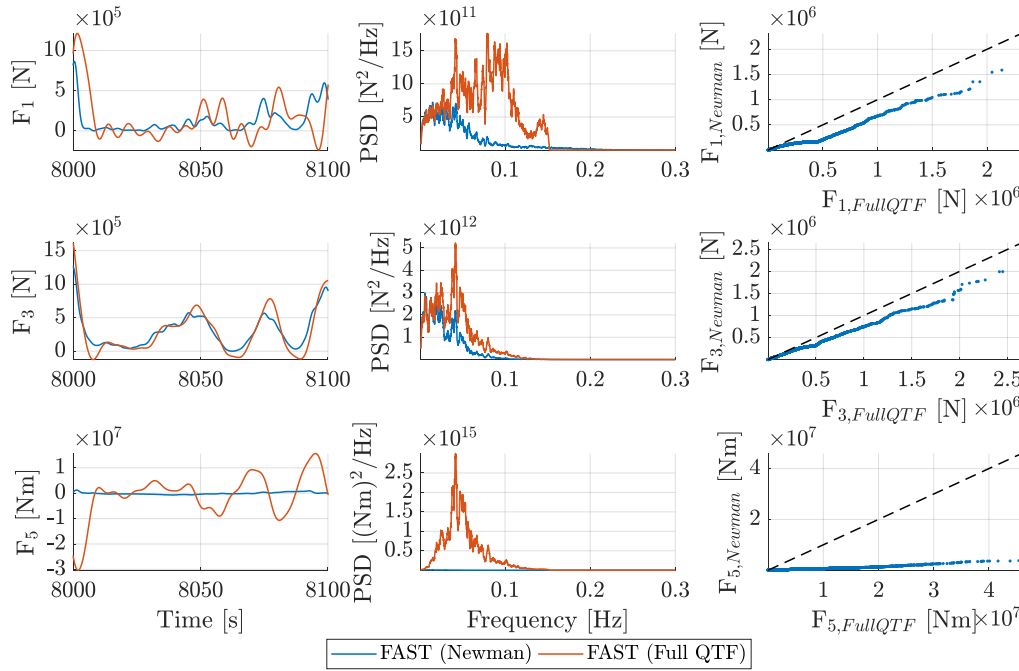


Figure 16: Time, frequency and peak-to-peak plots for the 2nd-order wave forces in DLC 6.1 (1) – modal calibrated

3.4.4 DLC 6.1 (2) – $H_s = 9.4$ m, $T_p = 16$ s

The in-plane response to DLC 6.1 (2) (extreme sea state) is shown in Figure 17 and corresponding result statistics are presented in Table 9. Figure 18 present the in-plane 2nd-order wave forces for the pink noise load case. Similarly to the previous cases it is observed that the full QTF solution introduces much higher second-order forces compared to the Newman approximation – an effect mostly seen in the heave and pitch as these requires significantly less negative damping and in some cases even positive damping.

A good match in all response standard deviations for both models are obtained with the errors being below 6%, with only a significant deviation for the maximum values of the pitch response for the full QTF model. This is evident from the error in the 95% percentiles of the pitch response, where an overprediction of ~16% is seen.

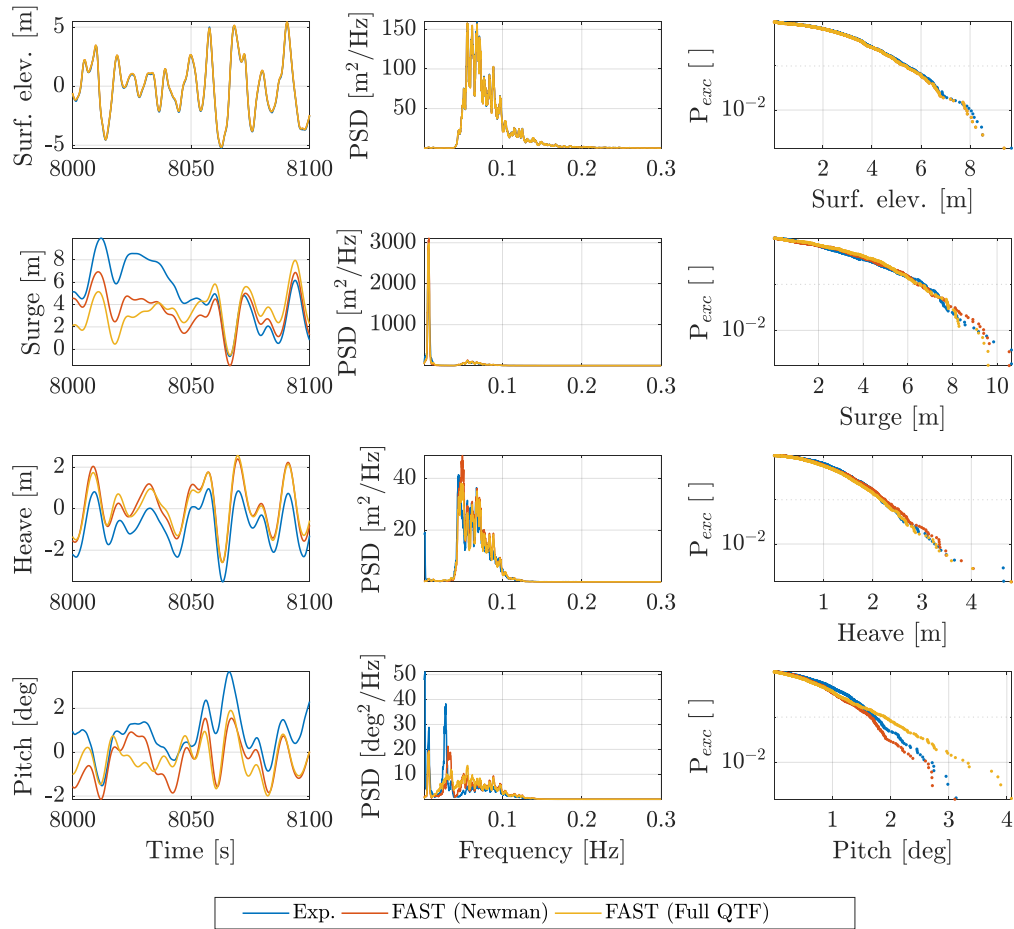


Figure 17: Time, frequency and exceedance probability plots for the response in DLC 6.1 (2) – modal calibrated

Table 9: Results statistics for DLC 6.1 (2) – modal calibrated

Newman	$\bar{\xi}_{test}$	$\bar{\xi}_{model}$	σ_{test}	σ_{model}	Error [%]	$\xi_{test}^{95\%}$	$\xi_{model}^{95\%}$	Error [%]
Surge [m]	2.57	2.23	3.28	3.30	0.49	7.45	7.55	1.33
Heave [m]	-0.56	0.08	1.08	1.12	3.01	2.50	2.58	3.36
Pitch [deg]	0.68	-0.15	0.82	0.78	-5.89	1.97	1.83	-6.91
Full QTF	$\bar{\xi}_{test}$	$\bar{\xi}_{model}$	σ_{test}	σ_{model}	Error [%]	$\xi_{test}^{95\%}$	$\xi_{model}^{95\%}$	Error [%]
Surge [m]	2.57	2.44	3.28	3.32	1.03	7.45	7.53	1.07
Heave [m]	-0.56	0.08	1.08	1.08	-0.25	2.50	2.52	0.93
Pitch [deg]	0.68	-0.18	0.82	0.81	-2.25	1.97	2.29	16.29

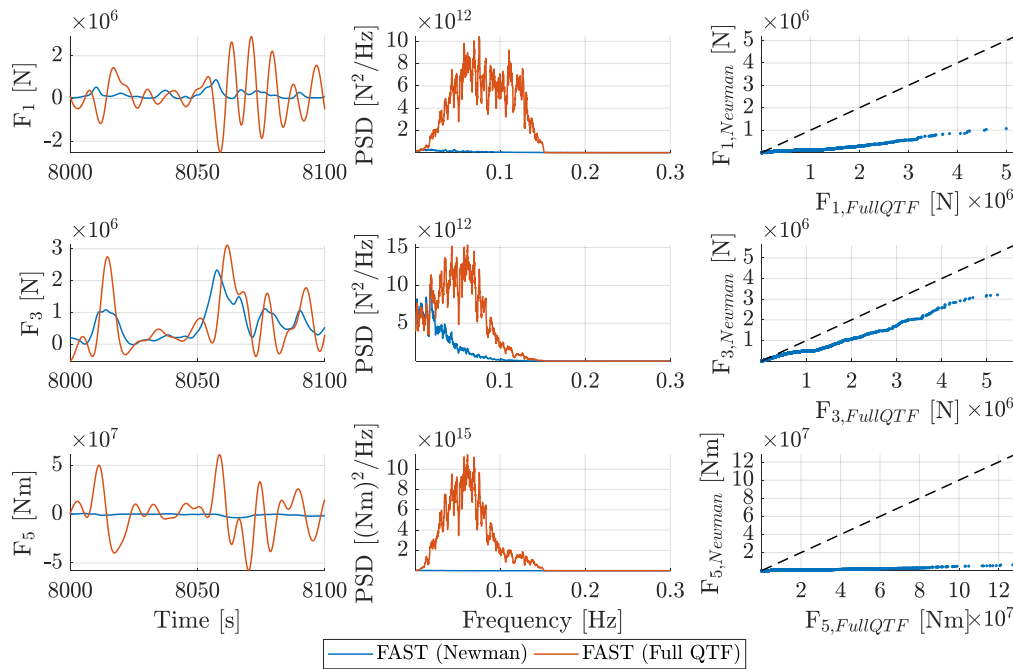


Figure 18: Time, frequency and peak-to-peak plots for the 2nd-order wave forces in DLC 6.1 (2) – modal calibrated

3.5 Discussion and conclusion

In this study the FAST model was extended to include second-order hydrodynamics through the full Quadratic Transfer Function solution. It was shown how a diagonal global linear damping matrix could be calibrated for each sea state such that the standard deviation in each degree of freedom is matched for a subset of the full time series. A comparison study of the results from the full second order solution and the Newman's approximation was then performed in terms of the in-plane response.

It is apparent from the comparison study of the full second order solution and the Newman's approximation that by using the same calibrated global diagonal damping matrices in both models, the responses are similar for mild sea states. However, it was also shown that for a more severe sea state the enhanced second-order forces introduced by the full QTF solution, will counteract the negative damping needed for the Newman based model.

Then extending the calibration method to also include the off-diagonal terms in the global linear damping matrix, by the use of a modal analysis, it was shown how the 2nd-order wave forces calculated by the full second order solution are much higher than the Newman's. This has a huge impact on the resonant responses located far from the diagonal in the QTF matrix. However, the surge is matched very well by both models with only a slight difference in the calibrated damping ratios and this is most likely related to the structure having a high natural period of surge, i.e. close to the diagonal in the QTF matrix.

A deviation in the heave response was observed for DLC 6.1 (1), which might arise from an increased resonant motion in the heave response, which may be too far from the diagonal in the QTF matrix to yield a proper Newman approximation by the diagonal terms.

The modal analysis damping calibration method allows a faster convergence of the response standard deviations, as the modal damping ratios are adjusted compared to the other approach where the physical space diagonal damping terms are adjusted. However, both calibration methods are capable of capturing the responses in the tests, if enough time is put into the calibration process.

4 Validation of OpenFOAM CFD for the OO-Star Wind Floater Semi 10MW

Previously in deliverable “D4.7: Models for advanced load effects and loads at component level” [36], we presented preliminary results of the CFD simulations of the LIFES50+ OO-Star Wind Floater Semi 10 MW, hereafter OO-Star, using the open source CFD solver, OpenFOAM. The study included added mass and damping analyses as well as floater response in arbitrary given regular waves and comparisons against FAST and WAMIT. The present chapter details further validations of the solver against SINTEF experiments and FAST results including new mooring analysis, decay tests and floater responses. The results are accompanied with new insights for instance, a further look into the effects of boundary conditions, specifically the wall boundary, as well as turbulence modelling.

4.1 Methodology of solving flow and body motion equations

For the sake of completeness, we here recap some of the main points regarding the governing equations and numerical solver.

Governing flow equations: The governing equations for conservation of mass and momentum to be solved using OpenFOAM in a Eulerian frame of reference, are given by

$$\nabla \cdot \mathbf{u} = 0, \quad (4.1)$$

$$\frac{\partial}{\partial t}(\rho \mathbf{u}) + \nabla \cdot (\rho \mathbf{U} \mathbf{u}) = -\nabla p + \nabla \cdot \boldsymbol{\tau} + \rho \mathbf{f}_b \quad \text{with } \mathbf{U} = \mathbf{u} - \mathbf{u}_g \quad (4.2)$$

where ∇ is the 3D gradient operator, \mathbf{U} is the relative motion velocity, \mathbf{u} and \mathbf{u}_g are the fluid and mesh velocity, respectively, p is the pressure, ρ is the local density of the fluid. $\boldsymbol{\tau} = 2\mu \mathbf{S}$ is the stress tensor, with μ and \mathbf{S} being the dynamic viscosity and the strain rate tensor and \mathbf{f}_b is the sum of the external body forces acting on the fluid.

For the two phase air-water flows with interface, in order to determine the position of the free surface, the volume of fluid method (VOF) is applied by solving a transport equation for the phase volume fraction field, α ($\alpha \in [0,1]$), and calculating fluid properties at each point as a mixture between air ($\alpha=0$) and water ($\alpha=1$).

$$\frac{\partial \alpha}{\partial t} + \nabla \cdot \mathbf{U} \alpha + \nabla \cdot \mathbf{u}_r \alpha (1 - \alpha) = 0 \quad (4.3)$$

In the above equation, $\mathbf{u}_r = \min[\mathbf{U}, \max(\mathbf{U})]$ is an artificial compressive velocity and the last term in the left hand side is an extra artificial interface compression that is applied to the region near free surface (through the term $\alpha(1 - \alpha)$) in order to avoid smearing of the wave interface. Ocean waves are generated and damped using the relaxation technique developed by [11] and extended by [12] as illustrated in Figure 19 and explained in D4.7.

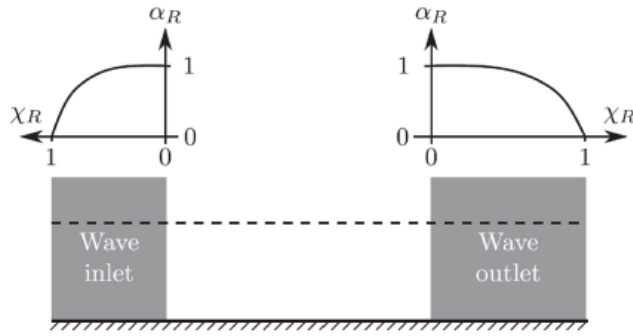


Figure 19: The relaxation zone at both inlet and outlet.

External loads: Once the pressure and stresses on the surface of the floater are calculated from the flow solver, the total force and moment including mooring forces on the floater will be given as

$$\mathbf{F} = F_p + F_v + \mathbf{F}_M, \quad (4.4)$$

$$\mathbf{M} = \iint_S (\mathbf{r}_{CS} \times (p\hat{\mathbf{n}} + \boldsymbol{\tau})) dS + \mathbf{r}_{CM} \times \mathbf{F}_M \quad (4.5)$$

where \mathbf{F}_M is the mooring force, \mathbf{r}_{CM} is the vector from the center of mass to the mooring attachment point and \mathbf{r}_{CS} is the center of each surface panel.

Motion solver: A 6-degree-of-freedom (6 DOF) solver then uses external forces and moments to update the location of the floater. The movement of the body is followed by the mesh deformation which uses the Laplace equation of the form $\nabla \cdot (\gamma \nabla u) = 0$ to deform the mesh. Here, γ is a diffusivity factor and u is the velocity of a particular grid that modifies the grid according to $x_{new} = x_{old} + u\Delta t$.

4.1.1 Mooring analysis

In the previous deliverable (D4.7) a static moored case was simulated using a simple model in which a linear spring system was deployed to moor the floater and the spring stiffness was obtained from the restoring matrix derived from FAST simulations. This approach has, however, limited geometric similarity to the physical mooring system of the model tests. Here, following the recent work by Bruinsma, Paulsen, & Jacobsen, (2018), we have used an extended approach and catenary equations are solved to obtain quasi-static mooring responses. In this approach, the mooring loads are assumed to be in quasi-static equilibrium in each time step. While nonlinear restoring effects are captured, hydrodynamic, inertial and other dynamics loads on the mooring lines are not included in the quasi-static approach.

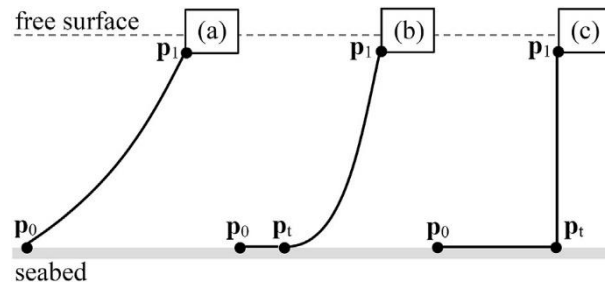


Figure 20: Schematic representation of the three different states of the catenary mooring line, where (a) is the simple state, (b) the resting state and (c) the hanging state (Bruinsma et al., 2018).

The mooring lines are implemented in the waves2foam library by Bruinsma, Paulsen, & Jacobsen, (2018). A flat horizontal seabed is assumed and three different mooring line states are defined. A simple state, resting state and hanging state as elaborated by Krenk, (2001) are depicted in Figure 20.

In the simple state the mooring line is in full suspension and the formulation follows the restoring force in a catenary line between two attachment points, where the distance between the attachment points is less than the length of the line. The line cannot break, while the distance between the connected objects can exceed the defined length of the line. Beyond this defined length the line is treated as a linear spring (Bruinsma, Paulsen, & Jacobsen, 2018).

In the resting state, the location of floating structure relative to the anchor point is such that a part of the catenary line is resting on the sea bed. The remainder of the cable acts as a catenary line, as defined in the simple state.

Finally, in the hanging state the floater is so close to the anchor point that the distance between the attachment point at the floater and the seabed contact point is shorter than the length of the mooring line. Only a vertical force acts in the attachment point, which is equal to the weight of the suspended part of the line.

4.2 Numerical set up

Simulations are performed using OpenFOAM's multiphase solver interDyMFOam, coupled with the wave generation toolbox waves2Foam. OpenFOAM uses a segregated cell-centred finite volume approach on unstructured polyhedral meshes. The combined solver uses the PIMPLE algorithm for pressure-velocity coupling. A non-conformal grid is generated and refined by importing the geometry and using the unstructured meshing library, snappyHexMesh (sHM) in such a way that the mesh is refined satisfactorily only in the vicinity of the floater and free surface to reduce computational cost.

The solver dynamicFvMesh is used to move the mesh surrounding the rigid body once it moves. Dynamic meshing is based on deformation of mesh without topological changes in the mesh configuration. The 2nd order Newmark implicit solver is used for the time integration of the mesh motion. For mesh deformation, the spherical linear interpolation (SLERP) algorithm is used in which mesh deformations (rotation and translation) are expressed using septentrions and quaternions [13]. For each grid point, deformation is scaled from the full to no deformation based on the distance from the moving body surface. It is defined using a minimum and a maximum distance with lower bound (no deformation) being of the order of the boundary layer thickness, and the upper bound be limited by the minimum distance to any domain boundary.

Lateral boundaries are slip-free walls and the top wall has an atmospheric boundary condition.



Regarding the turbulence modeling, a literature survey reveals that there is no common consent on the necessity of turbulence modeling nor is there an agreement on the choice of a turbulence model [14]. A preliminary test on the choice of turbulence modeling for the cases with fixed platform revealed no noticeable discrepancies between applying a turbulence model or running simulations in laminar mode and this was mainly due to the flow staying predominantly laminar in current investigations. Therefore, to reduce the number of variables involved in the simulations and to save computational time, all cases presented here are computed using a laminar flow assumption. This assumption has also been practiced by [13], [15], [16], [17] among others.

Variable time stepping is generally employed in all simulations by the Courant–Friedrichs–Lewy (CFL) number to ensure numerical stability and the 2nd-order Crank-Nicolson scheme is used for the time integration. In specific cases, however, due to arising instabilities, a combined time marching is used throughout the simulations by choosing fixed time steps for parts of the run time. This method is found to improve the overall simulation time. Sensitivity studies with respect to the grid resolution and time stepping are conducted in D4.7 [36].

The unbounded, conservative Gauss linear corrected scheme (second-order) is used for the Laplacian terms, while the gradient terms are discretized with linear Gaussian integration. The phase fraction equation is solved using a multi-dimensional universal limiter for explicit solution (MULES) algorithm, which ensures that values of scalar fields are bounded, in particular α remain between 0 and 1, see [18], [19]. To relax the MULES limitation to Courant number, thereby reduce running time, the Semi-implicit version of MULES is applied to the current simulations, which first executes an implicit predictor step before constructing an explicit correction on which the MULES limiter is applied.

Figure 21 shows a sketch of the numerical set up, numerical mesh and boundary conditions.

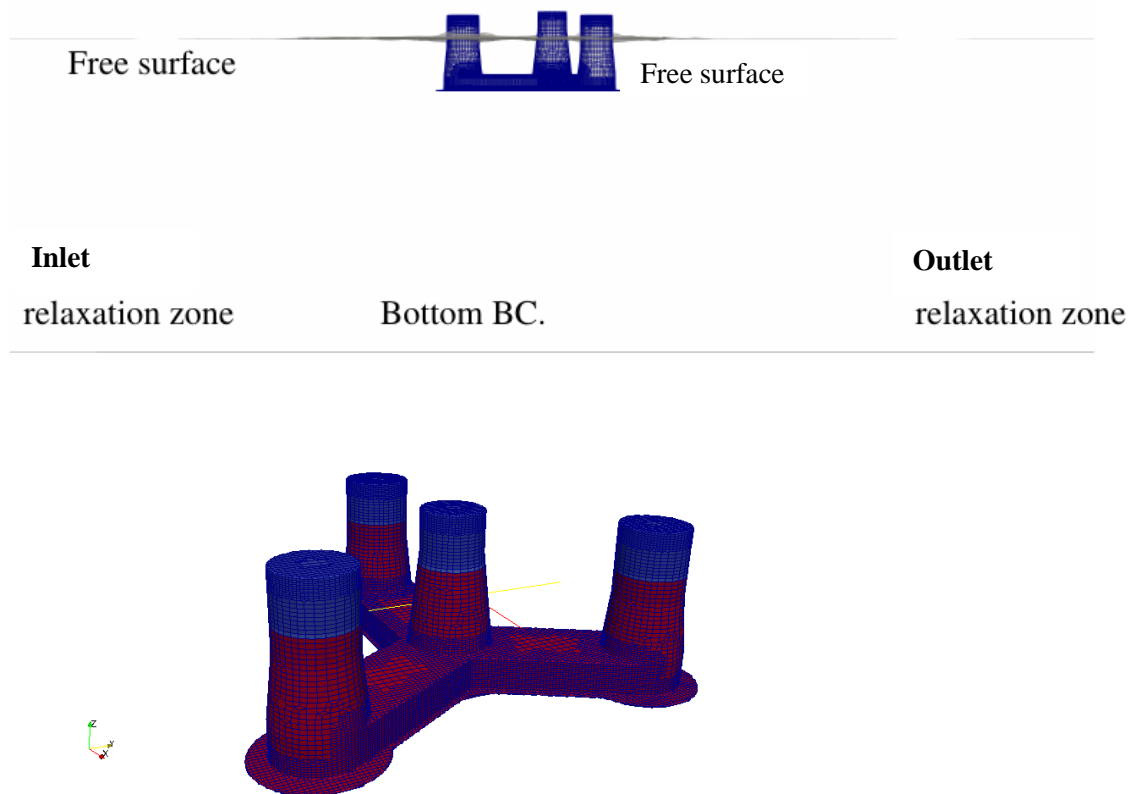


Figure 21: Schematic of the computational domain and boundary conditions (top) and a close-up of the mesh edge refinement near the floater walls (bottom). The interface between the two colours indicates free surface.

For the free heave decay simulation, CFD results are compared with FAST [20]. In the FAST model the frequency-domain radiation-diffraction results obtained from WAMIT are transformed to the time domain by the use of convolution integrals. Viscous effects, not captured by the potential-flow solver, are computed internally in FAST through the Morison drag term. Further details on the FAST model used here are given in [21], [22] as well as D4.7 [36].

4.2.1 Modified mooring system

The adapted mooring system in our CFD simulations uses catenary equations to solve for the tension forces along the mooring elements. The mooring system of the prototype and as used in the model scale experiments consists of three catenary mooring lines. Each mooring line is made from a single chain with a clump weight attached at approximately $1/7^{\text{th}}$ of its length. Unlike the experiments, the solver at its present form does not allow addition of the clump weight. Moreover, it only takes into account one reference mass per length and therefore, does not include the dry chain mass, while the fairlead point is at 9.5m (full scale) above the sea level when the floater is at rest. In order to proceed with the moored CFD simulations, an approximate “effective” mooring set up was devised based on FAST- MoorDyn simulations. The aim was to keep the stiffness in all degrees of freedom of same value as in the experimental setup. However, it was not possible to match all DoF forces. It was therefore decided to match the surge and pitch DoFs while the heave has a slight offset. In brief, the following was made to achieve a simplified mooring:

- The clump weight was removed, and the number of elements reduced from 9 nodes and 6 lines (i.e. 2-line segments and 3 nodes per mooring line) to 6 nodes and 3 lines
- The fairlead points were moved to $z=0$ (SWL). The line length remained the same as original
- The mass per length of the lines was accordingly increased to match the force-displacement curves in surge and in pitch

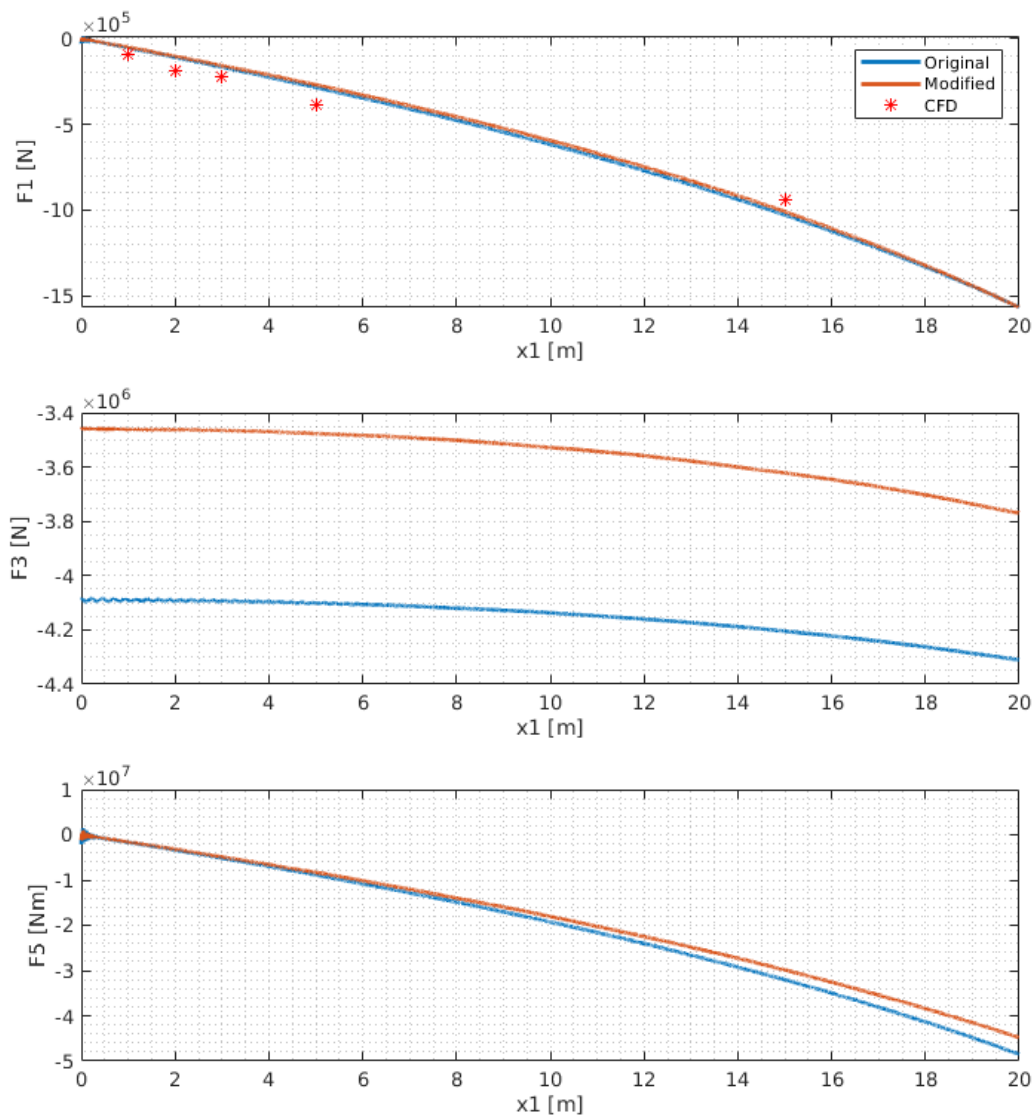


Figure 22 shows the global mooring reactions, F_x , F_z and M_y , obtained using FAST simulations when the floater is moved up to 20m from the equilibrium. By removing the clump weights, the pre-tension reduces slightly. This should, however, only affect the line tension itself, since the effect of the clump weights on the platform draft is expected to be small as the mass of the clumps is less than 1% of the total floater mass. The original and modified mooring line characteristics in full scale are shown in Table 10.

Table 10 – Specifications of original and modified mooring lines used for the CFD simulations

Case	Mass (dry) kg/m	Mass (wet) kg/m
Original – excl. clump	375.38	327.85
Modified – no clump	-	552.47

In order to assess the mooring stiffness in the CFD setup, pull out tests were carried out and initial loadings in surge and heave direction were measured and the results are plotted at Figure 22(top) for

the surge force. As can be seen, CFD simulations are able to reproduce the same loading in the surge direction.

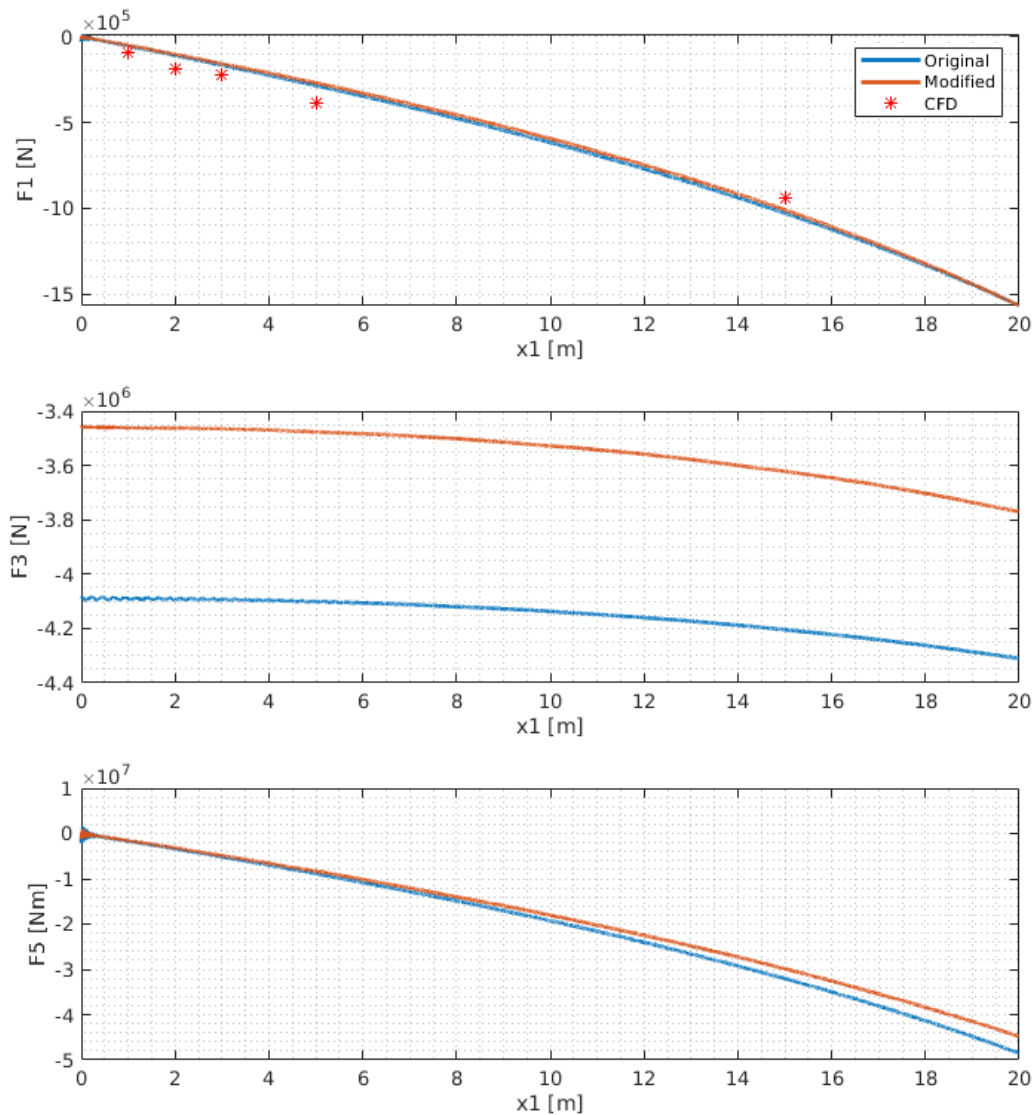


Figure 22: Modification of the mooring system for CFD computations for surge (top), heave (middle) and pitch (bottom) degrees of freedom. Blue (Original) and red (Modified) curves represent the forces on the original and modified mooring system, respectively.

Figure 23 shows the force-displacement values obtained from the CFD simulations using different initial positions for the floater and the linear fit represents the stiffness. As seen in Figure 23 (right), the stiffness in the heave force increases with initial distance. However, such a trend is not as visible in the surge case.

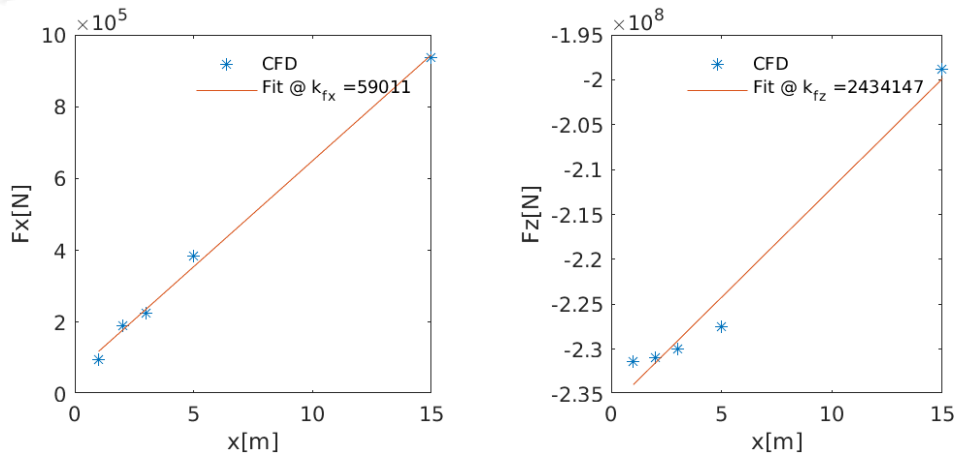


Figure 23: Assessment of the CFD mooring stiffness using pull-out tests. Horizontal axis is the initial location in surge direction and the vertical axes are magnitudes of surge (F_x) and heave (F_z) force.

Figure 24 shows a snapshot of the moored floater in the CFD domain.

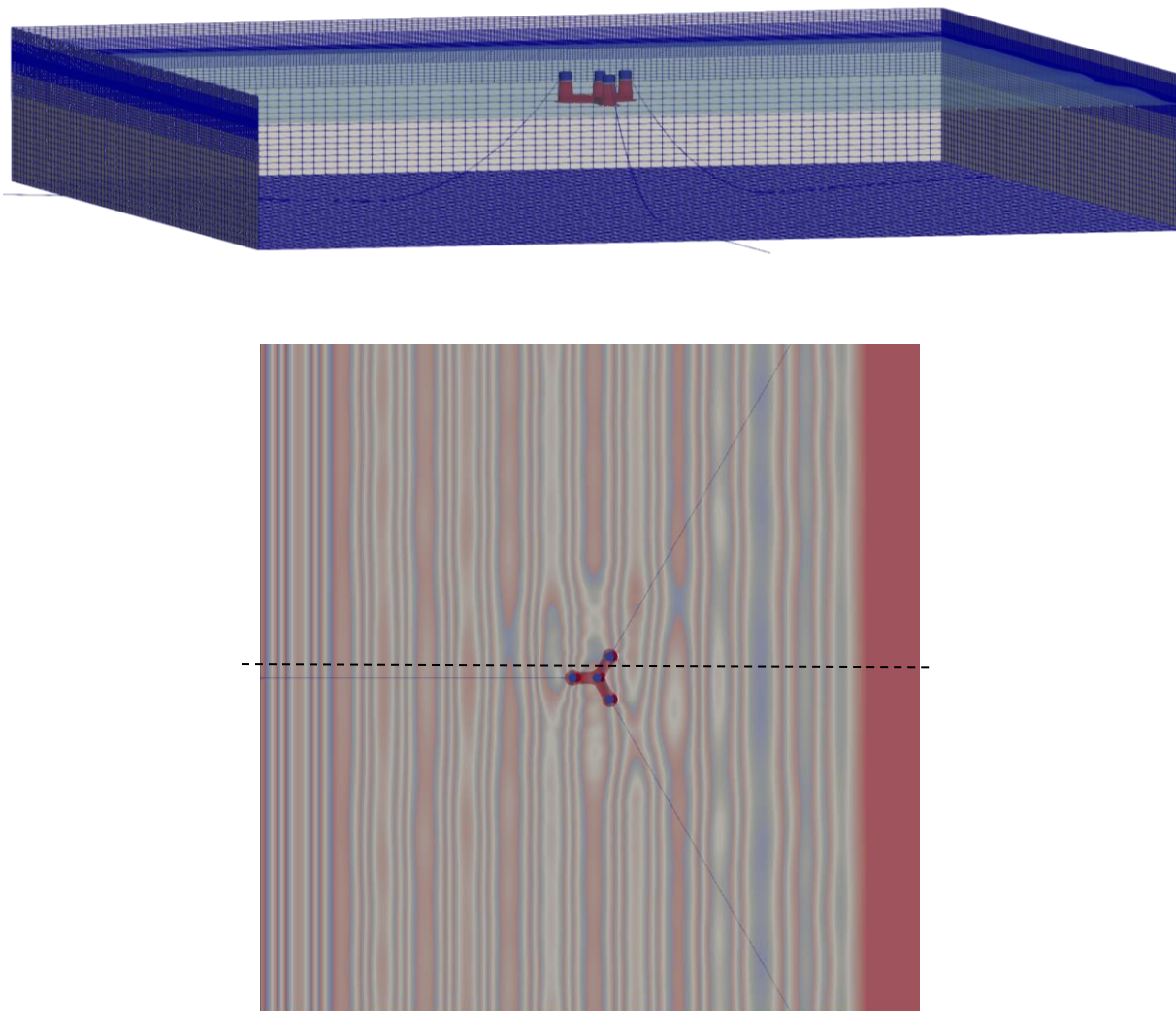


Figure 24: Implementation of the modified mooring system in CFD domain. Black dashed line represents the cross-sectional view shown in

Figure 31.

4.3 Selection of test cases

Two cases of comparison against the model tests are presented. First, the results of free heave decay simulations with and without mooring lines are discussed and next results for regular wave response is shown. Further, the sensitivity of the results to turbulence treatment and boundary conditions are also investigated for selected test cases. The mesh and time resolution are chosen following the refinement study performed in D4.7. The simulations were performed in real scale and in order to save computational time, a numerical tank of 1000 by 1000 by 130 m is used instead of full extent of the SINTEF Ocean's basin ($L \times B \times D = 2880\text{m} \times 2160\text{m} \times 130\text{m}$ in full scale). It is believed, however, that this domain size is large enough for the results to stay domain independent, although bound long waves may be affected.

4.3.1 Free decay simulations

Figure 25 shows the response of the floater in free heave decay without the mooring in frequency and time domains. Here a direct comparison with the experiments is not performed since free heave decay tests without mooring were not performed in the experiments. Instead, a direct comparison against FAST is performed, which shows an excellent match between the two models. The peak shown in Figure 25 (left) indicates the natural frequency of the floater.

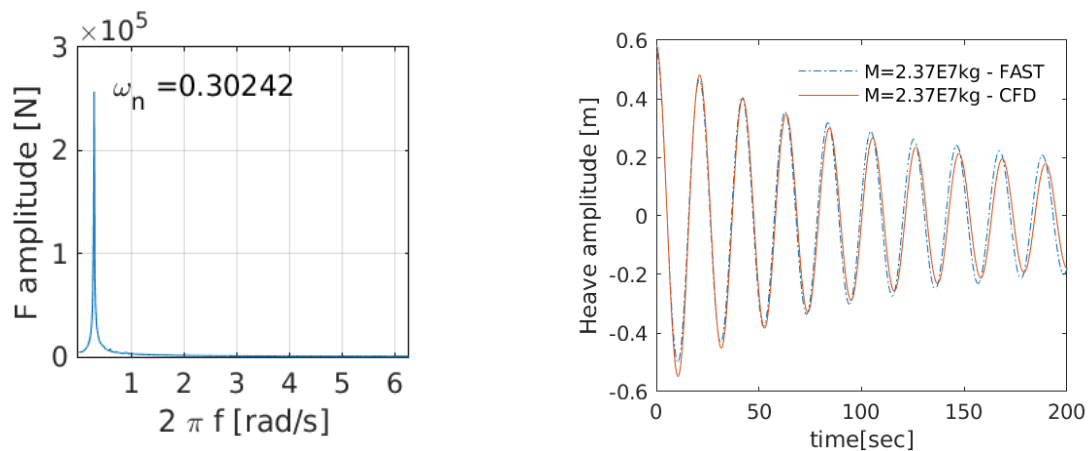


Figure 25: Free heave decay force response simulations – test no. 3020.

Next, we will consider the moored free heave decay test, corresponding to test number 3131. Figure 26 shows comparison of CFD and measurements in free heave decay amplitudes. As can be seen, CFD simulations are predicting heave oscillations very closely although a slight frequency mismatch is noticeable.

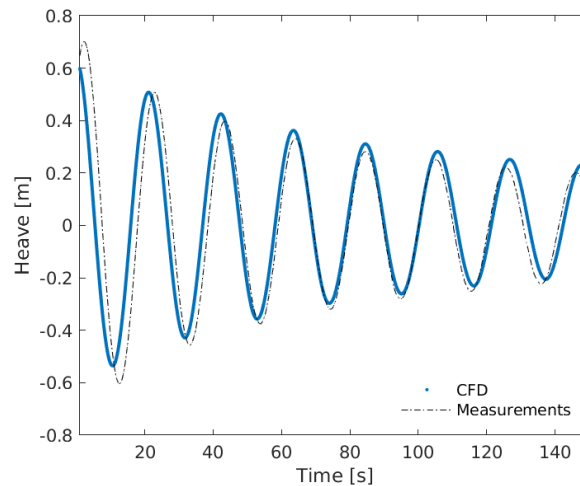


Figure 26: Comparison of CFD and measurements in free heave decay amplitudes – test no. 3131.

To investigate any possible impact of the turbulence modeling on the accuracy of simulations, simulations using laminar and turbulent flow modeling are both presented. Figure 27 shows the force response of the floater in free heave decay simulations. As can be seen, here the effect of turbulence on the global heave force is negligible although the addition of turbulence dissipation, tends to reduce the force spikes. The spikes stem from the solver's instabilities and limiting them may lead to better code stability. For more details on the source of spikes, see deliverable D4.7 [36].

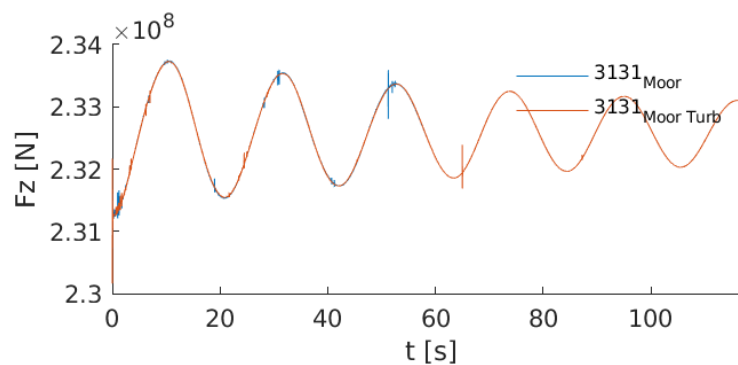


Figure 27: Effect of turbulence modelling on the performance of the CFD solver. F is the heave external force (see Eq. 4.4)

4.3.2 Wave induced floating simulations in regular waves (test 4010: H2.1m, T9s)

This section present CFD results of the test case 4010 with catenary mooring lines implemented and the loadings are shown in Figure 28. CFD predicted motions for this case have been compared against wave basin measurements and results of the surge and heave motion are plotted in **Error! Reference source not found.**

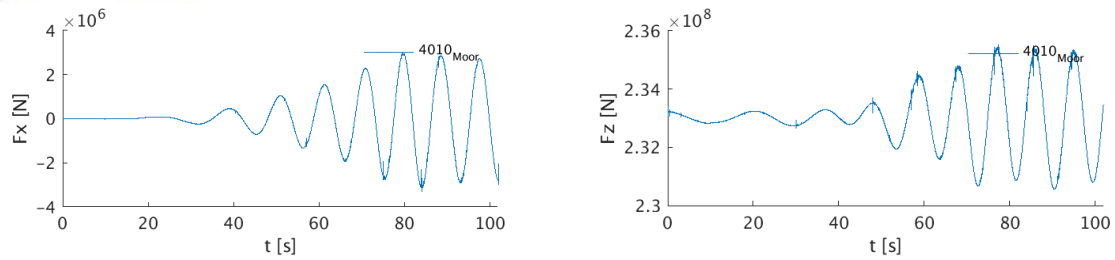


Figure 28: CFD computation of loads on the floater for test case 4010 (H2.1m, T9s) in time domain. Left: surge forces, right: heave forces.

Since the wave basin is larger than the CFD domain, it takes longer for the generated waves to reach the floater in the measurements. Therefore, to match CFD and experiments, measurement signals were shifted in time to adjust to the CFD setup. To assess the accuracy of CFD predictions, two sets of plots are presented. In the first category, as shown in Figure 29, the CFD wave elevation is shifted in time to best match the measurement and the corresponding surge and heave response are examined. In the second category, the CFD predicted surge response is time shifted to best match the experiments and the corresponding wave elevation and heave response are examined. This result is shown in Figure 30. As can be seen from both figures, there is generally a good match between the CFD and measurements for wave elevation and surge as well as the transient behaviour. The heave frequency is also well-predicted although some mismatch exists in the amplitudes. A low-frequency heave response seems to overlay the wave-frequency heave response in the CFD results.

Generally, the match between the numerical and experimental results is good. The numerical solution is seen to reproduce the low-frequency transient response in surge, related to the floater's initial movement from rest to the equilibrium position related to the mean drift wave loads. Additionally, the motion response at the wave frequency is reproduced in both heave and surge, although with the mentioned overlaid low-frequency variation in heave. This latter behaviour may be a result of the difference in wave generation between the lab and the CFD setup.

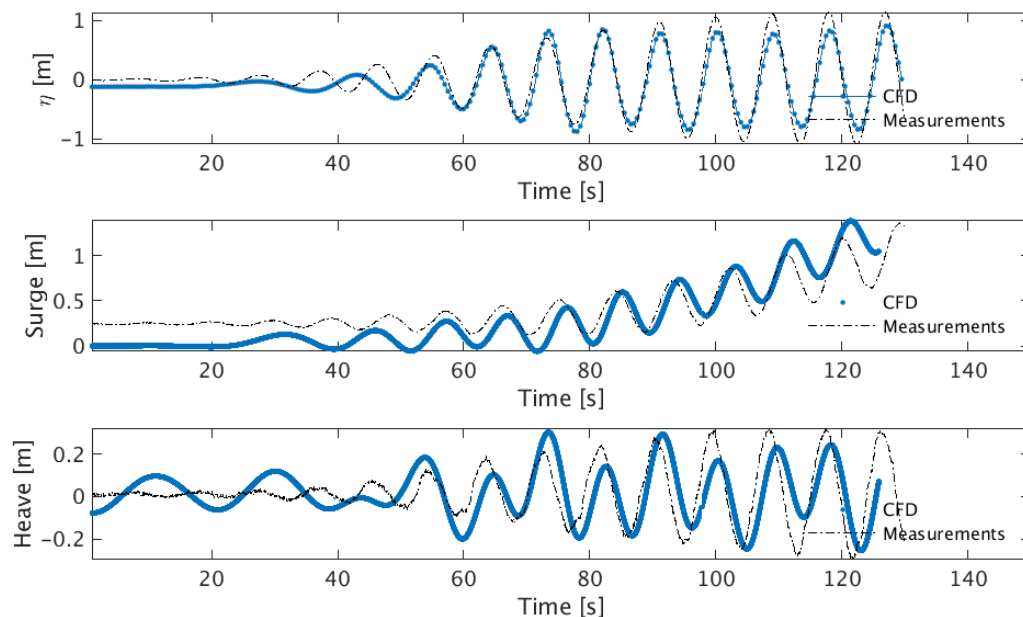


Figure 29: Comparison of the CFD simulations and measurements for test case 4010 based on the wave elevation match. Top: wave elevation, middle: surge amplitude; and bottom: heave amplitude.

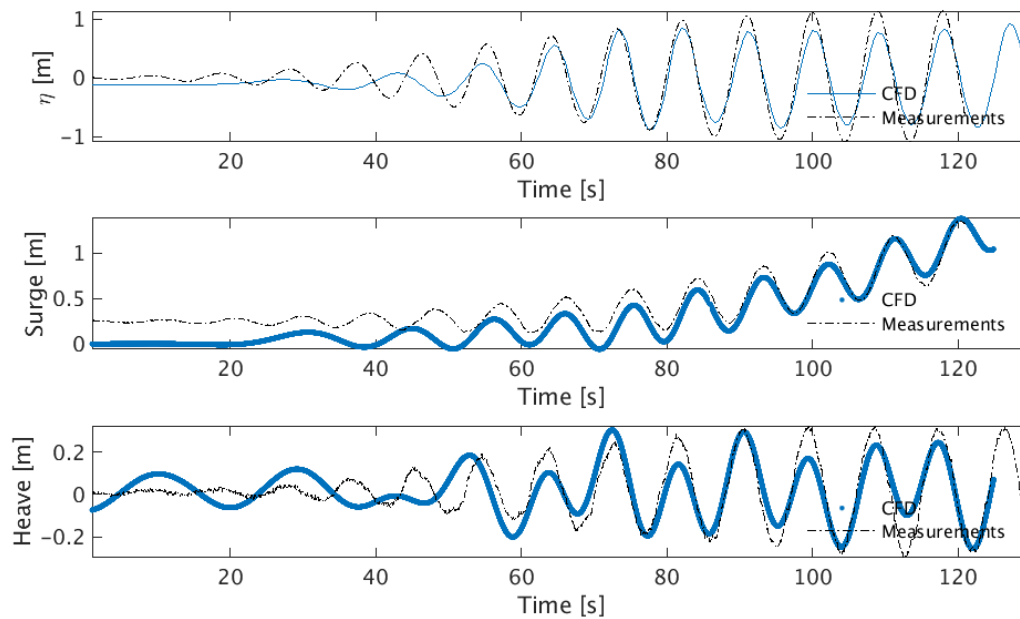


Figure 30: Comparison of the CFD simulations and measurements for test case 4010 based on the surge motion match. Top: wave elevation, middle: surge amplitude; and bottom: heave amplitude.

4.3.3 Effects of slip/no slip boundary conditions

The effect of the boundary condition on the moving body floaters was investigated using the test case 4020 (REG H4.1m, T12.5s) in order to examine the impact on the stability of the simulations. Snapshots of the instantaneous velocity and vorticity magnitudes for both cases are plotted in

Figure 31. Three-dimensional views are presented as an insight into the flow physics around the floater and free surface. These are presented as the top and middle plots and allow to watch the column walls from the inside. The velocity and vorticity magnitude is shown through the walls.

Two-dimensional snapshots are also taken by slicing through one of the pontoons as shown by a dashed line in Figure 24 and aim at looking into vorticity generation around the pontoons. As can be seen, the no-slip wall results in significantly higher vorticity magnitudes near the pontoon which is caused by the shear layer. One should note that the velocities shown here are given in the absolute sense and not relative to the floater velocity. Therefore no-slip here does not necessarily mean zero velocity at the wall. To study the boundary conditions more quantitatively, heave amplitudes and loadings are plotted in Figure 32. As can be seen, no significant impact is seen on the behaviour of the solver by employing a slip-free boundary condition on the walls. While the no-slip conditions can thus provide a closer reproduction of the physical effects in the shear layer, the impact on the global motion is thus found to be very small in the present case. Similar mesh refinement is used for both cases and the grid looks as shown in Figure 21.

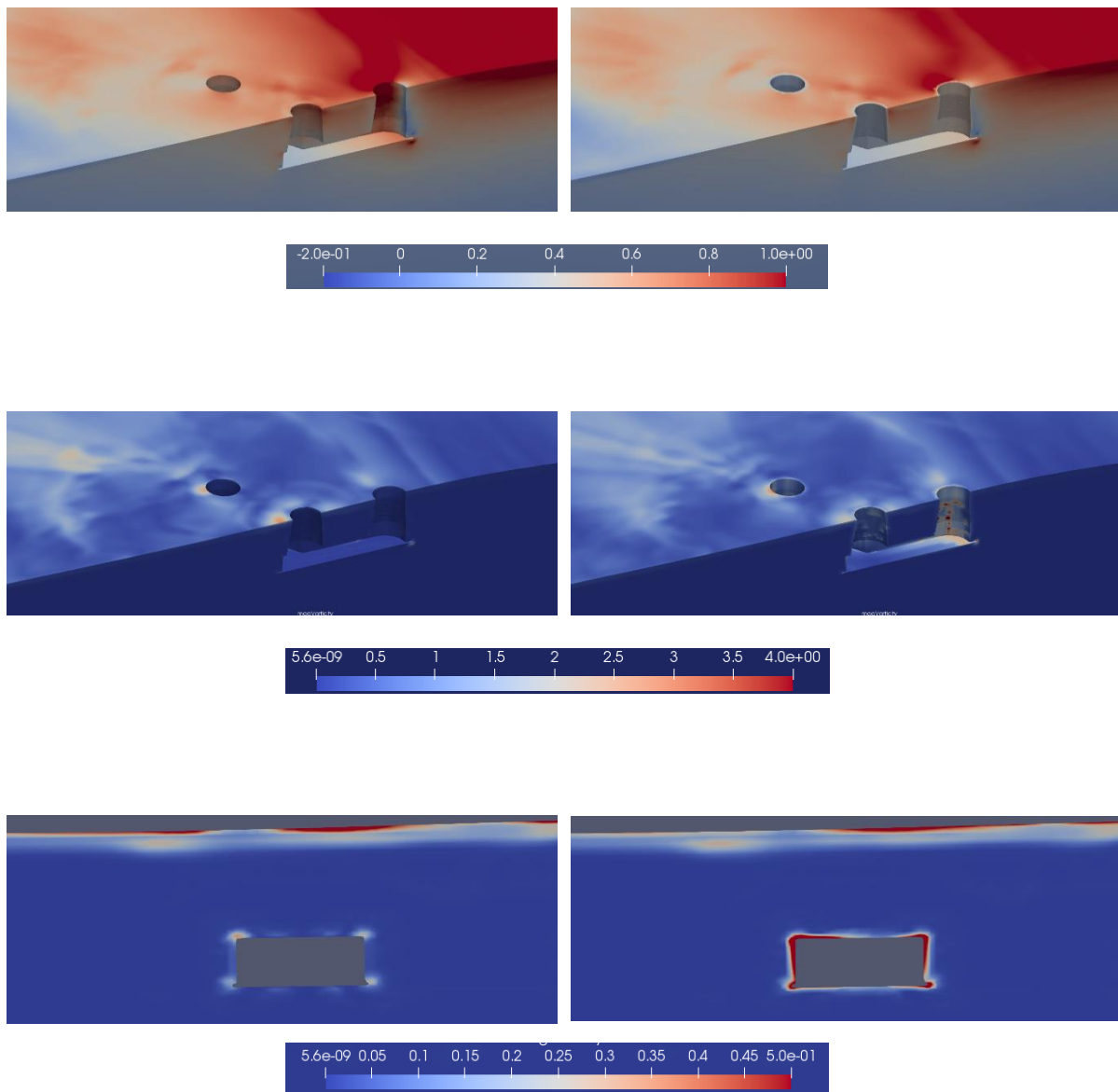


Figure 31: Snapshot of the (top) velocity and (middle and bottom) vorticity magnitudes using left: slip and right: no-slip walls.

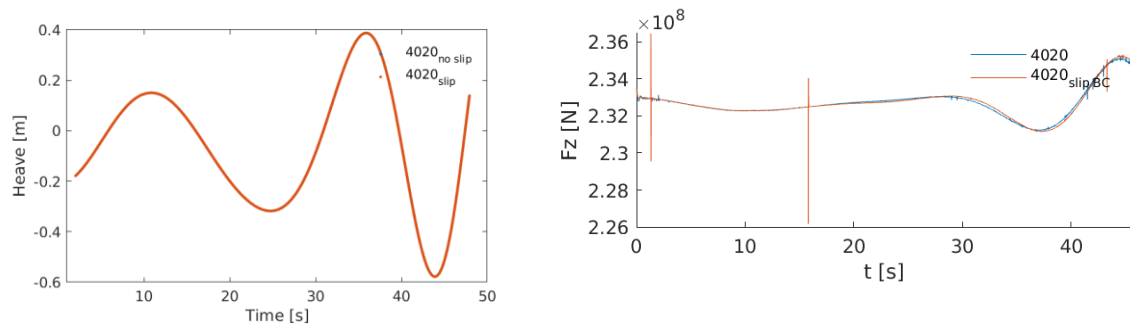


Figure 32: Impacts of slip and no slip boundary conditions on the performance of the CFD solver for the load prediction for Test 4020 (REG H4.1m T12.5). Left: motion amplitudes, right: force magnitude.

4.4 Concluding remarks

To further extend the preliminary results presented in D4.7, CFD simulations were carried out with attention to validation against measurements, wall boundary conditions and mooring analysis. The floater geometry in OpenFOAM was modelled and an unstructured mesh was created using OpenFOAM's snappyHexMesh toolbox.

Simulations of the heave decay tests showed excellent agreement with the experiments. For the test case 4010 ($H=2.1$, $T=9s$), CFD simulations predicted accurate surge response both in high and low frequencies and although there were some underprediction in heave, the heave order of magnitude and frequencies were predicted well. The effects of slip versus no slip boundary conditions were investigated and it was shown that the magnitude of vorticity formed around the floater with no-slip wall boundary condition is higher than the slip wall. However, in terms of the overall effects, the cases do not exhibit a noticeable difference.

The present results are encouraging and demonstrates the potential of CFD for detailed design studies. Yet, as discussed in D4.7 and its accompanying references, the numerical method suffers from well known instabilities, some of which resulting from the weak coupling between the fluid solver and the motion solver in OpenFOAM. Current research in the OpenFOAM community aims at solving these issues.

Focused waves and high sea states often exhibit wave breaking. Quantifying the effects of turbulence modeling is a logical step to better understand and predict such flows. The present project has provided us with a platform to further investigate such sea states and turbulence conditions in our ongoing research.

5 Validation of second-order hydrodynamics in a state-of-the-art model of the NAUTILUS-DTU10

5.1 Introduction

The LIFES50+ Nautilus-DTU10 FOWT (Figure 33) is described in LIFES50+ D4.2 [30] with a correlated FAST model in LIFES50+ D4.5 [29]. As reference, also a publication by Tecnalia R&I and Nautilus Floating Solutions contains simulation results [31].

In section 4 of Deliverable 4.6, a tuned model of the Nautilus-DTU10 floating wind turbine was created in FAST8. The hydrodynamics of the computer model include first order radiation-diffraction hydrodynamics (added mass, radiation damping and wave diffraction forces) calculated in WAMIT. Additionally, Morison damping elements for representation of the columns and the pontoon of the floating platform were included to take into account the viscous damping. Similar numerical models including second order terms were presented in [31].

Second order nonlinear drift forces were represented in D4.6 through Newman's approximation [32]. The approximation assumes low rigid-body natural frequencies of the FOWT, such that the difference frequency $\delta_{ij} = \omega_i - \omega_j$ is small and ω_i and ω_j are close to the diagonal of the QTF. The assumption of small natural frequencies holds for the surge degree of freedom (DOF) but potentially not anymore for the pitch-DOF at 0.032Hz. Even though the design of the FOWT will demand its natural frequencies outside the range of the wave frequencies, the natural frequencies often coincide with the frequencies of the drift forces, leading to high excitations, especially of the mooring system [33], [34].

The following sections will thus show a comparison of model test results with a state-of-the-art simulation tool for validation purposes. The scaled model test campaign referred to here is that of the Nautilus-DTU10 presented in [35]. The scaled turbine can be seen in Figure 33.



Figure 33: NAUTILUS-DTU10 scaled model in the wave basin at SINTEF [30].

The Morison drag model and especially the discretization of the platform for the computation of drag forces was iterated from the description of D4.2 [30], D4.5 [29], D4.6 [4] to the present deliverable. A difficulty for the discretization is that FAST v8 [36] does assume circular horizontal surfaces to which the drag force nodes are coupled. The Nautilus-DTU10 FOWT, however, has rectangular pontoons.

In D4.5, a single central node and four eccentric nodes were defined with modified areas to obtain the generalized drag forces on the platform, which would match the real drag of the members. They provide damping forces in the vertical and horizontal directions. The tuning of the model was done to match the decay frequencies and damping of the experiment [37]. While this approach is well suited for the drag-induced damping, it does not model the drag-induced wave forces.

In D4.6, the platform drag discretization was created with 4 different coefficients of drag to represent the horizontal and vertical components of drag on the columns and pontoon of the platform. To model the rectangular pontoons through circular drag elements, the projected area from the bird's eye view of the pontoon has been discretized into circles of 10.5m in diameter. The circular area of the column and the circular areas of the pontoon have been assigned two different vertical coefficients of drag. The areas can be seen in Figure 34.

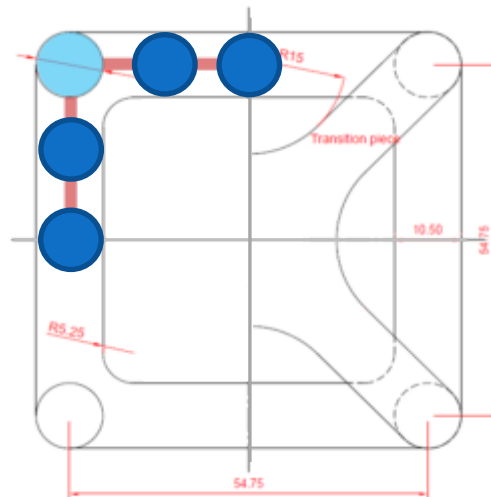


Figure 34: Birds eye view section of the platform. One quarter of the representation of the Modified Morison element model. Coloured areas represent modifications to modelling of the pontoon of the Nautilus platform for FAST.

The thickness of the pontoon is taken as the diameter for a cylinder (2m) in the simulation model, which connects the columns and has a horizontal coefficient of drag. This would be the red line in Figure 34. The vertically oriented columns, which are also modeled as cylinders (10.5m in diameter), have a different horizontal coefficient of drag. In D4.6, the values of the coefficients were tuned to the decay tests of the platform. The following table shows the values of the frequencies and damping coefficients after tuning the model to the decay tests performed in the model test [35].

Table 5-1: Tuned properties after decay tests from D4.6.

	Modified Morison Model	Test	Percentage deviation
Moored Yaw frequency (Hz)	0.0100	0.0110	10.0%
Moored Pitch frequency (Hz)	0.0322	0.0314	2.5%
Moored Heave frequency (Hz)	0.0511	0.0527	3.1%
Moored Surge frequency (Hz)	0.0082	0.0079	3.6%
Damping coefficient column heave plates vertical (Cd vertical column)	78.05	-	-
Damping coefficient pontoon heave plates vertical (Cd vertical pontoon)	12.95	-	-
Damping coefficient column lateral (Cd horizontal column)	0.715	-	-
Damping coefficient heave plate/pontoon lateral (Cd horizontal pontoon)	2.05	-	-
Specific weight mooring lines (kg/N)	157.14	-	-

The decay-tuned numerical model was compared to the scaled model tests of [35]. For the scaled model tests, experimental results of irregular extreme wave and pink noise tests show that there is a significant excitation in the low frequency range (lower than the wave frequencies) which can be attributed to the second order drift forces, see D4.6 [4].

Several of the recent experiments in the FOWT community have shown that the low-frequency resonances of FOWTs are often under-predicted by numerical models. In the OC5 [38] project, most participant codes could not model the low-frequency motion amplitudes. For the TripleSpar platform, which was used in the initial deliverables of LIFES50+, a load-case dependent drag of the members made it possible to obtain a numerical response, comparable to the experimental data [16]. The load-case dependency of the drag is due to the variation of the Reynolds and Keulegan-Carpenter numbers for the different submerged members. An iteration of the response with parameterized drag coefficients, as function of KC was done in LIFES50+ for the TripleSpar platform [39].

5.2 Comparison of decay tuned model for different hydrodynamics modelling approaches

The FOWT was tested in the wave basin under a variety of conditions. Different tests are used for comparison purposes for these sections. The properties of the test are shown in Table 5-2. The model is rotated with 15 degrees relative the incoming waves.

Table 5-2: Subset of environmental conditions selected for this study. No wind was applied for these tests.

Test Number	Case	Spectrum	H_s [m]	T [s]	Test duration [s]
4210	Pink noise	Pink noise	2.0	4.5-18.2	11880
4220	Pink noise	Pink noise	4.0	4.5-18.2	11880
6241	DLC 1.6	Pierson-Moskowitz	10.9	15	11880
6270	DLC 1.6	Pierson-Moskowitz	7.7	12.4	11880

In Deliverable 4.6, comparisons of the experimental data with the numeric models with Newman's approximation have been shown. It is seen that the FAST8 model with Morison elements with no second order forces cannot approximate the low frequency response in heave, surge, sway, pitch, roll, and yaw (see Figure 35). Once the 2nd-order slow-drift forces, computed with Newman's approximation with the nearfield mean drift coefficients are used in the model, the response of the surge, yaw and sway in the low frequency range is shown. For the case of the irregular wave Test6270 with extreme waves, the decay-tuned model with Morison elements under-predicted the frequency response of all platform degrees of freedom for frequencies below the wave frequencies (below 0.04Hz). For the pink noise Test4220 the response of the surge and sway showed good agreement. But for heave, pitch, roll and yaw, the response for frequencies below the wave frequencies was under-predicted.

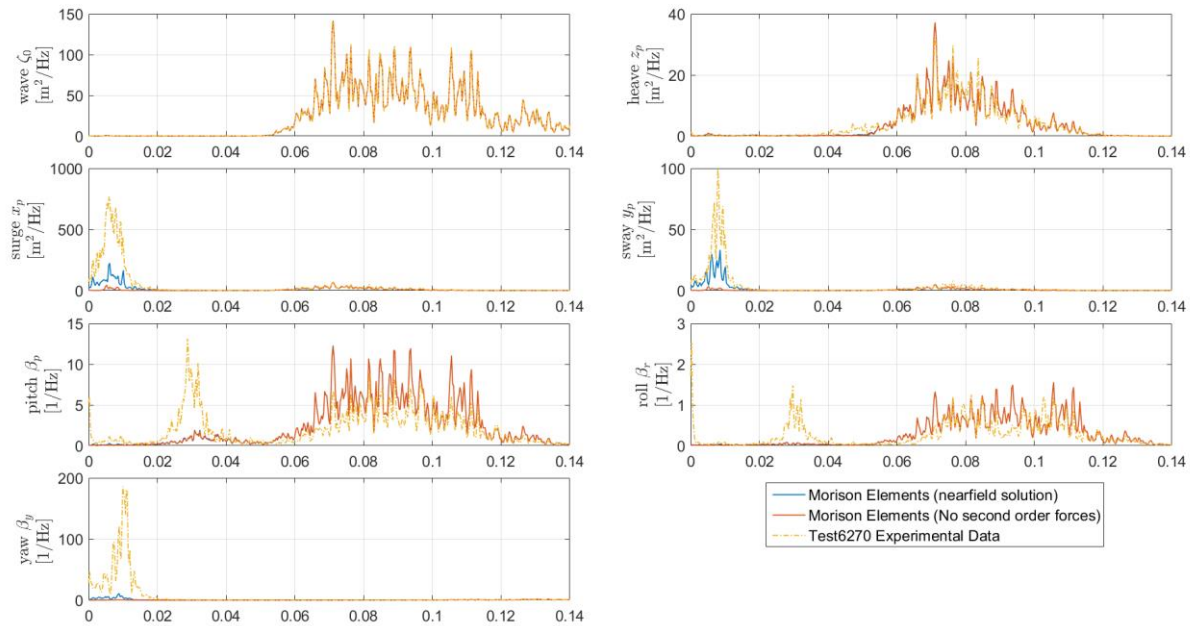


Figure 35: Comparison in the frequency domain of the simulation with experimental data for different FAST models for Test 6270. The x-axis is in Hz.

Newman's approximation, used in D4.6 for the second order forces, provides the advantage of not being as computationally expensive as determining the full quadratic transfer functions for the slow and mean drift forces. However, it is necessary to investigate if better results can be obtained for the Nautilus-DTU10 model with the more computationally expensive difference full quadratic transfer functions. The implementation of the second order forces and the difference full quadratic transfer functions in FAST8 is outlined by Duarte et al. in [40]. Work from [41] has also investigated the implementation of the QTFs on the models

5.3 Newman approximation and QTF results

The following graphs of

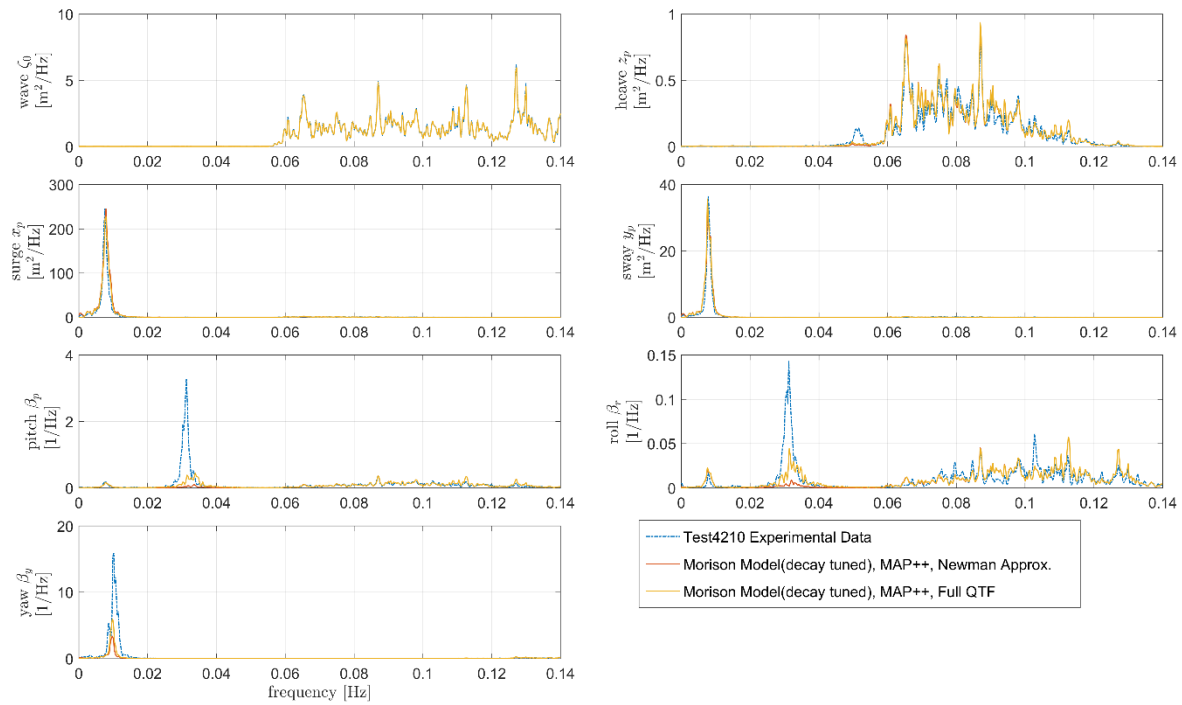


Figure 36 - Figure 37 show the frequency-domain response of the different platform degrees of freedom for the simulations as compared to the scaled model test. Here the coefficients of drag used have been obtained by tuning to the decay tests. Different approaches are shown for the implementation of second order wave forces on the platform. The test corresponds to an input pink noise wave spectrum as previously described.

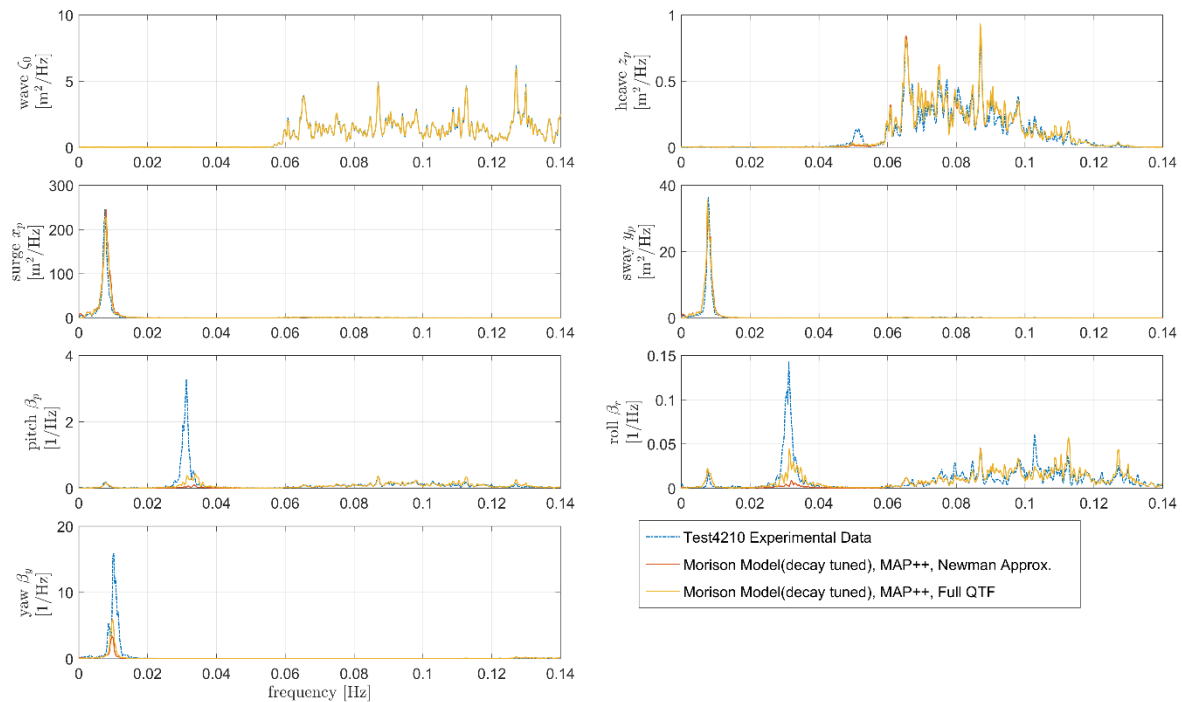


Figure 36: Response in the frequency domain of the simulation with MAP++ mooring model for Test 4210.

The simulation models for the test case with the pink noise wave spectrum show good agreement of the heave response for the frequency range of the waves (above 0.06Hz). Good agreement is also seen for the case of the surge and sway degrees of freedom in both the cases of the Newman approximation and the full QTFs simulations. For the cases of the heave, pitch, roll and yaw, there is an underestimation of the excitation of the degrees of freedom at the low frequency ranges, even though the simulation with full QTFs does show an increased response in comparison with that using Newman's approximation.

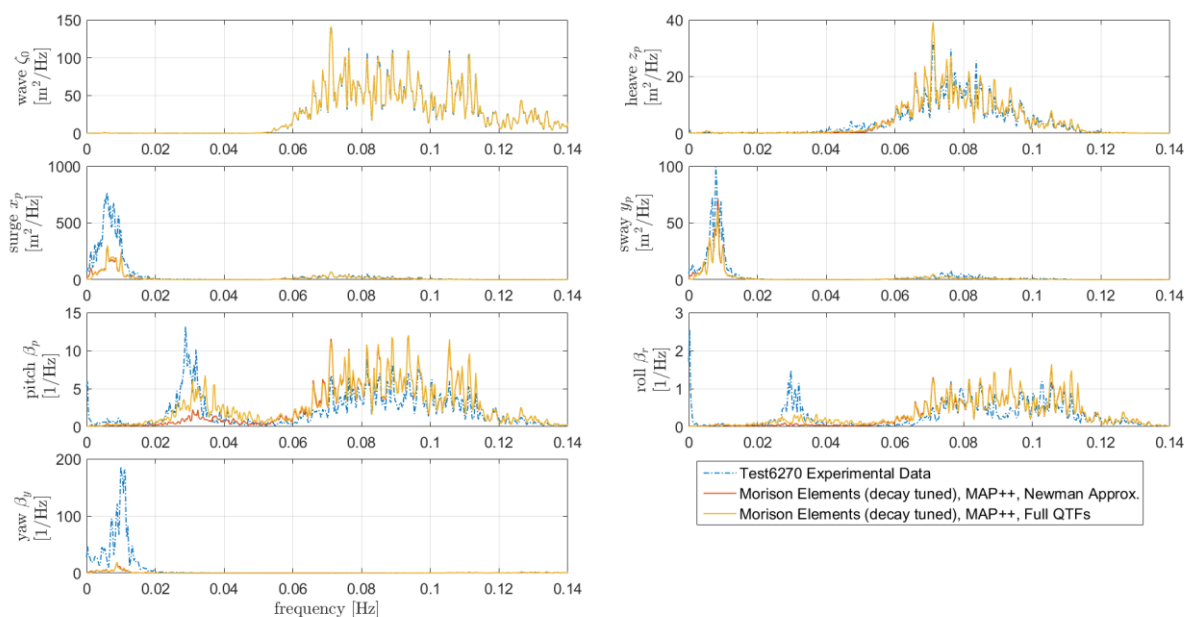


Figure 37: Response in the frequency domain of the simulation with MAP++ mooring model for Test 6270.

Figure 37 shows the case of Test6270 with extreme waves as described in [35]. In this case, as opposed to the pink noise test, the response in the surge, sway and yaw direction are underestimated, both by the simulation with Newman's approximation and with full QTFs. For the low-frequency region of the pitch and roll response, the same case is seen as the pink noise test, were both approaches underestimated the response for the decay-tuned models. For the region of the wave excitation frequencies, the response of the heave, pitch and roll is substantial, and for the pitch and roll, they are comparable to the response at their respective natural frequencies of the platform. The yaw response here is large but the decay tuned model does not show much response in the same region.

5.4 Sensitivity of Morison drag coefficients in decay tests

The decay-tuned model showed that the excitation of the simulation model with irregular waves was too low at the natural frequencies of the model when comparing to the test results. Tuning the global coefficients of damping of the model with the decay tests needs involves taking into account the amplitude of motion [42].

Figure 38 shows an exemplary comparison of the decay test with the simulation data as presented in D4.6. Here, tuning has been done by changing the vertical coefficients of drag of the areas representing the pontoon and the columns. Trying to match the linear and quadratic damping through Morison elements only, can thus introduce some deviations from the experimental results.

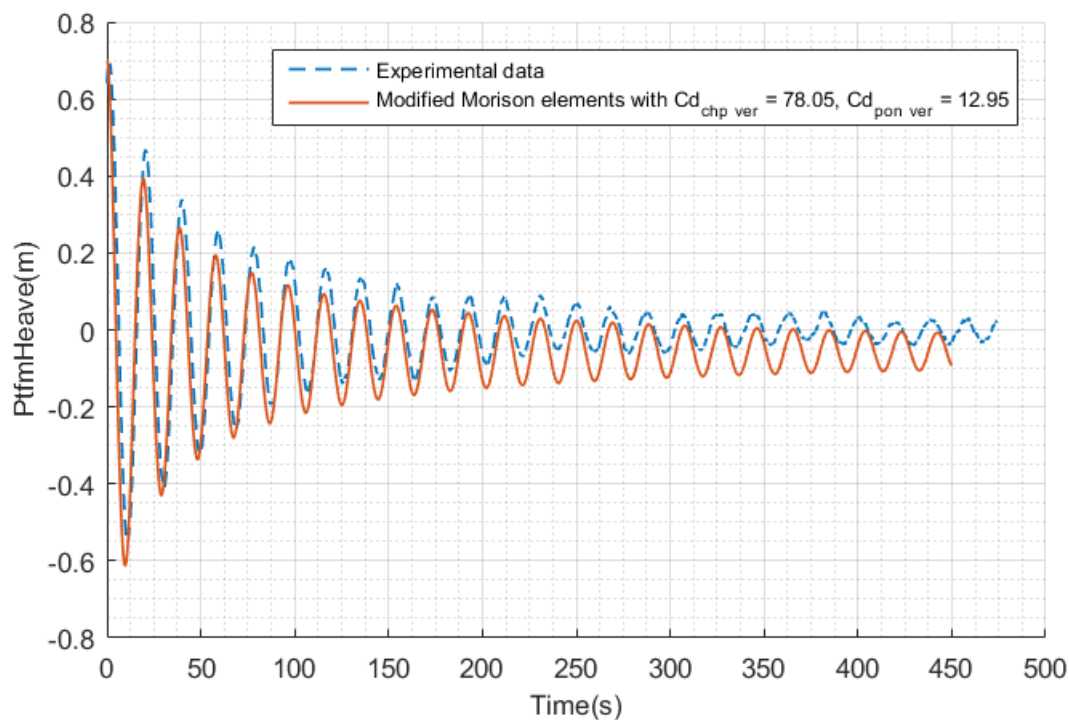


Figure 38: Comparison of moored heave decay simulation with experimental data

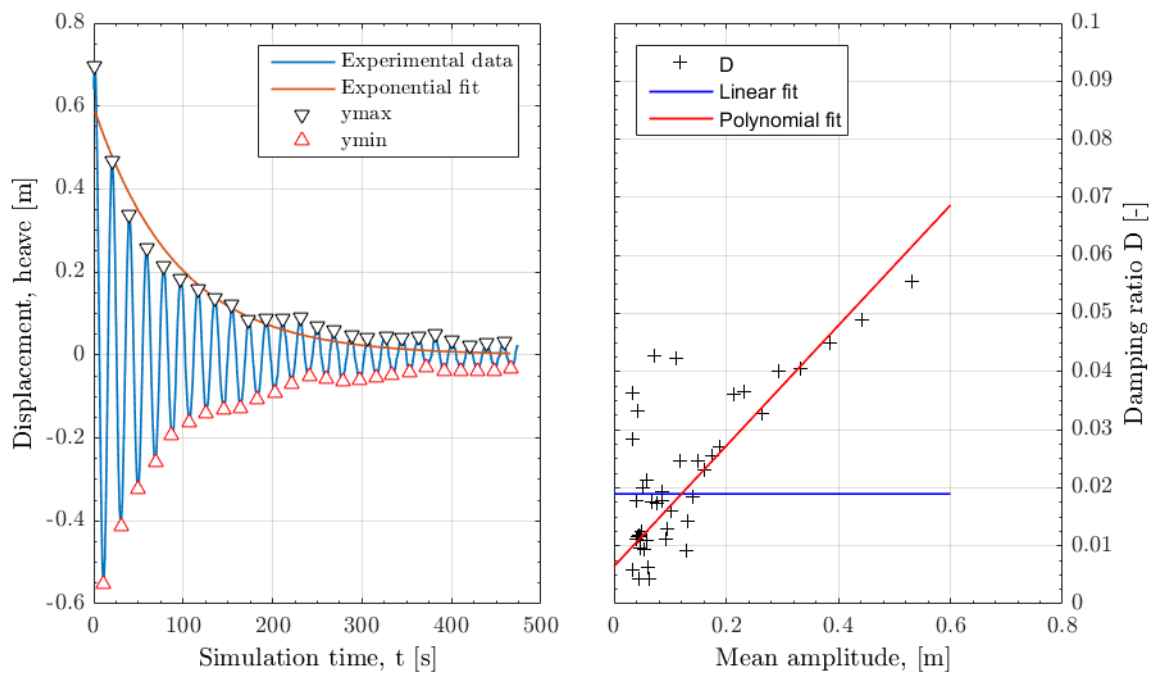


Figure 39: Calculation of damping ratio based on maximums of the experimental data for the heave decay test

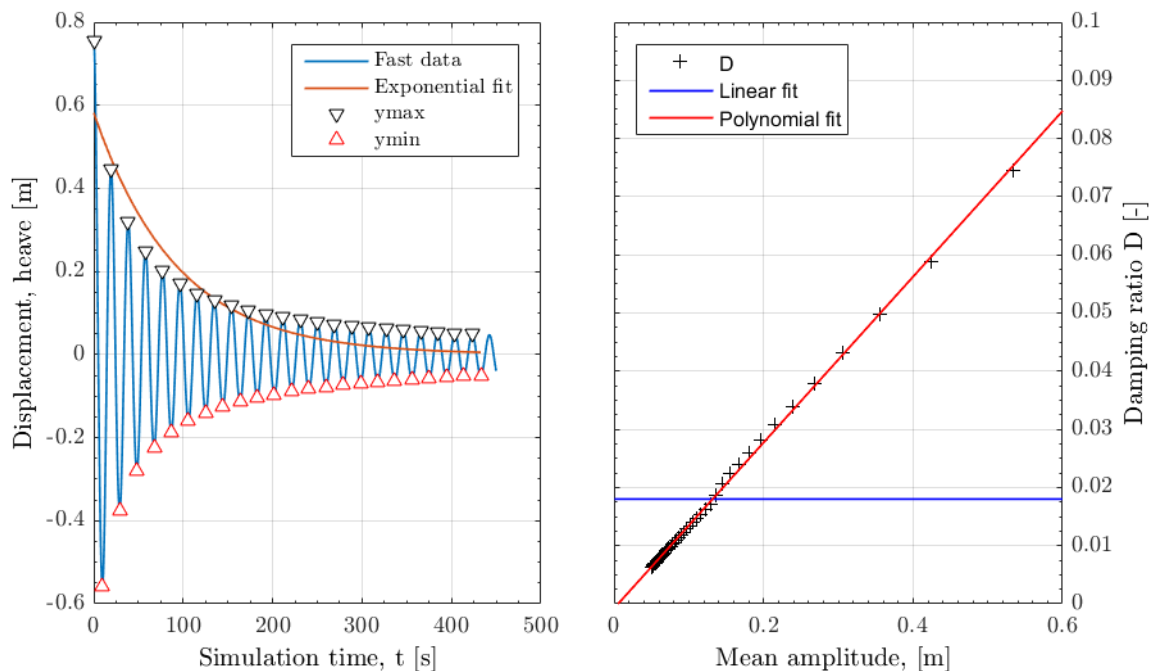


Figure 40: Calculation of damping ratio based on maximums of the FAST simulation data shown in Figure 38 for the heave decay test

In the left side of Figure 39 one can see a best fit estimate of an exponential function to the decay data from the wave basin tests for the moored heave decay. On the right side, one sees the damping ratio as a function of the mean amplitude of the decay motion for each period of oscillation. Here, a constant damping ratio (blue line) would represent a system with only linear damping. However, the scattering

of the data shows the non-linear behaviour of the damping of the system. The scattering also shows the difficulty to fit experimental data to that of the simulations (shown in Figure 40).

The effect of changing the coefficients of drag of the Morison elements in the vertical and horizontal directions, as well as the case-dependency of the coefficients used will thus be shown in the following sections. As opposed to D4.6 [4], the following results do all include the full QTF, instead of Newman's approximation.

5.5 Test 4210 Pink Noise – $H_s=2$ m, $T_p = [4.5, 18.2]$ s

The first case examined is that of the pink noise spectrum. As results shown in

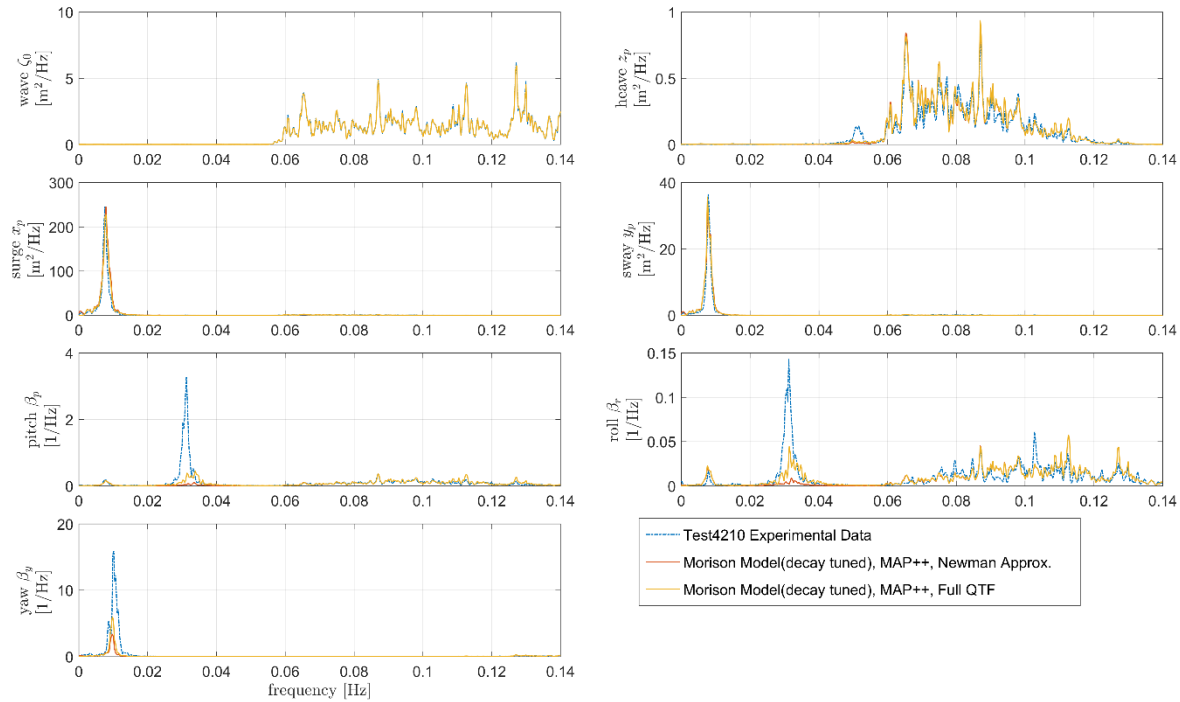


Figure 36 have not been able to reproduce the pitch motion at the low frequency range, the coefficients of drag in the vertical direction are now modified. The results of the changes are shown in Figure 41.

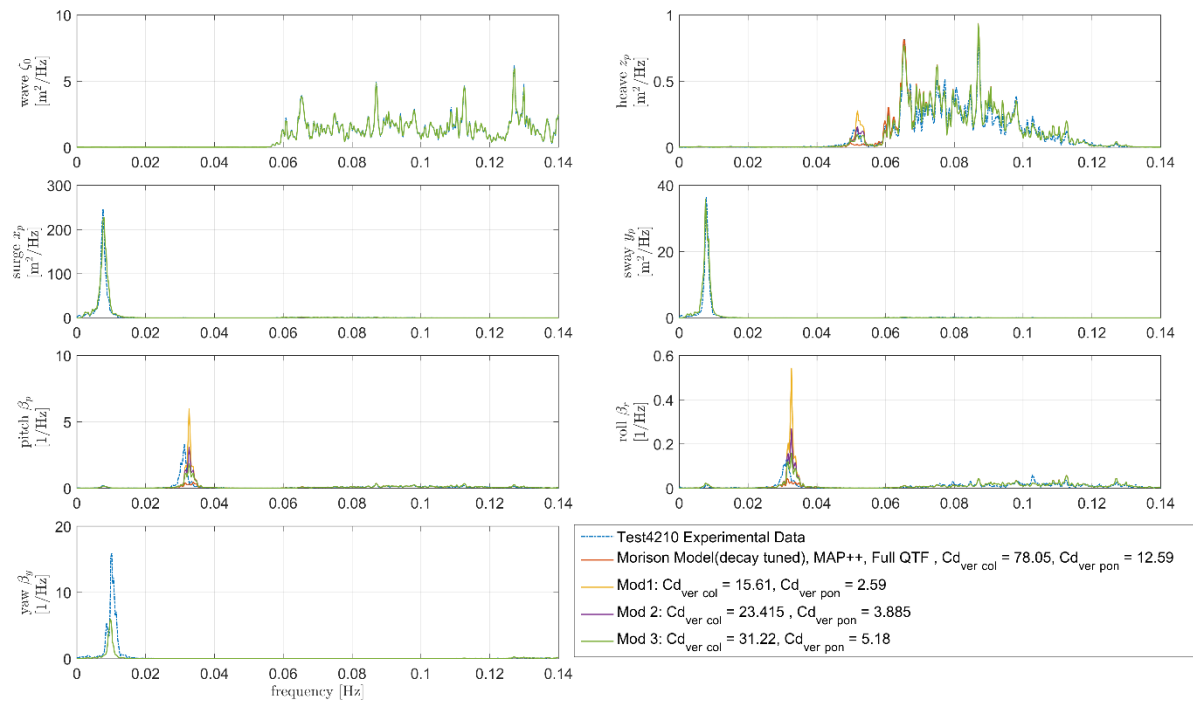


Figure 41: Sensitivity of the response in the frequency domain of the simulation with MAP++ mooring model for Test4210 for changing coefficients of drag in the vertical direction.

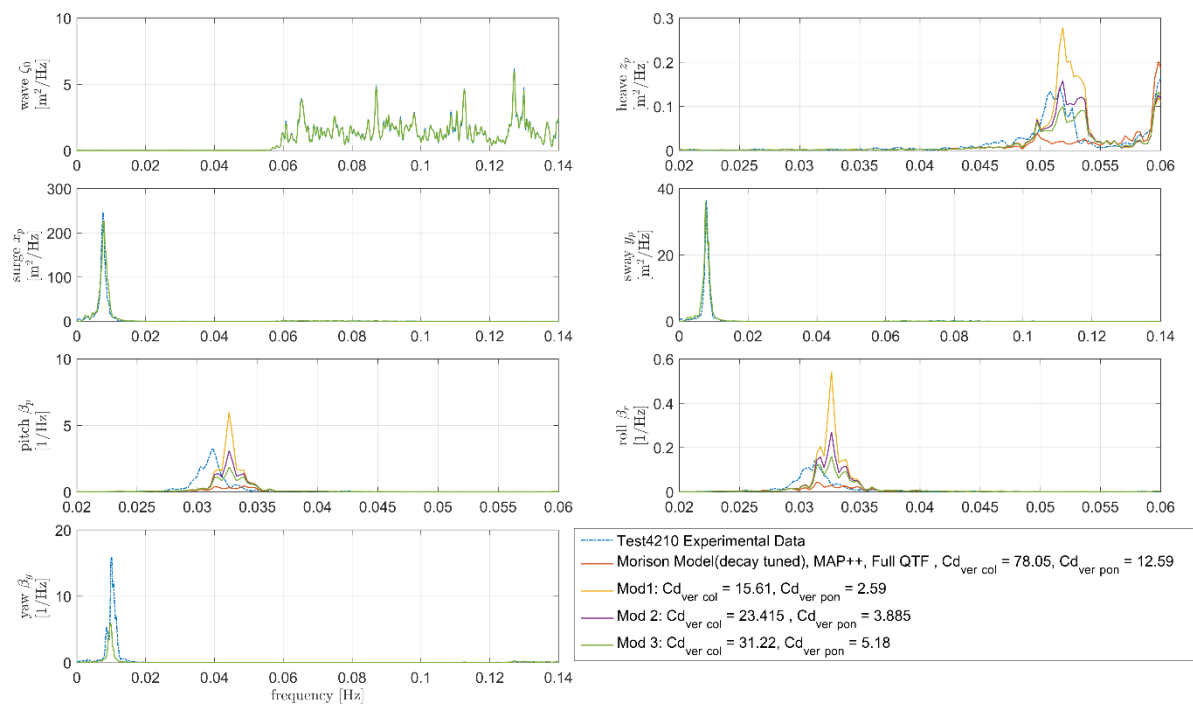


Figure 42: Close up of the sensitivity of the response in the frequency domain of the simulation with MAP++ mooring model for Test4210.

For comparison purposes, the standard deviation of each of the signals is presented in Table 5-3.

Table 5-3: Standard deviation (STD) of the platform motions for Test4210

Model	Cd _{ver col}	Cd _{ver pon}	STD Surge (m)	STD Sway (m)	STD heave (m)	STD Roll (°)	STD Pitch (°)	STD Yaw (°)
Experimental data	-	-	0.694	0.240	0.116	0.039	0.121	0.208
Modification 1 (yellow)	15.61	2.59	0.743	0.264	0.121	0.043	0.128	0.146
Modification 2 (blue)	23.415	3.885	0.743	0.264	0.120	0.040	0.117	0.146
Modification 3 (green)	31.22	5.18	0.743	0.264	0.120	0.039	0.111	0.146
FAST8 Morison model, decay tuned	78.05	12.59	0.743	0.264	0.121	0.036	0.099	0.146

Important to note is that the mean has been removed from the signal before calculating the power spectral density and the sum of its area.

The results in the close-up of the heave, surge and roll in Figure 42 show the excitation of the respective natural frequencies. The highest values of damping are those used in the decay tuned model. As the damping in the vertical direction gets smaller, the increase in the excitation of the second order forces around the natural frequency is evident.

However for heave, as seen in table from the almost none changing value of the STD, the response around its natural frequency is small compared to that seen at the wave excitation frequencies.

5.6 Test6241 DLC1.6 – PM, $H_s = 7.7\text{m}$, $T_p = 12.4\text{s}$

Similarly, the irregular wave Test 6421 has been analysed. First the effect of the horizontal coefficients of drag is tested. As results shown in Figure 43 and Figure 44, increase the coefficients of drag in the horizontal direction lowers the response around the natural frequency of the surge and sway response, as was the case of the pink noise test4210. The best fit for surge is the solid blue/purple line (with Cd hor col = 0.5125 and Cd hor pon = 0.1787). In this case the sway is a bit over predicted, but the response in sway is much lower than that in surge. The yaw, however would be completely under predicted. The yaw shows large excitation, much larger than the pitch and roll in the low frequency range. It is not clear in this case, if this excitation is due to the fact that the tests are done with a 15° wave misalignment with respect to the platform. Nevertheless, it shows that neither the yaw nor surge excitations are able to be reproduced with the same coefficients of drag for this particular case.

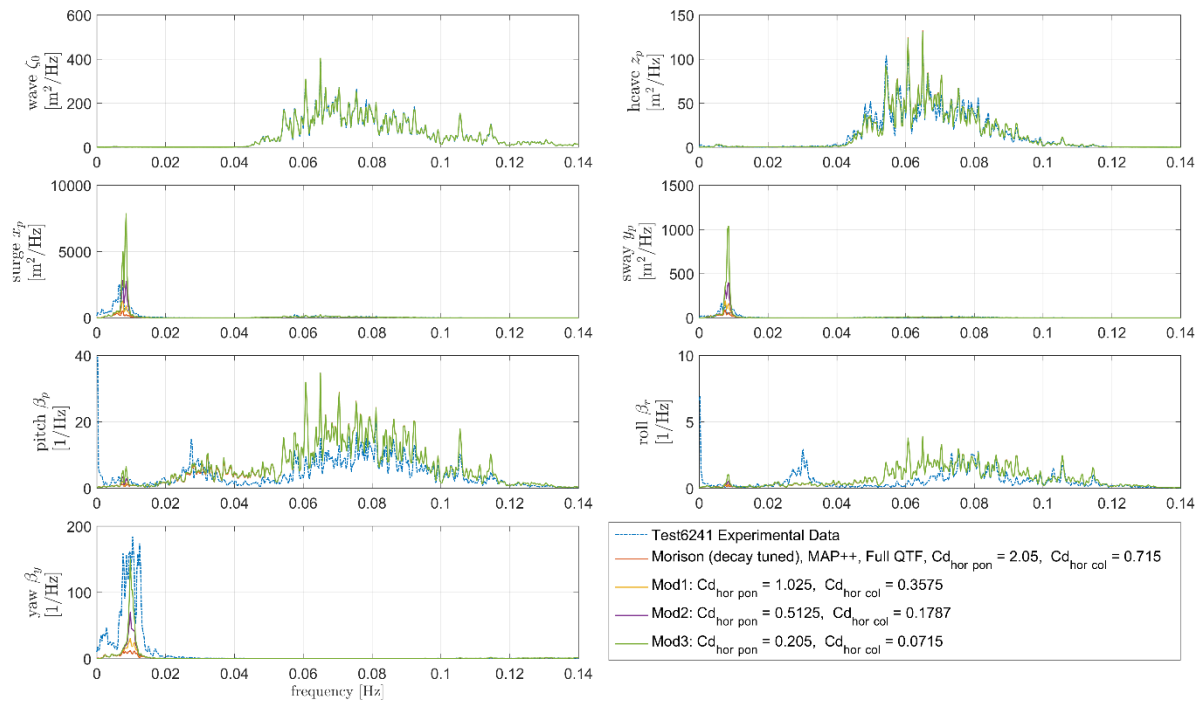


Figure 43: Sensitivity of the response in the frequency domain of the simulation with MAP++ mooring model for Test6241 for changing coefficients of drag in the horizontal direction.

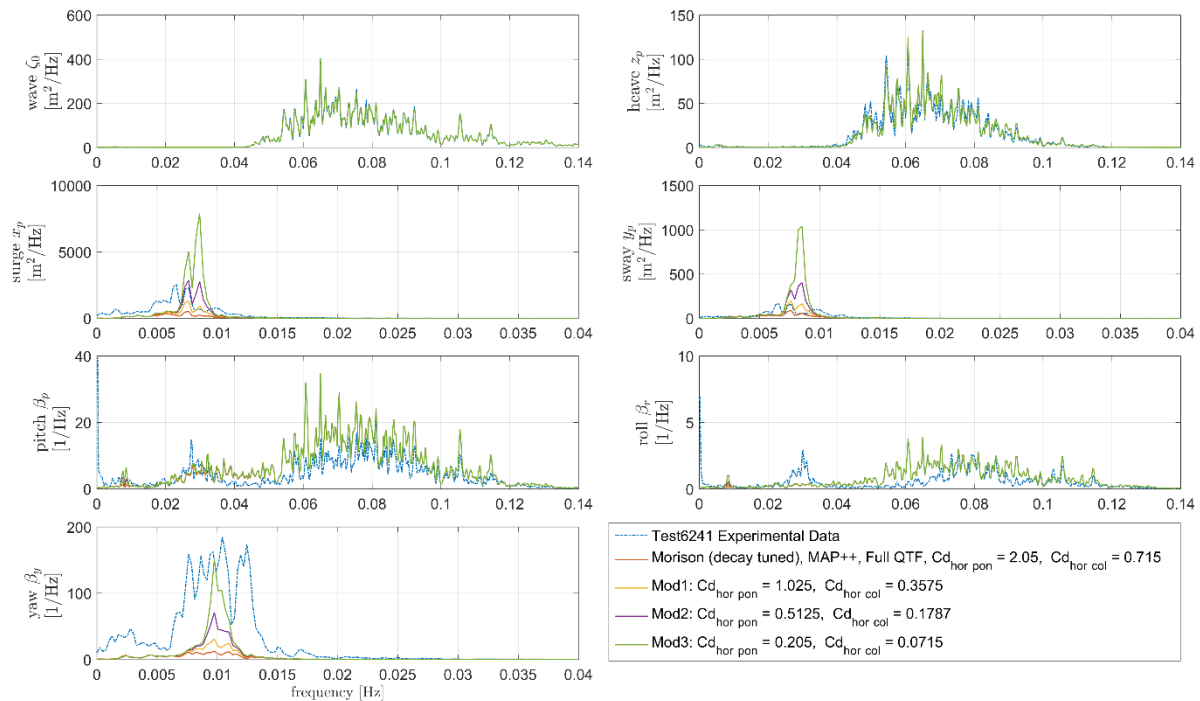


Figure 44: Close up for the sensitivity of the response in the frequency domain of the simulation with MAP++ mooring model for Test6241 for changing coefficients of drag in the horizontal direction.

For comparison purposes, the standard deviation of each of the signals is presented in Table 5-4.

Table 5-4: Standard deviation of the platform motions for Test6241 and the modifications to the model

Model	$C_{d_{hor\ pon}}$	$C_{d_{hor\ col}}$	STD Surge (m)	STD Sway (m)	STD heave (m)	STD Roll (°)	STD Pitch (°)	STD Yaw (°)
Experimental data	-	-	3.645	0.962	1.385	0.270	0.766	1.074
FAST8 Morison model, decay tuned	2.05	0.715	2.218	0.703	1.393	0.318	0.944	0.385
Modification 1 (yellow)	1.025	0.3575	2.547	0.835	1.392	0.318	0.947	0.439
Modification 2 (blue)	0.5125	0.1787	3.048	1.003	1.392	0.319	0.949	0.507
Modification 3 (green)	0.205	0.0715	3.812	1.254	1.391	0.320	0.951	0.597

Important to note is that the mean has been removed from the signal before calculating the power spectral density and the sum of its area.

As with the figures before, the sensitivity to the horizontal drag values is shown in Table 5-4 for the surge, sway and yaw degrees of freedom. Import to point out is that a factor 10 decrease in the horizontal drag coefficient still is not sufficient to be able to reproduce the yaw excitation.

Now the effect of the vertical coefficients of drag is looked at. This showed to have a more complex behaviour, as the excitation in the pitch and roll also are large in the region of the first order wave excitation frequencies.

Figure 45 shows that as the values of the vertical drag coefficients are lowered, two effects can be seen on the response of the pitch and roll. First, for the region around the natural frequency (lower frequency than that of the wave excitation) the lowering of the coefficients of drag lead to an increase in excitation. However, the opposite is seen for the range of the wave excitation, where the lowering of the drag coefficients lead to a decrease in the response. This coupled effect is subject to the publication [15].

The response of the heave for this irregular sea state with large waves and long periods show to have not been affected much by the changing of the damping parameters in this case.

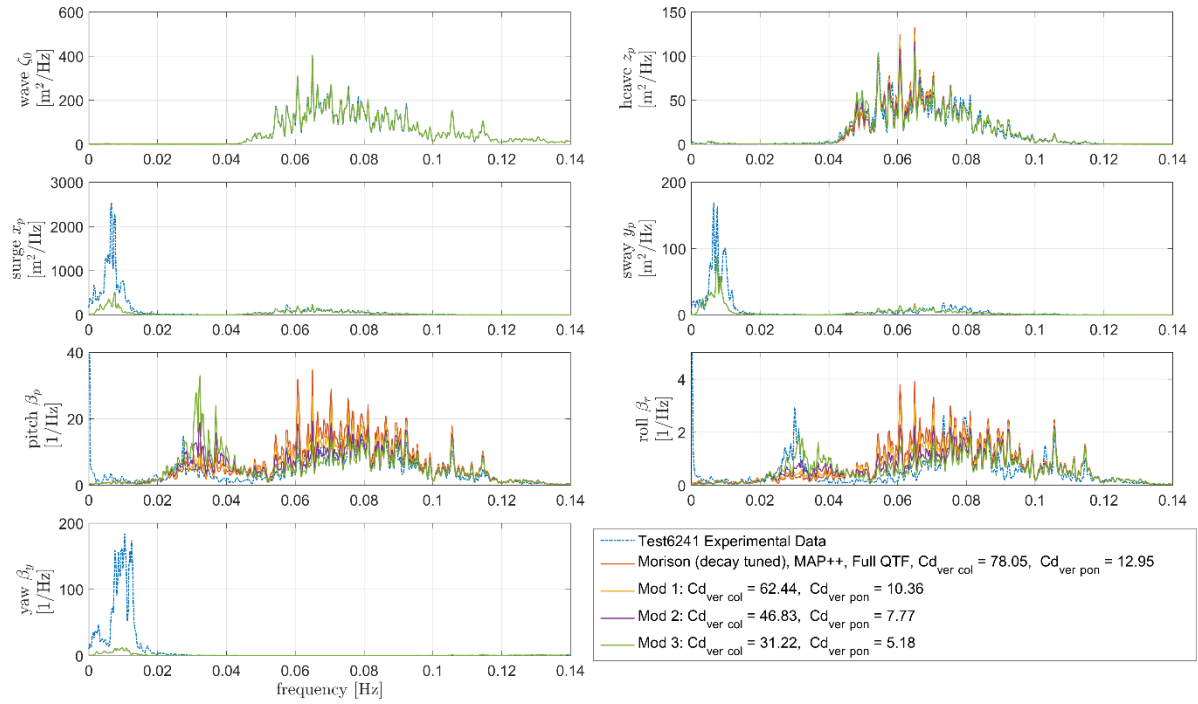


Figure 45: Sensitivity of the response in the frequency domain of the simulation with MAP++ mooring model for Test6241 for changing coefficients of drag in the vertical direction.

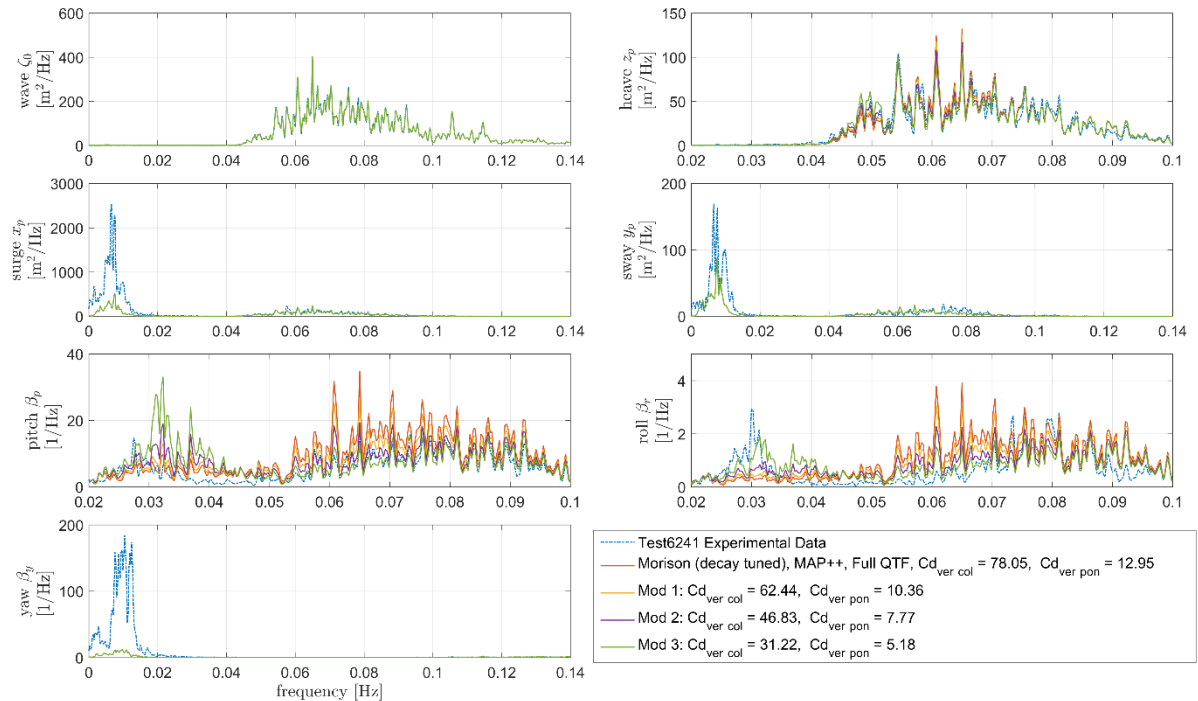


Figure 46: Close up of sensitivity of the response in the frequency domain of the simulation with MAP++ mooring model for Test6241 for changing coefficients of drag in the vertical direction.

For comparison purposes, the standard deviation of each of the signals is presented in Table 5-5.

Table 5-5: Standard deviation of the platform motions for Test6241 and modifications to the vertical coefficients of drag of the model

Model	$C_{d_{ver\ col}}$	$C_{d_{ver\ pon}}$	STD Surge (m)	STD Sway (m)	STD heave (m)	STD Roll (°)	STD Pitch (°)	STD Yaw (°)
Experimental data	-	-	3.645	0.962	1.385	0.270	0.766	1.074
FAST8 Morison model, decay tuned	78.05	12.95	2.218	0.703	1.393	0.318	0.944	0.385
Modification 1 (yellow)	62.44	10.36	2.217	0.702	1.387	0.302	0.894	0.385
Modification 2 (blue)	46.83	7.77	2.216	0.701	1.379	0.288	0.855	0.384
Modification 3 (green)	31.22	5.18	2.213	0.699	1.374	0.280	0.844	0.383

Important to note is that the mean has been removed from the signal before calculating the power spectral density and the sum of its area.

Table 5-5 shows that the coefficients of drag considered in the vertical direction have relatively low influence on the overall response of the platform in the heave, roll and pitch direction for the case of extreme irregular waves. For the pitch and roll though, from Figure 45 it is seen that, even if the low frequency response is increased by a lowering of the coefficients of drag in the vertical direction, the response to the wave frequencies is then decreased. For the pitch and roll, the shape of the PSD of the numerical models in the first-order wave frequency range gets closer to the experimental one with lower drag coefficients.

If one would try to quantify which coefficients of drag would best fit the measurement data from the given sensitivity plots for the cases of the pink noise test and the extreme irregular waves test, one would have to weigh several factor that come into play. Such factors could be the overall response, the response at the natural frequencies, or the response of the different degrees of freedom.

Table 5-6: Summary of fitted coefficients of drag for the given tests.

Model	$C_{d_{ver\ col}}$	$C_{d_{ver\ pon}}$	$C_{d_{hor\ col}}$	$C_{d_{hor\ pon}}$
FAST8 Morison model, decay tuned	78.05	12.95	0.715	2.05
Sensitivity study of Test4210 in horizontal Cd	23.415	3.885	unchanged	Unchanged
Sensitivity study of Test6241 in for vertical Cd	31.22	5.18	Unchanged	Unchanged
Sensitivity study of Test6241 for horizontal Cd	Unchanged	Unchanged	0.0715	0.205

Table 5-6, as well as the figures shown for the analysis of this section, exemplify the difficulty of properly defining the coefficients of drag for the different tests, as well as the fact that the coefficients that would be appropriate for the decay tests, cannot be used to properly reproduce the excitation of the platform in irregular sea states. Further work is necessary to define the drag coefficients, appropriate for the different flow conditions.

5.7 Computational Time

An additional factor to consider when using the solutions from implement Newman's approximation and the Full QTFs is the computational time of the simulation in FAST8. With a CPU Intel(R) Xeon(R) E5645 with 2.40GHz, the pre-processing of the mean- and slow-drift 2nd-order forces with Newman's approximation needs about 4 minutes, while for the full difference-frequency 2nd-order forces computed with full QTF took about 35 min. This pre-processing is done by Hydrodyn part of FAST8. The 11800 second simulation itself took another 50min approximately for both methods.

There is also additional time needed to compute the QTFs themselves, which comes from the panel code software used, for example WAMIT or Ansys AQWA. At the moment no information is had on the time needed for this calculation. Also, important to remember is that for every wave heading there needs to be a new set of QTFs calculated which does not directly affect the simulation time in FAST8 but does affect the overall time needed to perform a simulation study.

5.8 Conclusion

For the analysis presented in these sections, the difference frequency full QTF were used in order to try to better represent the response of the floating platform scaled experimental test of the NAUTILUS-DTU10 FOWT. This in contrast to D.4.6 which had focused on modelling the second order effects with Newman's approximation. In summary, the following findings were obtained:

- The use of difference frequency full QTF increased the response of the platform for the low frequency region (below the wave excitation region), especially for pitch and roll, when compared to Newman's approximation for the second order excitation forces. The response in this low frequency region for the extreme irregular wave test, for the decay tuned model, was however below that of the experimental data. A better comparison was achieved for the surge and sway degrees of freedom under the pink noise test, but the simulation still under-predicted the response in for the low frequencies of the other degrees of freedom
- The sensitivity analysis of the vertical coefficients of drag for the pink noise tests with the full QTF model showed that the numerical model could approximate the test response well for all degrees of freedom except the yaw. Large excitation in the low frequency range of the test results of the yaw degree of freedom could be due to the -15-wave direction. The reason why the model cannot capture this excitation is not clear. For the pitch and roll degrees of freedom, the response of the low frequency region could be well matched with the coefficients of drag which was an improvement over the results seen in D4.6 with Newman's approximation.
- The sensitivity analysis of the vertical and horizontal drag coefficients showed the increase in response in the low frequency region for decreasing values, as would be expected. The changes to the drag coefficients, however, were not sufficient for complete replication of all the platform DoFs for the irregular wave test cases and the pink noise test. For the extreme irregular wave case, it was also seen that as the vertical drag coefficients were decrease, the response in the pitch for the wave frequencies was also decrease. This would be due to the fact that the Morison equation creates both damping and forcing.

5.9 Further work

The discussion of this section suggests improved modelling approaches that should be investigated in further work:

- Dependency of the coefficients of drag of the platform and the mooring lines on non-dimensional parameters such as the Reynolds number and the Keulegan–Carpenter number, most likely mean that choosing correct coefficients of drag for the different design load cases becomes a task that needs more investigation. Lemmer [16] has investigated the changing of the drag coefficients for different load cases, and Kvittem, et al. [17] (also within the LIFES50+ project) have looked at changing drag coefficients depending on the depth of the columns of the Olav Olsen platform to try to better capture the second order excitations.
- The analysis presented has focused on the motion response of the platform. The load response is also of interest for the proper design of the system and thus should be the focus of further research. The OC5 project [38] has compared loads of simulations from a floating offshore wind turbine with scaled experimental data but has found a general under-estimation of the extreme and fatigue loads.
- For the extreme irregular wave cases, tuning of the vertical coefficients of drag were found to have trade-offs with respect to the platform response in the low frequency region and in the wave frequency region. Since the Morison equation produces both damping and forcing, the decrease of the Morison element coefficients of drag decreased the response in the frequency wave region and had the opposite effect for the region around the pitch natural frequency of the platform. Further investigation could thus help propose different approaches that would neglect this drawback of the tuning procedure.
- Scaling effects of the platform response and loads will also be of interest for the future development of the platform concept shown here, as the aim of the LIFES50+ project in general is to help the development of the floating platform technologies leading to real life size prototypes.

6 Validation of CFX for the NAUTILUS-DTU10

6.1 Introduction

Advanced numerical models provide a more detailed insight in predominant physical phenomena. One is able to analyse, verify or correct assumptions, limitations and modelling approaches of engineering-level tools by comparison to higher-order methods. The purpose of this study is to evaluate the dynamic behaviour of the NAUTILUS-DTU10 by means of an advanced fluid-structure interaction. It is based on a coupling of a Multibody System (MBS) solver for the structure and a Computational Fluid Dynamics (CFD) solver for the fluid. In particular, the hydrodynamic forces acting on the floating foundation at forced oscillation and free-decay tests in heave are of interest. In this study only, the heave degree-of-freedom is considered for simplification because motion in surge and sway or rotation in roll, pitch and yaw are of minor interest. A lumped mass represents the floating system including rotor-nacelle-assembly and tower because no wind is considered. Mooring lines are not modelled as they are not necessary for the conclusions resulting from this analysis. The CFD results are analysed and resulting hydrodynamic properties, like added mass, damping, natural period etc., are compared to experimental data, which is presented in [37] and [35], as well as results calculated with linear potential flow theory.

A similar study has been performed in [43], but by application of a different CFD solver with the LIFES50+ OO-Star Wind Floater Semi 10MW. The methodologies for analysis of hydrodynamic properties through both numerical and experimental data sets are very common in ocean engineering and ship technology. Thus, relevant literature can be found, for example, in [42], [44] etc.

6.2 Simulation environment and setup

6.2.1 Coupling methodology

A high-fidelity numerical approach is applied to investigate hydrodynamic effects of the NAUTILUS-10 floating foundation. Here, the methodology is briefly introduced. More details are included in [43].

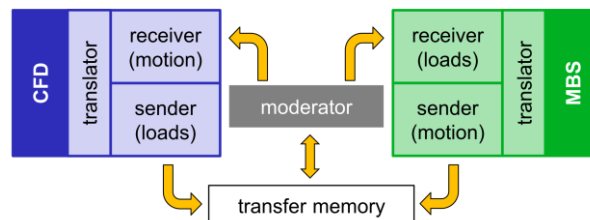


Figure 47: Structure of the MBS-CFD coupling

Hydrodynamics are calculated by means of the commercial CFD code ANSYS CFX. It uses the Finite-Volume Method (FVM) to solve the Reynolds-Averaged Navier-Stokes (RANS) equations on structured and unstructured grids. The free surface is modelled by means of the Volume of Fluid (VOF) method that computes the shape and location of the free surface on the basis of a fractional volume function.

The commercial MBS solver SIMPACK is applied for modelling of the structural properties and is coupled to CFD, see Figure 47. The MBS model is made of bodies, which are connected by joints of various type. Structural properties for the mass, centre of gravity and inertia are defined. External forces like simple spring-damper elements or complex aerodynamic forces on rotor blades may be applied. The resulting MBS topology for forced oscillation and free-decay tests in heave is presented in Figure 48. Here only the heave degree-of-freedom is considered with a rigid foundation not moored to the seabed.

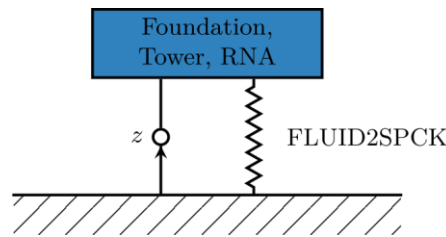


Figure 48: Topology of the MBS model used for forced oscillation and free-decay tests in heave. Hydrodynamic loads from CFD are included by means of the force element FLUID2SPCK.

6.2.2 Numerical wave tank modelling

The geometry of the NAUTILUS-10 is based on the specifications given in [30] and [29]. Model complexity is reduced because the foundation is symmetric in the xz - and yz -plane, see Figure 49: Illustration of the surface mesh of the NAUTILUS-10.. This allows to mesh only 1/4th of the substructure for forced oscillation and free-decay tests in heave and decrease the computational effort by a factor of 4. In order to compare findings with data from the experiment or other simulation tools, the numerical results have to be multiplied by 4 in post-processing. The MBS-CFD model is setup in the numerical domain in model scale with a scaling factor of $\lambda = 36$ according to [37] and a water depth of $d = 130$ m. A hybrid mesh (Figure 49) is used to spatially discretise the platform. The Y-type connection between the cylinder and pontoons at the bottom is meshed by means of tetrahedral grid elements. Prisms are located at surface to resolve the boundary layer and pyramids are included at the interface with the hexahedral mesh that is used for the remaining parts of the Numerical Wave Tank (NWT). For simplification the star-shaped deck and transition piece at the top of the platform is neglected because of missing hydrodynamic influence for forced oscillation and heave free-decay tests in heave. Two mesh variations are investigated, a fine mesh with approximately 890.000 cells in total and a coarse mesh with 407.000 grid elements.

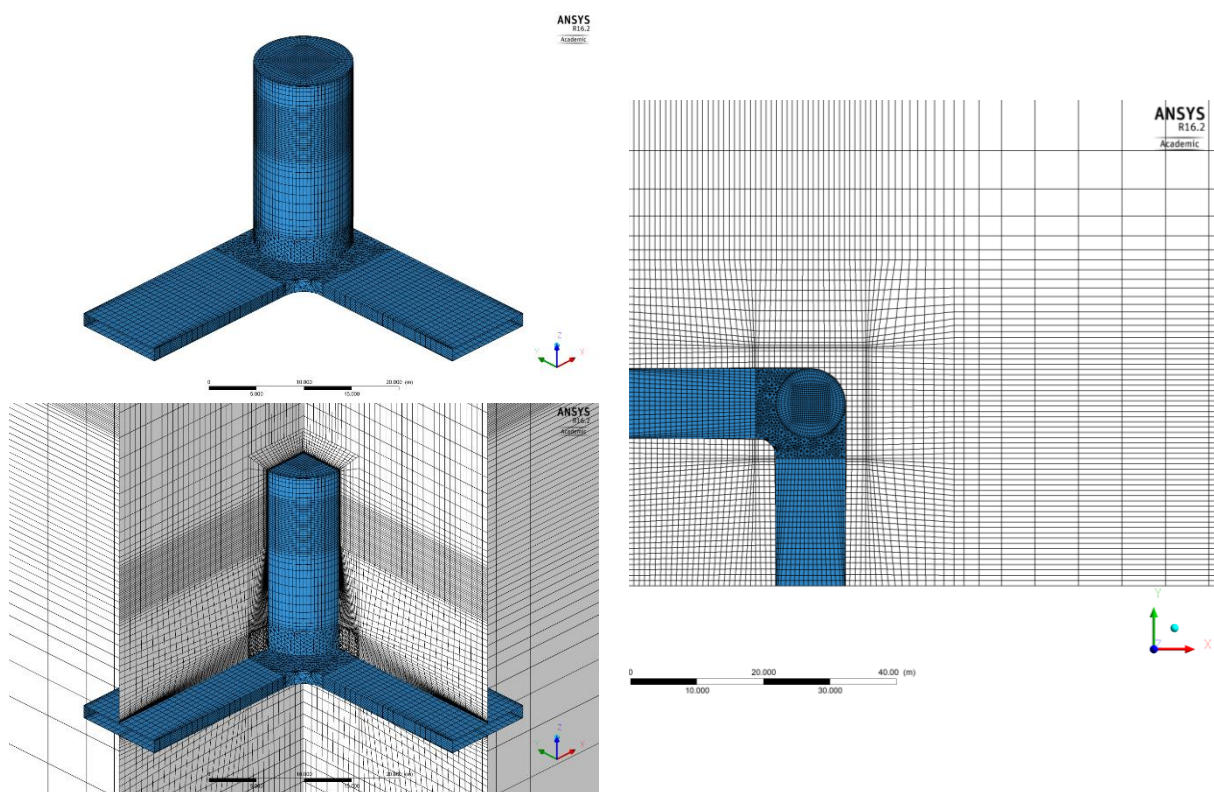


Figure 49: Illustration of the surface mesh of the NAUTILUS-10. The mesh at the right is cut below the foundation.

The NWT has multiple boundary conditions. The seabed is a no slip smooth wall, the side (yz -plane) at y_{max} is a free slip wall and the top is an opening of type entrainment. Symmetries are applied at the yz -plane ($x = 0$ m) and xz -plane ($y = 0$ m). The outlet is an opening with hydrostatic pressure distribution and the floating foundation is modelled by means of no slip smooth wall.

The mesh is deformed in the vicinity of the floating foundation allowing the substructure to move according to the kinematics calculated by the structural solver (MBS). A three-dimensional deformation function $D(x,y,z)$ is defined with $0 \leq D \leq 1$. It is based on a geometric description of an ellipsoid with principal semi-axes a , b and c . For $D = 0$ no mesh deformation is present and for $D = 1$ the mesh is completely translated and rotated. In the transition region the mesh is deformed according to the multiplication of D with the deformations from the MBS solver. The two limits of D are geometrically specified by an outer and inner ellipsoidal volume surface. The latter surrounds the platform and protects it from mesh folding due to stretching and compression. The first needs to fit into the NWT and allow enough room for mesh deformation.

A numerical beach is implemented in the CFD domain to damp radiation waves generated by the moving platform. Two techniques are combined. Firstly, grid elements increase in size towards the outlet, side, seabed and top boundary condition to increase numerical damping. Secondly, momentum sources in x and z are included in the domain starting some distance behind the platform. They are proportional to the velocity squared and provide sufficient damping.

During initialisation the NWT is filled up with water up to the free surface based on the hydrostatic pressure distribution and volume fractions for air and water. The initial velocities are $u = v = w = 0 \text{ m s}^{-1}$. In case of free-decay simulations the platform is deflected in an initial simulation run without fluid solvers to the final initial amplitude. The resulting deformed mesh is loaded into the pre-processor as initial mesh. In order to stabilise the initialisation of the coupled simulation it is beneficial to include a spring-damper element in MBS that fixes the platform for a small number of time steps, e.g. 10.

General CFD solver settings for the coupled simulation are a homogenous multiphase model which results in the same velocity, turbulence, etc. fields for all fluids, an isothermal option at fluid temperature of 25°C, the application of the Shear Stress Transport (SST) turbulence model with automatic wall function and the neglect of surface tension. Water and air are modelled as incompressible fluids. All cases are run with the double-precision solver in parallel and the CFD domain is divided in 32 user specified partitions of direction $[x, y, z] = [1, -1, 1]$, see Figure 50.

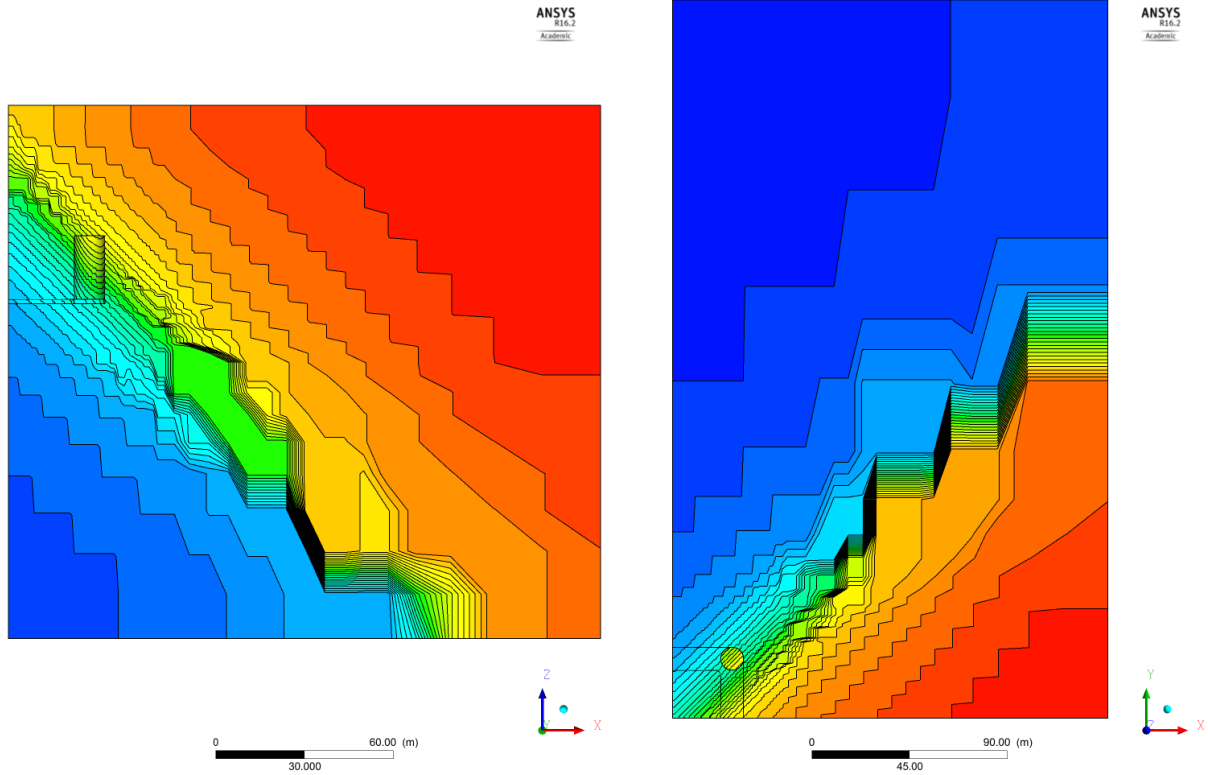


Figure 50: Illustration of the partitioning of the NWT with 32 partitions of direction $[x, y, z] = [1, -1, 1]$.

6.3 Forced oscillation tests

Forced oscillation tests are performed in still water (no wind, no waves) to evaluate the added mass and damping characteristics of the NAUTILUS-10 platform. The heave motion z , velocity \dot{z} and acceleration \ddot{z} are defined by the following equations:

$$z = z_a \sin(\omega t) \quad (6.1)$$

$$\dot{z} = z_a \omega \cos(\omega t) \quad (6.2)$$

$$\ddot{z} = -z_a \omega^2 \sin(\omega t) \quad (6.3)$$

For the determination of hydrodynamic coefficients in heave ($*_{33}$) the floating system is represented by a linear equation of motion:

$$(m + A_{33})\ddot{z} + B_{33}\dot{z} + C_{33}z = F_z \quad (6.4)$$

with body mass m , added mass coefficient A_{33} damping coefficient B_{33} and stiffness coefficient C_{33} . The vertical force F_z acting on substructure is measured over time in CFD:

$$F_z(t) = F_a \sin(\omega t + \varepsilon_{F_z}). \quad (6.5)$$

Equations 6.1 to 6.3 are inserted in 6.4 to solve for A_{33} , B_{33} and C_{33} :

from $\omega t = \pi/2$:

$$A_{33} = \frac{C_{33} - \frac{F_a \cos(\varepsilon_{F_z})}{z_a}}{\omega^2} - m \quad (6.6)$$

from $\omega t = 0$:

$$B_{33} = \frac{\frac{F_a \sin(\varepsilon_{F_z})}{z_a}}{\omega} \quad (6.7)$$

from geometry:

$$C_{33} = \rho g A_w \quad (6.8)$$

with the area of water plane A_w for the NAUTILUS-10 platform using 4 times the cross-sectional area of the cylindrical columns of diameter $d_c = 10.5$ m:

$$A_w = 4 \frac{\pi}{4} d_c^2 = 346.36 \text{ m}^2. \quad (6.9)$$

The in-phase components of the exiting force F_z are associated with inertia and stiffness and are calculated by integration over a whole number n of periods T of the measured signal and multiplication by $\cos(\omega t)$. A similar equation is found for the out-of-phase components which are associated with damping:

in-phase:

$$F_a \cos(\varepsilon_{F_z}) = \frac{2}{nT} \int_0^{nT} F_z(t) \sin(\omega t) dt \quad (6.10)$$

out-of-phase:

$$F_a \sin(\varepsilon_{F_z}) = \frac{2}{nT} \int_0^{nT} F_z(t) \cos(\omega t) dt. \quad (6.11)$$

Equations 6.10 and 6.11 are inserted in equations 6.6 and 6.7 to solve for the coefficients A_{33} and B_{33} . This procedure is also described in [42].

The initial amplitude of the oscillation is $z_0 = 0$ m. A ramp function is used to increase the amplitude of the motion signal from 0 to z_a over one period T to improve numerical stability, for example see graph at top in Figure 51. A total simulation time of 10 periods is applied and the time step size is $\Delta t = T/100$.

At first, the oscillation period is $T = 19.22$ s, which is the natural heave period of the free-floating system according to [35]. Further analysed periods are $T = 5.7$ s and $T = 2.5$ s. With increasing oscillation amplitude viscous effects are becoming more important and, thus, multiple amplitudes are tested with $z_a = 0.1$ m, $z_a = 0.5$ m, and $z_a = 1.0$ m. Additional, the sensitivity of the results on the mesh discretisation is determined by means of a coarse and fine mesh. Moreover, simulations are performed at model and full scale to see if scaling is of importance.

Results for the heave motion z , the resulting vertical force F_z acting on the platform and the Peak Spectral Density (PSD) of the vertical force are presented in Figure 51 to Figure 53. Added mass and damping coefficients A_{33} and B_{33} are calculated based on the method described above and compared in Figure 54 to results from linear potential flow theory (WAMIT). A quantitative summary of the calculated hydrodynamic properties is given in Table 7. Plots and data are given in full scale.

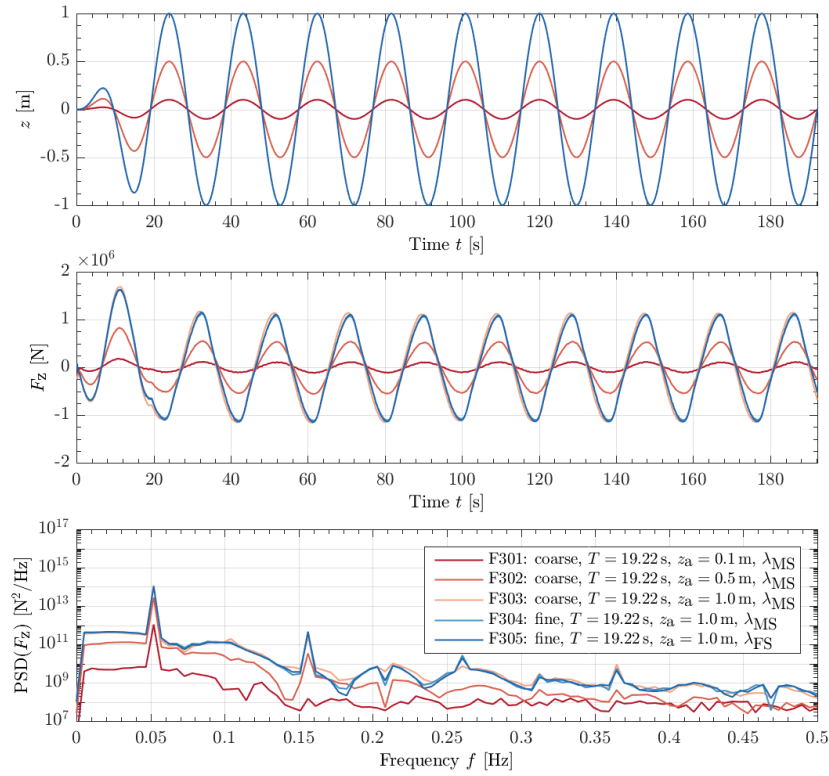


Figure 51: Forced oscillation test in heave with $T = 19.22$ s and $0.1 \text{ m} \leq z_a \leq 1 \text{ m}$. Top: time series of platform heave z . Middle: vertical force component F_z over time. Bottom: PSD of vertical force component over frequency.

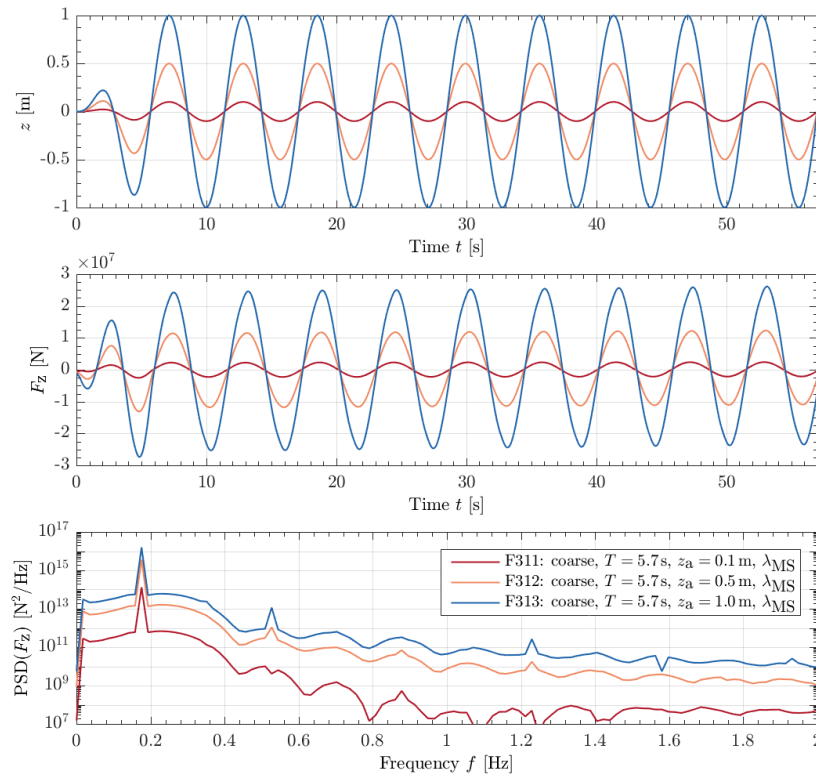


Figure 52: Forced oscillation test in heave with $T = 5.7$ s and $0.1 \text{ m} \leq z_a \leq 1 \text{ m}$. Top: time series of platform heave z . Middle: vertical force component F_z over time. Bottom: PSD of vertical force component over frequency.

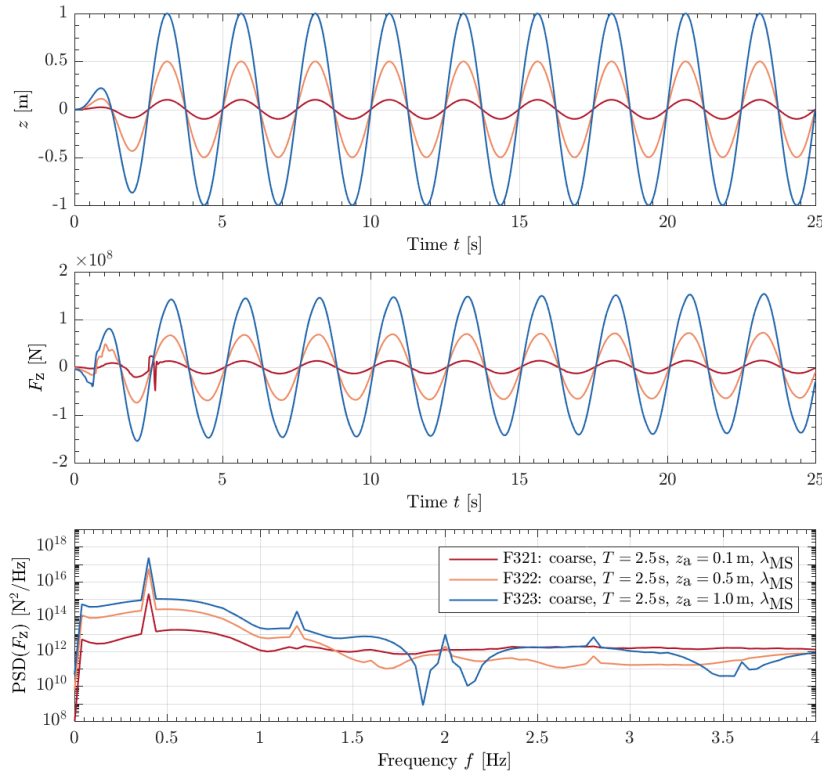


Figure 53: Forced oscillation test in heave with $T = 2.5$ s and $0.1 \text{ m} \leq z_a \leq 1 \text{ m}$. Top: time series of platform heave z . Middle: vertical force component F_z over time. Bottom: PSD of vertical force component over frequency.

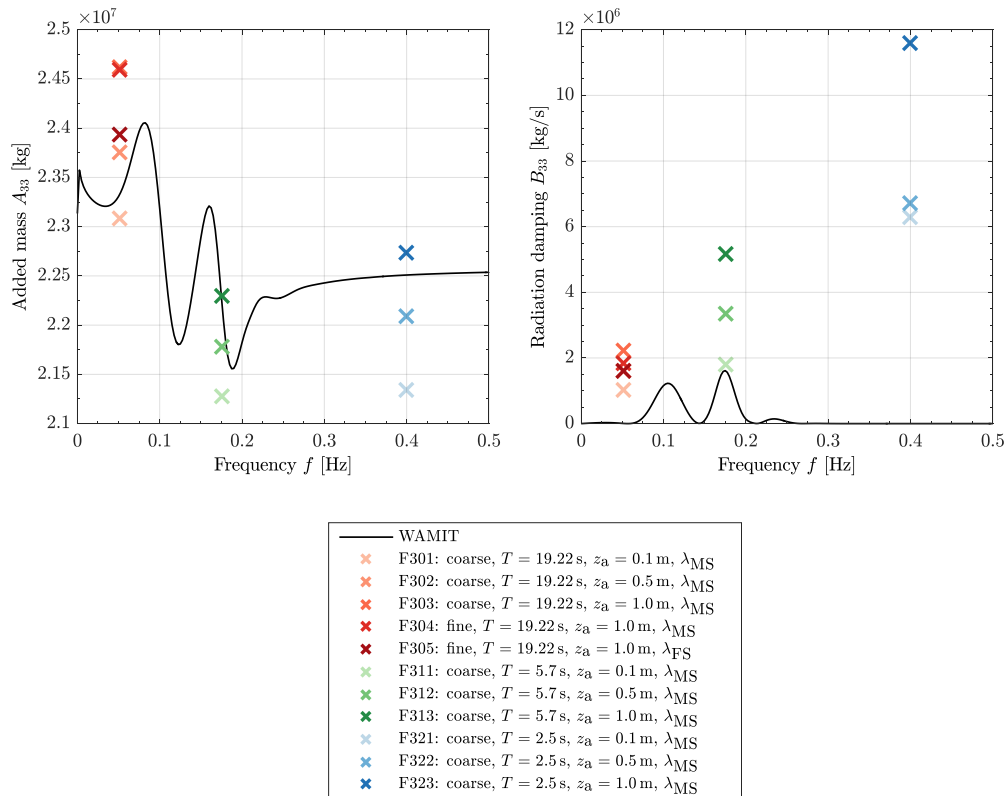


Figure 54: Forced oscillation test in heave with $2.5 \text{ s} \leq T \leq 19.22 \text{ s}$ and $0.1 \text{ m} \leq z_a \leq 1 \text{ m}$. Left: added mass A_{33} over frequency. Right: radiation damping B_{33} over frequency. The reference line is calculated by linear potential theory.

Table 7: Summary of simulation settings and resulting added mass and damping coefficients using MBS-CFD. Data is given in full scale.

ID	Mesh	T [s]	z_a [m]	λ [-]	KC [-]	A_{33} [kg]	$A_{33}/A_{33,exp}$ [-]	B_{33} [kg s ⁻¹]
F301	coarse	19.22	0.1	36	0.06	2.3089E+07	0.9893	1.0198E+06
F302	coarse	19.22	0.5	36	0.30	2.3754E+07	1.0178	1.6016E+06
F303	coarse	19.22	1.0	36	0.60	2.4617E+07	1.0548	2.2406E+06
F304	fine	19.22	1.0	36	0.60	2.4593E+07	1.0538	1.8564E+06
F305	fine	19.22	1.0	1	0.60	2.3942E+07	1.0258	1.6003E+06
F311	coarse	5.7	0.1	36	0.06	2.1275E+07	0.9565	1.8052E+06
F312	coarse	5.7	0.5	36	0.30	2.1787E+07	0.9795	3.3404E+06
F313	coarse	5.7	1.0	36	0.60	2.2291E+07	1.0022	5.1833E+06
F321	coarse	2.5	0.1	36	0.06	2.1339E+07	0.9480	6.3090E+06
F322	coarse	2.5	0.5	36	0.30	2.2094E+07	0.9816	6.7183E+06
F323	coarse	2.5	1.0	36	0.60	2.2739E+07	1.0102	1.1609E+07

Based on the plots and data presented above several conclusions can be drawn. First, the higher the oscillation amplitude, the higher the added mass and damping coefficients derived from MBS-CFD using the same scaling factor and mesh discretisation. This behaviour is expected as viscous effects due to vortex shedding and wall friction increase with the amplitude as well as the additional mass of water that needs to be accelerated during one period.

In general, the solution of the radiation problem in potential flow theory provides good results for the added mass of a floating foundation over a wide range of oscillation frequencies. The A_{33} using MBS-CFD are close to the linear solution for all analysed periods with deviations of 1 to 5%. For simplification the rigid body mass of the foundation was simulated with $m = 1\text{E-}09$ kg in MBS (see also Equation 6.6) because of the prescribed motion leaving an empty hull in the CFD domain.

However, the radiation damping B_{33} in potential flow that introduces damping on the heave motion of the platform due to radiation of water waves is much smaller than the damping calculated by MBS-CFD, especially for smaller oscillation periods like $T = 2.5$ s ($f = 0.4$ Hz). Again, this trend is foreseen as potential flow theory relies on small displacement assumptions and does not account for any viscous effects that are inherently included in the Navier-Stokes equations in CFD. The smaller the oscillation period (the higher the frequency), the higher the flow velocities and viscous effects as drag is getting more relevant. Within engineering-level tools for load calculations of floating offshore wind turbines one usually introduces viscous damping by means of Morison drag distributed on the elements of the platform or additional global matrices for linear and quadratic damping.

Additionally, the grid discretisation is examined. Case F303 uses a coarse mesh and F304 a refined mesh with identical simulation settings. The added mass predicted by the coarse mesh only differs by 0.1% in comparison with the fine mesh. Thus, the fine mesh is not beneficial when only looking at the added mass. But the viscous damping reduces by 17% in F304 with increased number of grid elements in the boundary layer and mesh region in the vicinity of the platform. In general, numerical damping depends on spatial discretisation, among other numerical influences like time stepping scheme as described in section 6.4, and increases for larger grid elements. Thus, the fine mesh is advantageous from the damping point of view. In previous studies for a different platform concept the same numerical behaviour was found for the damping characteristics in relation to the mesh size [45].

Usually, data from experiment and numerical simulation are most commonly compared in full scale by application of Froude scaling. Wave tank model tests are performed in model scale, of course, and the simulations using an engineering-level tool are usually done in full scale. CFD allows to model the flow field around the platform and the resulting hydrodynamic forces either in model or full scale depending on the mesh and input parameters. Besides F305, all MBS-CFD simulations are performed in model scale. By comparison to F304 that applies identical settings, one clearly observes that predicted values of added mass and damping reduce in full scale simulation. Differences for the two cases F304 and F305 occur because of a significant mismatch in Reynolds number, which describes the ratio of inertial forces to viscous forces. For example, considering the height of the pontoons of $z_P = 1.5$ m, see [30], the Reynolds number for F305 at the maximum velocity of the heave oscillation is $Re_{F305} = 5E+05$ but for F304 in model scale it is $Re_{F304} = 3E+03$. Taking into account the dependence of viscous drag on Reynolds number (and KC number) differences in hydrodynamic properties that are derived from CFD simulations applying different scaling factors are inevitable.

In order to demonstrate the flow development at the platform during one heave oscillation, the velocity field (magnitude in full scale) is plotted together with normalised, tangential velocity vectors for F323 (highest amplitude and oscillation frequency). At the beginning, the platform is at $z = 0$ m and moving upwards (Figure 55). It reaches its maximum position in Figure 56 (zero velocity), moves downwards and reaches the initial heave position at $z = 0$ m again (Figure 57) and comes at rest at the minimum heave amplitude in Figure 58. The highest velocities occur at the corners of the pontoons and it can be observed that the platform moves in and out of shed vortices.

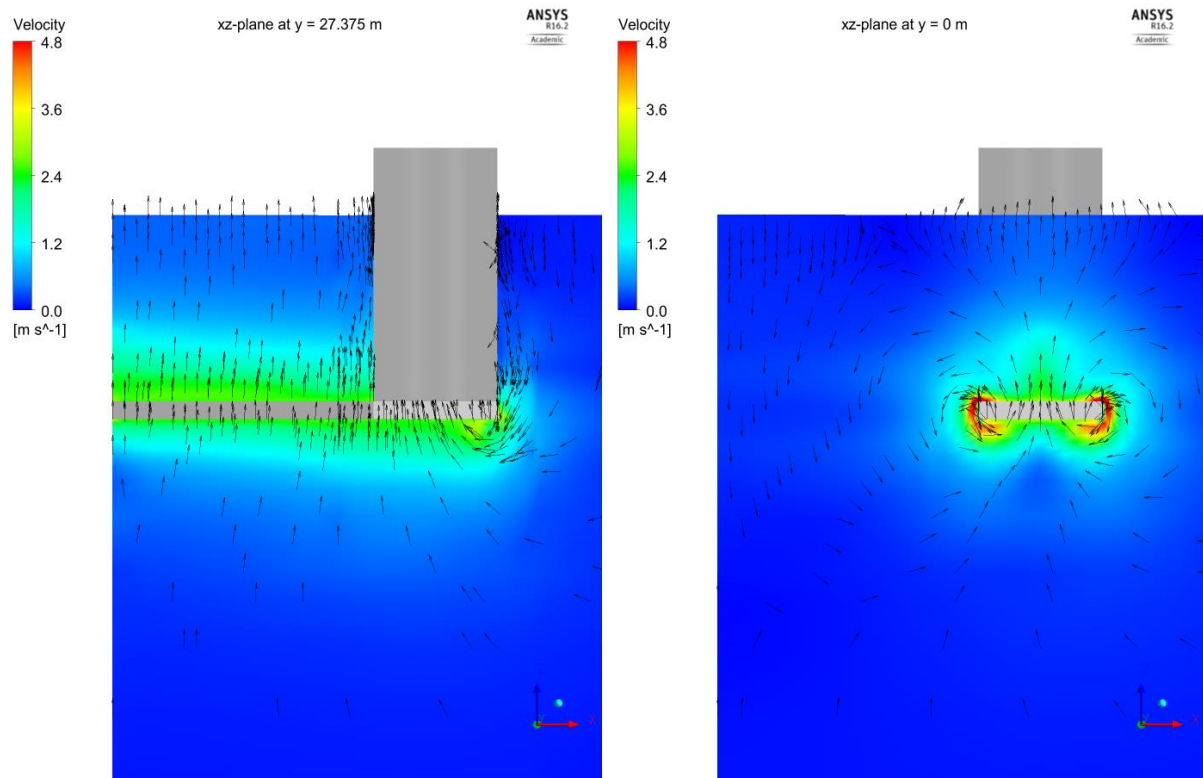


Figure 55: Velocity field at time $t = 22.5$ s for forced heave oscillation test F323 ($T = 2.5$ s, $z_a = 1$ m). The heave amplitude is $z = 0$ m and moving upwards.

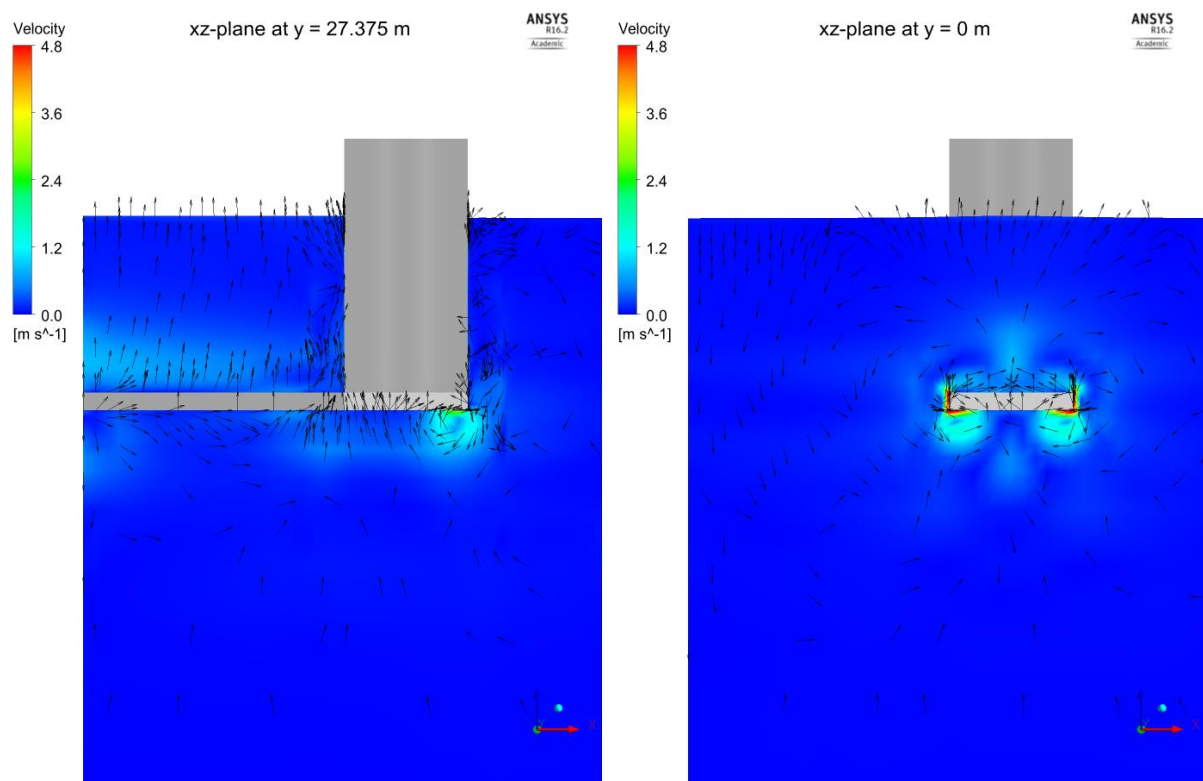


Figure 56: Velocity field at time $t = 23.1$ s for forced heave oscillation test F323 ($T = 2.5$ s, $z_a = 1$ m). The heave amplitude is maximum at $z = 1$ m.

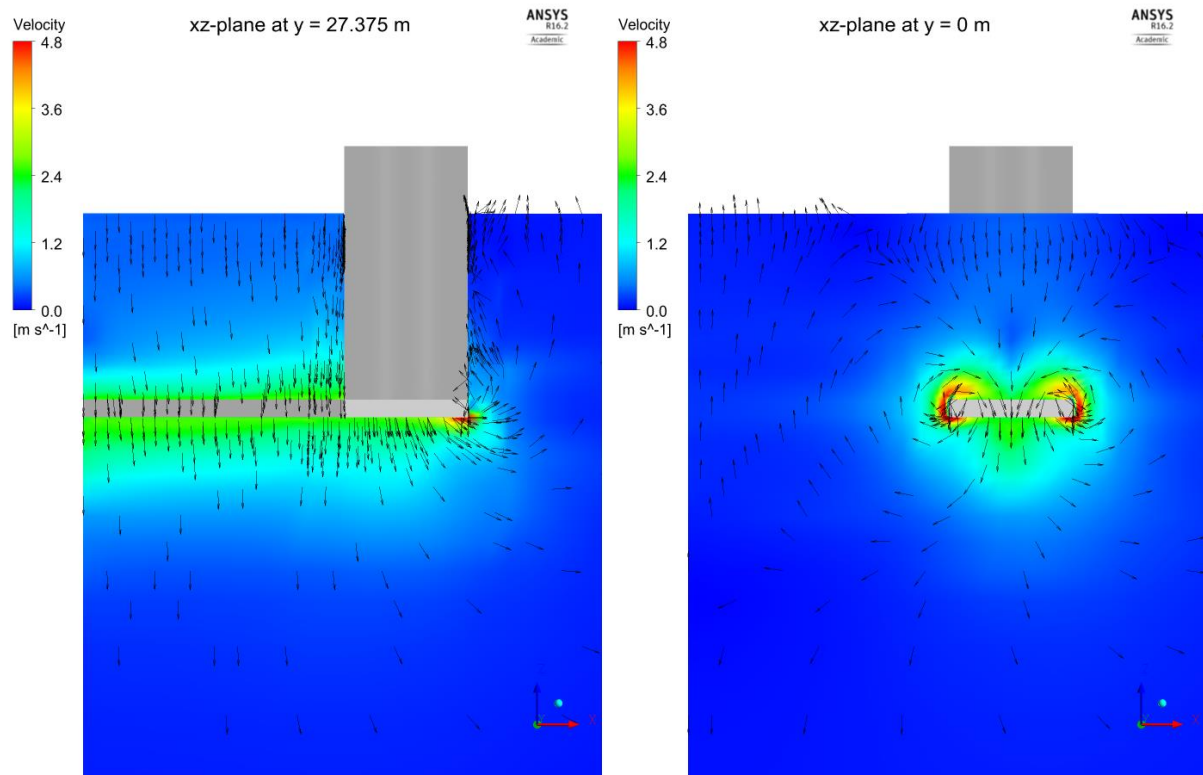


Figure 57: Velocity field at time $t = 23.8$ s for forced heave oscillation test F323 ($T = 2.5$ s, $z_a = 1$ m). The heave amplitude is $z = 0$ m and moving downwards.

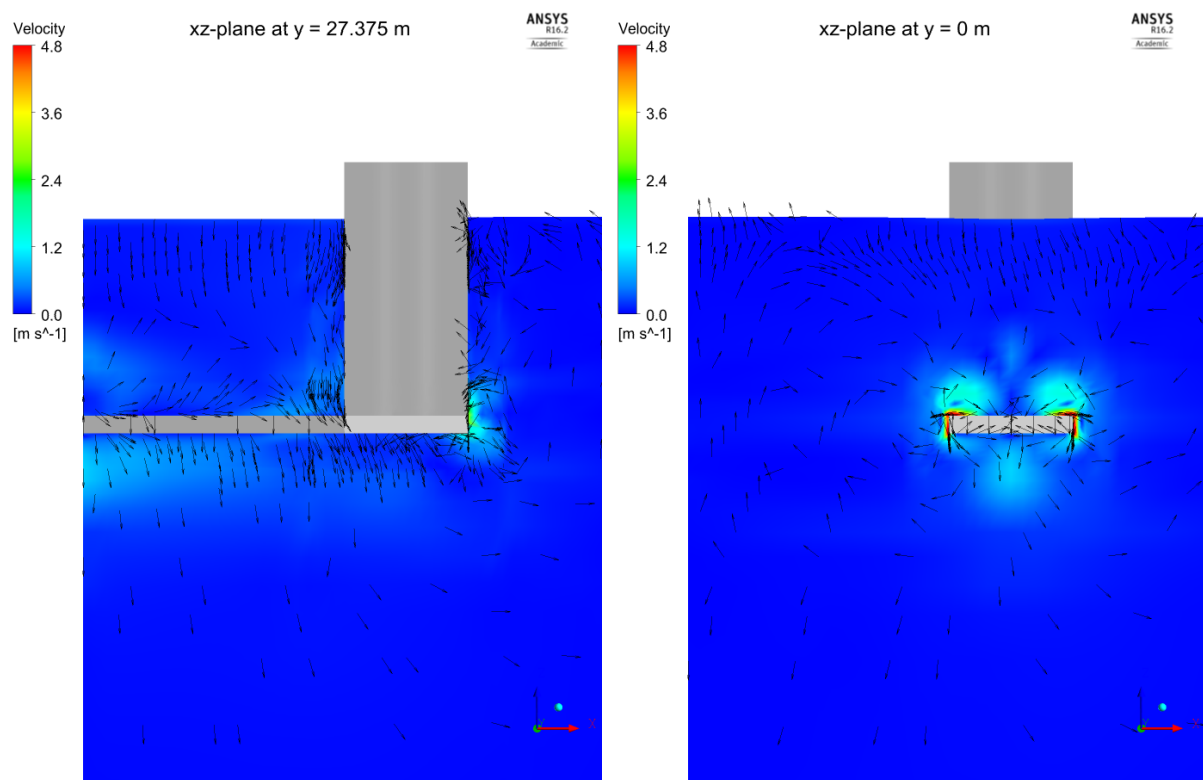


Figure 58: Velocity field at time $t = 24.4$ s for forced heave oscillation test F323 ($T = 2.5$ s, $z_a = 1$ m). The heave amplitude is minimum at $z = -1$ m.

6.4 Free-decay test

In contrast to the forced oscillation tests described in the previous section, this part deals with the analysis of free-decay tests in heave and comparison of numerical results against data from experiment. The model test in the wave basin comprises free-decay tests in free floating and moored condition in calm water. The natural period in heave for both setups is very similar as the mooring lines do not introduce noticeable additional restoring in heave. However, the platform draft increases slightly for the moored case because of a different mass distribution.

The MBS-CFD model uses the same mesh properties and numerical wave tank as for the forced oscillation tests in section 6.3 but without prescription of the platform motion by means of an excitation function in MBS. The initial heave amplitude is derived from experimental data of the moored platform, although no mooring is included in the free-decay simulation. There are three main reasons for this procedure. First, only the heave degree-of-freedom is considered in MBS-CFD for simplification, resulting in zero motion in platform surge and sway and zero rotation in platform roll, pitch and yaw. In comparison to the free-floating condition without mooring, the measurements of the moored platform do not show a significant drift over time after the release, for example in surge, sway and yaw. Thus, the motion of the moored platform in free-decay is more representative for the simulation. Second, multiple repetitions of the free-decay for free floating and moored condition are performed. The best data set in terms of initial inclination and release is found for one free-decay test with mooring. Finally, it is assumed that the influence of mooring lines on the natural period of the heave free-decay is negligible for this type of floating system, which is confirmed by [35]. The moored free-decay data set is used as reference for the comparison to simulation. The MBS-CFD model, especially the platform mass, needs re-calibration to match the equilibrium position and draft of the moored platform.

The simulation procedure is divided in two steps. First, the platform is placed in the undeformed mesh in CFD and an excitation drives the associated platform joint in MBS to the desired initial heave amplitude of $z_0 = -3.34$ m. This step is performed in CFD with enabled mesh deformation only, other equations, for example, for hydrodynamics, etc. are not solved in this preliminary step. In order to compare the results in a reliable way, the same initial heave amplitude needs to be applied in simulation and experiment, other degrees-of-freedom and initial velocities are neglected in this analysis for simplification. Secondly, the actual decay simulation is started applying the initially deformed mesh with full set of equations enabled. Then, the floater decays from the initial heave excitation to equilibrium and the motion and forces, among other things, are tracked during the simulation for post-processing.

Results include the damped natural period T_d that is calculated from the mean of successive maxima and minima found in the z -signal. The non-dimensional damping ratio D is derived by application of the logarithmic decrement, following a procedure described in [42]. Thus, successive pairs of positive and negative maxima are evaluated to calculate damping ratios:

$$D_i = \frac{1}{2\pi} \ln \left[\frac{z_{a,i} - z_{a,i+1}}{z_{a,i+2} - z_{a,i+3}} \right]. \quad (6.12)$$

Double amplitudes are used to avoid spreading due to possible zero-shift. The calculated damping ratios D_i are plotted over the mean heave amplitudes $\bar{z}_{a,i}$:

$$\bar{z}_{a,i} = \left| \frac{z_{a,i} - z_{a,i+1} + z_{a,i+2} - z_{a,i+3}}{4} \right|. \quad (6.13)$$



Afterwards, a regression analysis is applied to characterise the damping. Pure linear damping results in a constant value, represented by a constant line in the plot:

$$D(\overline{z}_a) = D_0. \quad (6.14)$$

But often non-linear damping behaviour appears in floating systems. Thus, linear and quadratic terms are introduced for the approximation of damping:

$$D(\overline{z}_a) = D_1 + D_2 \overline{z}_a. \quad (6.15)$$

In this case, the intersection of the resulting curve with the vertical axis of the plot yields D_1 and the slope of the line represents D_2 .

This procedure is followed to quantify the natural period and damping of experiment and simulation for free-decay test in heave. Results are summarised in Table 8. The damping of the investigated platform in heave is approximated very well with a linear plus quadratic damping function. It is observed in Figure 60 by the good correlation between the plus symbols, representing maxima, and the dashed line, following Equation 6.15. The numerical simulation applying the coupled MBS-CFD environment can be approximated similarly in Figure 61, but it predicts higher damping ratios D_0 to D_1 . A better fit is found for the quadratic term D_2 .

Several influences can be identified for the estimation of damping from free-decay tests using this numerical approach. First, mesh refinement and increased temporal discretisation (smaller time step) will reduce the numerical damping until convergence is reached. Additional, solver parameters such as the applied turbulence model in case of RANS will influence the numerical solution. A special feature occurs with the coupled MBS-CFD methodology as only a first-order backward Euler time stepping scheme can be applied for the fluid solver as described in [46]. Thus, the quality of the numerical solution is reduced in comparison to higher-order schemes and the damping calculated by the solver increases. However, switching to, for example, second-order is not possible as two-time steps would need to be communicated in the implicit coupling scheme which cannot be implemented with the closed commercial MBS and CFD solvers applied in this study.

For the natural periods between experiment and simulation a much better correlation is observed, see Table 8. Simulation D31 slightly overestimates T_d by about 2 percent which may be caused by the increased damping and the mutual influence of damping on the natural period. In general, it is also found by the authors for other floating systems that natural periods are better approximated by the MBS-CFD approach even with a coarse mesh and medium size time step than damping.

Platform heave signals are plotted against each other in Figure 59, again visualising the match in frequency but higher damping for the simulation.

Table 8: Summary of period and damping from heave free-decay test of experiment and MBS-CFD

ID	Method	Mesh	t_{step} [s]	λ [-]	T_d [s]	$T_d / T_{d,exp}$ [-]	D_0 [-]	D_1 [-]	D_2 [-]
D30	Experiment			36	19.1400	1.0000	0.0374	0.0113	0.0942
D31	MBS-CFD	coarse	$T/100$	36	19.4806	1.0178	0.1064	0.0637	0.1096

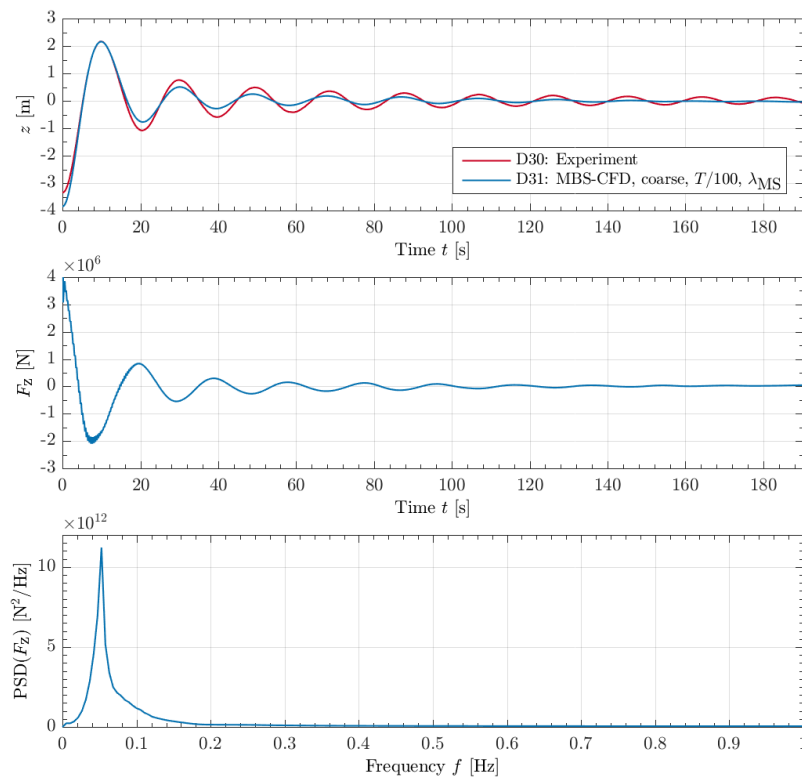


Figure 59: Free-decay test in heave. Top: time series of platform heave z . Middle: vertical force component F_z over time. Bottom: PSD of vertical force component over frequency.

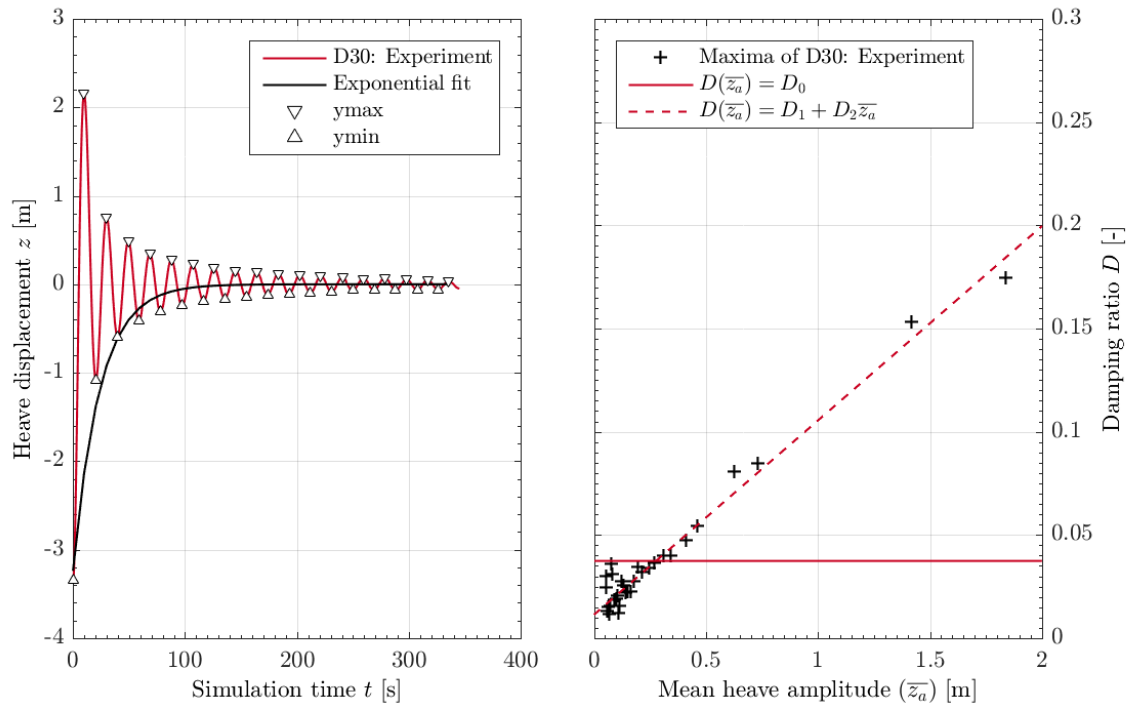


Figure 60: Free-decay test in heave of experimental data. Left: time series in heave z with maxima and exponential fit. Right: damping function D fitted to successive maxima.

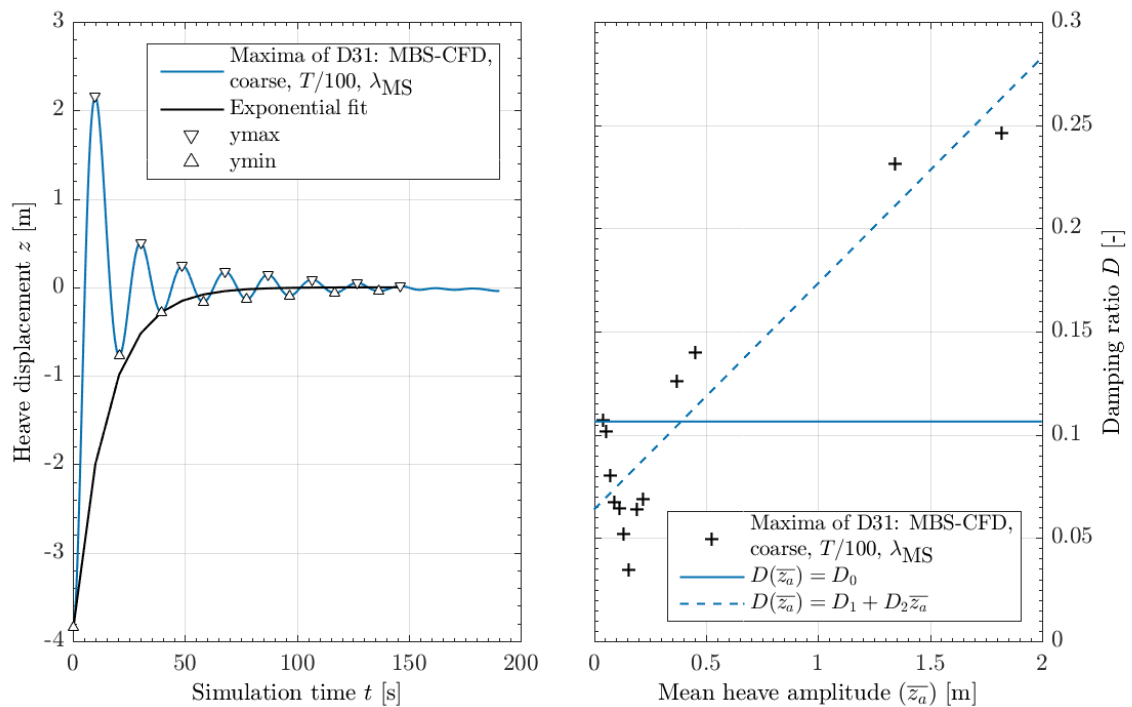


Figure 61: Free-decay test in heave of MBS-CFD data. Left: time series in heave z with maxima and exponential fit. Right: damping function D fitted to successive maxima.

6.5 Conclusions

For the forced oscillation cases, the higher the oscillation amplitude, the higher the added mass and damping coefficients derived from MBS-CFD using the same scaling factor and mesh discretisation. This behaviour is expected as viscous effects due to vortex shedding and wall friction increase with the amplitude as well as the additional mass of water that needs to be accelerated during one period. In general, the solution of the radiation problem in linear potential-flow theory provides good results for the added mass of a floating foundation over a wide range of oscillation frequencies. The heave added mass values using MBS-CFD are close to the linear solution from WAMIT for all analysed periods with deviations of 1 to 5%. However, the radiation damping in heave calculated with potential-flow theory, that arises from radiation of water waves, is much smaller than the heave damping calculated by MBS-CFD, especially for smaller oscillation periods, like $T = 2.5$ s. This trend is foreseen, as potential-flow theory does not account for any viscous effects that are inherently included in the Navier-Stokes equations in CFD. The smaller the oscillation period (the higher the frequency), the higher the flow velocities for constant amplitudes and the more relevant are the viscous effects.

For the heave free decay, mesh refinement and increased temporal discretisation (smaller time step) will reduce the numerical damping until convergence is reached. Additional, solver parameters such as the applied turbulence model in case of RANS will influence the numerical solution. In general, it is also found by the authors for other floating systems that natural periods are better approximated by the MBS-CFD approach even with a coarse mesh and medium size time step than damping.

7 Damping detection by Operational Modal Analysis for the NAUTILUS-DTU10¹

7.1 Introduction

The aim of this study is to numerically reproduce the slow-drift response observed in physical tests, by combining both viscous and inviscid slow-drift forcing with a simplified damping model, suitable for efficient solution of the response. We further investigate the applicability of Operational Modal Analysis (OMA) to extract damping levels from the physical tests in operational sea states of Thys et al. [37] [35].

The extraction of damping from the test data is done through OMA, a set of methods that provide modal properties of a structure — usually natural frequencies, damping ratios and mode shapes — through the analysis of response data in operational conditions. Since the OMA toolset is output-only (meaning that only the measured structural response is needed), it has the potential to become a robust and model-independent way of estimating the modal properties of floating wind turbines. Although OMA comprises several different methods (see Brincker and Ventura [47]), they all work under the same set of assumptions: i) the system can be described with linear equations of motion; ii) the motions are lightly damped; and iii) the excitation loads can be considered as white noise. For this study, the Ibrahim Time Domain (ITD) method was selected [48] [49] [50]. A summary of the OMA method applied for this study can be found in Pegalajar-Jurado and Bredmose [18].

The application of OMA techniques to the rigid-body motion of floating wind turbines was first done by Ruzzo et al. [51]. In their work, which was purely numerical, a numerical model was set up for a spar floating wind turbine, with Morison-based hydrodynamics and linear waves from a JONSWAP spectrum with significant wave height of 2 m and two different peak periods. The damping ratios estimated by applying the Frequency-Domain Decomposition (FDD) method to the model output were compared to the damping ratios specified in the model input. While a general good agreement was reported for the dominant modes in cases where the wave peak frequency was far from the system natural frequencies, a worse comparison was observed for non-dominant modes or in the case where the wave peak frequency was too close to a natural frequency for the resonant modes. Sall [52] applied the Eigensystem Realization Algorithm (ERA) method to physical test data of a scaled semisub floating wind turbine. Although the time series were not always long enough to assure a stable output, the damping ratio was observed to generally increase with the sea state severity. Ruzzo et al. [53] also concluded that the modal damping ratios estimated with OMA are sensitive to the length of the time series analyzed. Nava et al. [54] applied the Covariance-driven Stochastic Subspace Identification (COV-SSI) method to extract heave and pitch modal properties of the NAUTILUS concept from wave-basin test data. The method provided a good estimate of the heave and pitch natural frequencies, but did not provide reliable estimates of the damping ratios.

In this study we separate the different contributions of the Morison drag to allow calibration of the damping without altering the forcing term. Further, considering i) that the quadratic damping contribution in the Morison drag dominates for decay tests in still water, while the linear damping term becomes more important in waves; ii) the wish to keep the model in a linear response format; iii) the wish for easy calibration; and iv) compatibility with OMA results, we approximate viscous effects by a pure forcing term and a linear damping matrix. We explore OMA as a tool to estimate the linear damping matrix for different wave conditions, and also investigate further simplifications of the hydrodynamic added mass and radiation damping matrices. We discuss the damping level as a function of the sea state,

¹ This section is an extract of [18]. For further details please refer to the original paper.

and quantify the success of the simplified linear damping format by comparing to physical test data in terms of time series, PSD and exceedance probability plots of the response in six DoFs.

7.2 Environmental conditions

Table 9 shows the four environmental conditions considered here, all of them with a total duration of 11180 s, equal to 3 h and 1080 s in full scale. In the table, H_s indicates the significant wave height of each sea state, while T corresponds to the period range for the pink-noise spectra (P1 and P2) and to the peak period for the Pierson-Moskowitz spectra (M1 and M2). The case M2 corresponds to the 50-year sea state for the selected site in the Gulf of Maine (see Krieger et al. [55]).

Table 9: Subset of target environmental conditions in [37] selected for this study.

Case	Spectrum	H_s [m]	T [s]
P1	Pink noise	2.0	4.5-18.2
P2	Pink noise	4.0	4.5-18.2
M1	Pierson-Moskowitz	7.7	12.4
M2	Pierson-Moskowitz	10.9	15.0

7.3 The numerical model

The numerical model is an in-house tool specifically developed for the present study. Aerodynamic loads are not included, the rotor is parked and, linked to the focus on low-frequency response, the wind turbine tower and blades are considered rigid. Dynamic mooring loads are included through the MoorDyn model [56] coupled through a dynamic-link library (DLL). The model captures the six rigid-body DoF of a floating wind turbine: surge, sway, heave, roll, pitch and yaw. The level of fidelity is similar to standard state-of-the-art aeroelastic tools, although some simplifications to the standard modelling techniques are introduced, as detailed later in this section.

The starting point for the model are the linearized equations of motion (EoM) of a floating body (Cummins [57], Ogilvie [58]) with forcing terms from waves, mooring reactions and viscous effects,

$$(\mathbf{M} + \mathbf{A}_\infty)\ddot{\boldsymbol{\xi}} + \int_0^t \mathbf{K}(t - \tau)\dot{\boldsymbol{\xi}}(\tau)d\tau + \mathbf{C}_{hst}\dot{\boldsymbol{\xi}} = \mathbf{F}_{exc} + \mathbf{F}_{moor} + \mathbf{F}_{vis}. \quad (7.1)$$

Here $\boldsymbol{\xi} = [\xi_1 \dots \xi_6]^T$ is the vector of displacements in the six DoFs, and dot indicates time derivative. The frequency-domain tool WAMIT [59] was used to solve the radiation-diffraction problem (see Newman [9]) and thus obtain a matrix of hydrostatic stiffness \mathbf{C}_{hst} , as well as frequency-dependent matrices of added mass $\mathbf{A}(\omega)$ and radiation damping $\mathbf{B}_{rad}(\omega)$ and a frequency-dependent vector with the Fourier coefficients of the wave excitation loads, $\hat{\mathbf{F}}_{exc}(\omega)$. In Eqn. (7.1) \mathbf{M} is the mass and inertia matrix, and \mathbf{A}_∞ is the infinite-frequency limit of the added mass matrix. The wave excitation loads in the time domain are given by \mathbf{F}_{exc} , while the mooring reactions and viscous effects are \mathbf{F}_{moor} and \mathbf{F}_{vis} , respectively. The convolution integral in Eqn. (7.1) is due to radiation memory effects, where $\mathbf{K}(t)$ is the radiation-retardation kernel, given by the cosine transform of the radiation damping,

$$\mathbf{K}(t) = \frac{2}{\pi} \int_0^\infty \mathbf{B}_{rad}(\omega) \cos(\omega t) d\omega. \quad (7.2)$$

7.3.1 Simplification of viscous forcing and damping

Viscous effects are commonly computed through the drag term of the Morison equation [60], which gives the drag force dF normal to a cylindrical member section with diameter D and length dl as

$$dF = \frac{1}{2} \rho C_D D |v_f - v_s| (v_f - v_s) dl. \quad (7.3)$$

Here ρ is the water density, C_D is a drag coefficient, and $(v_f - v_s)$ is the local *relative velocity* between the fluid particles and the structure, perpendicular to the member axis. Equation (7.3) may also be written as

$$dF = \frac{1}{2} \rho C_D D \operatorname{sgn}(v_f - v_s) (v_f - v_s)^2 dl \equiv \frac{1}{2} \rho C_D D \operatorname{sgn}(v_f - v_s) (v_f^2 + v_s^2 - 2v_f v_s) dl, \quad (7.4)$$

which shows that viscous effects are the sum of a pure forcing term, a quadratic damping term and a linear damping term. In Eqn. (7.1), the vector \mathbf{F}_{vis} corresponds to

$$\mathbf{F}_{vis} = \int_l \frac{1}{2} \rho C_D D |v_f - v_s| (v_f - v_s) dl. \quad (7.5)$$

The structural velocity v_s normal to the member axis at a location \vec{r} is obtained by multiplying the local velocity by a normal unit vector \vec{n} ,

$$v_s = \vec{n} \cdot [\xi_1 \xi_2 \xi_3]^T - \vec{r} \times [\xi_4 \xi_5 \xi_6]^T. \quad (7.6)$$

Under the assumption that $\operatorname{sgn}(v_f - v_s) = \operatorname{sgn}(v_f)$ and by neglectation of the quadratic damping term, we approximate the drag loads as

$$\mathbf{F}_{vis} \approx \int_l \frac{1}{2} \rho C_D D |v_f| v_f dl - \int_l \rho C_D D |v_f| v_s dl \approx \mathbf{F}_{vis'} - \mathbf{B}_{vl} \dot{\xi}, \quad (7.7)$$

where $\mathbf{F}_{vis'}$ is the integral of the drag forces considering the local *absolute velocity* of the fluid particles (or the pure forcing term), and the linear damping term is represented by a constant matrix applied to the bulk motion of the floater. The main motivation for this simplification is that the overall linear damping will be calibrated later anyway. While the original relative Morison formulation will capture local phenomena better, the simpler damping format of Eqn. (7.7) is chosen due to ease of calibration and computational efficiency. The quadratic damping term, which is not considered here, dominates for decay tests in still water but it is expected to be less important than the linear term in wave conditions. Given the factor $|v_f|$ in the second term of Eqn. (7.7), \mathbf{B}_{vl} is expected to increase in magnitude for increased wave velocity levels, for a successful approximation of Eqn. (7.5) by Eqn. (7.7). With the

simplifications mentioned so far, a connection to a linear version of the EoM (solvable in the frequency domain) is also possible, although this step has not been taken in this study.

7.3.2 Simplification of added mass and radiation damping

Motivated also by the fact that OMA captures *global* linear damping ratios, the effect of the frequency-dependent radiation damping (represented by the convolution integral in Eqn. (7.1)) is also lumped into a constant linear global damping matrix \mathbf{B} , thus losing the frequency dependence. This step is justified by observing that generally all responses but heave are dominated or heavily influenced by resonance at the natural frequencies. For example, Figure 62 shows the pitch-pitch element of the frequency-dependent radiation damping matrix, as well as the pitch-pitch element of the linear damping matrix after calibration for the sea state P1. It can be seen that the radiation damping alone is not able to counteract the resonance, given that its value at the natural frequency (black dashed line) is very small compared to the amount of damping needed to obtain a reasonable resonant response (red solid line). On the other hand, including both sources of damping leads to overdamping in the wave frequency range (green dashed lines), where the radiation damping is significantly higher than the constant linear damping. It is also worth noting that avoiding the convolution integral in the model significantly reduces the computational time.

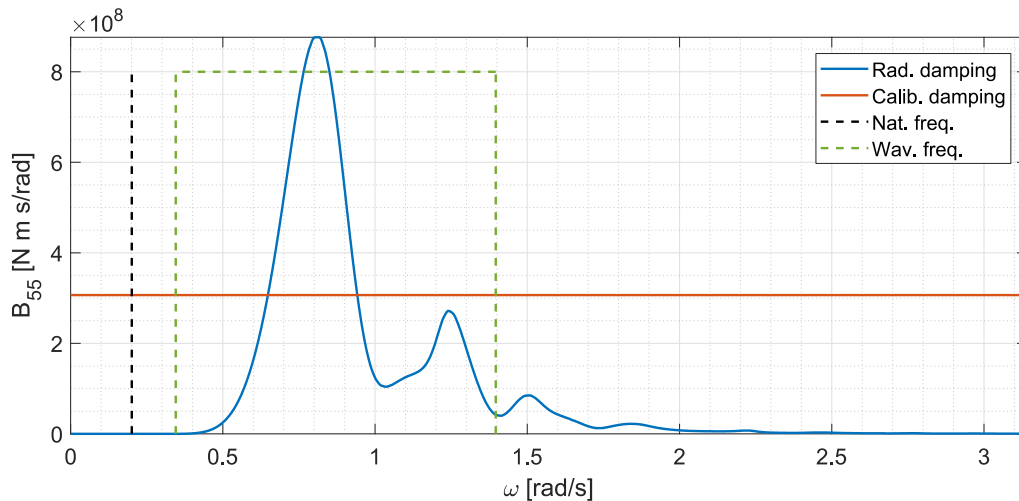


Figure 62: Radiation damping and the linear damping needed in the pitch degree of freedom for sea state P1. The black dashed line indicates the pitch natural frequency of the moored system, while the green dashed lines indicate the wave frequency range.

Since the convolution integral also contributes to the added mass, the effect of its simplification on the response-amplitude operators (RAOs) was investigated. As an example, the surge RAO for the moored floating wind turbine is shown in Figure 63. It was computed from the first-order wave excitation loads and using a linearized mooring matrix. Three different RAOs are compared in the figure: the RAO using frequency-dependent added mass $\mathbf{A}(\omega)$ and radiation damping $\mathbf{B}_{rad}(\omega)$ from the WAMIT solution (blue); the RAO using the zero-frequency added mass \mathbf{A}_0 and the constant damping matrix \mathbf{B} calibrated for sea state P1 (red); and the RAO using the infinite-frequency added mass \mathbf{A}_∞ and the constant damping matrix \mathbf{B} calibrated for sea state P1 (green). The left panel is centered at the surge natural frequency, and shows that the radiation damping alone would lead to an unrealistic surge response. The right panel focuses on the wave frequency range for the same sea state. Here we see that, while neglecting the convolution integral leads to errors in the RAO, the zero-frequency limit is a better alternative than the infinite-frequency limit in such case.

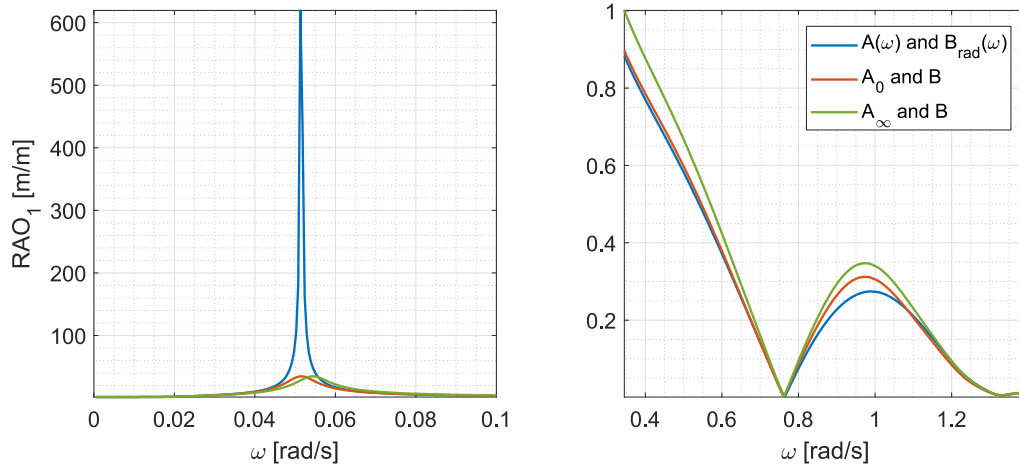


Figure 63: Comparison of surge response-amplitude operator using frequency-dependent and constant radiation properties. The left panel is centred at the surge natural frequency, while the right panel shows the wave frequency range for sea states P1 and P2.

7.3.3 The final equation of motion

The modelling choices presented above mean that *all* the damping effects on the floater are lumped into the matrix \mathbf{B} , with the only exception being the viscous drag on the mooring system (see Section 7.3.8). The EoM implemented in the model is therefore

$$(\mathbf{M} + \mathbf{A}_0)\ddot{\xi} + \mathbf{B}\dot{\xi} + \mathbf{C}_{hst}\xi = \mathbf{F}_{exc} + \mathbf{F}_{moor} + \mathbf{F}_{vis}. \quad (7.8)$$

The different elements involved in Eqn. (7.8) are discussed in the following subsections.

7.3.4 Linear damping matrix

The linear damping matrix is built from damping ratios extracted from the test data with Operational Modal Analysis. For the present case, the input data array contained time series of measured surge, sway, heave, roll, pitch and yaw, hence. In order to isolate the resonant responses, each of the six raw signals was band-pass filtered with a bandwidth of 0.03 Hz centered around the natural frequency of the given DoF. Furthermore, the correlation matrix was truncated at $t = 500$ s, given that the correlation functions contained only noise for $t > 500$ s.

Since OMA provides *modal* damping ratios, the linear damping matrix \mathbf{B} is also built in the modal space. We choose to base the numerical modal damping matrix on the modal vectors of the numerical model, combined with the damping ratios from the OMA analysis. The numerical model's system matrix \mathbf{D}_{num} is built as

$$\mathbf{D}_{num} = (\mathbf{M} + \mathbf{A}_0)^{-1}(\mathbf{C}_{hst} + \mathbf{C}_{moor}), \quad (7.9)$$

where \mathbf{M} is the mass matrix, \mathbf{A}_0 is the zero-frequency limit of the added mass matrix, \mathbf{C}_{hst} is the hydrostatic restoring matrix and \mathbf{C}_{moor} is the mooring restoring matrix, resulting from the linearization of the mooring system around the equilibrium position in still water. The diagonalization of \mathbf{D}_{num} provides a set of eigenvectors contained in the columns of Ψ_{num} , which is used to diagonalize the model's mass and stiffness matrices,

$$[m_n] = \Psi_{num}^T (\mathbf{M} + \mathbf{A}_0) \Psi_{num}, \quad (7.10)$$

$$[k_n] = \Psi_{num}^T (\mathbf{C}_{hst} + \mathbf{C}_{moor}) \Psi_{num}. \quad (7.11)$$

For each mode, the modal damping coefficient is thus computed as $b_n = 2\zeta_n \sqrt{m_n k_n}$. Finally, the diagonal matrix of modal damping coefficients $[b_n]$ is transformed back to the physical space by virtue of

$$\mathbf{B} = (\Psi_{num}^T)^{-1} [b_n] \Psi_{num}^{-1}. \quad (7.12)$$

Given the findings of Ruzzo et al. [51], it is part of the present study to investigate how well the damping detected with OMA can lead to a good match between the measurements and the model output. For this reason, a calibrated modal damping ratio is also found for each sea state. The six modal damping ratios ζ_n are calibrated until the standard deviation σ of the computed response in each DoF is as close as possible to the standard deviation of the measured response. In both signals the first 1080 s are discarded in the computation of σ . By working with modal damping coefficients, the damping in each DoF is independently calibrated with only one parameter.

7.3.5 Wave excitation loads

The vector of wave excitation loads contains first- and second-order components,

$$\mathbf{F}_{exc} = \mathbf{F}_{exc}^{(1)} + \mathbf{F}_{exc}^{(2)}. \quad (7.13)$$

According to Pinkster [6], the second-order loads are due to five components, namely:

6. the first-order relative wave elevation;
7. the quadratic interaction of the first-order velocity potential with itself;
8. the second-order velocity potential;
9. the interaction of the first-order potential and the first-order motion;
10. and the interaction of the first-order rotations with the first-order body accelerations.

As mentioned in Simos et al. [7], the first-order motion is sensitive to the amount of damping in the system. Since the viscous damping is expected to change with the sea state, the second-order analysis would have to be carried out for each sea state due to the dependence of the second-order solution on the first-order motion. Therefore, for the present work the contributions of the first-order motion to the second-order loads (items 4 and 5 in the list above) are not considered. This also allows a more general solution of the second-order problem, which is independent on the motion and can thus be re-used for different environmental conditions, including cases with wind forcing. This simplification is expected to have small effect for mild sea states, but it may lead to an underprediction of the second-order loads for severe sea states. On the other hand, computation of the Quadratic Transfer Functions (QTFs) including the first-order solution with insufficient damping may lead to overestimation of the second-order loads [8]. Further details on the theory behind first- and second-order radiation diffraction theory can be found in Newman [9], Pinkster [6] and Lee [10].

For the present model, the time-domain implementation of the second-order hydrodynamic loads has been verified against FAST v8 [11]. Full difference-frequency QTF matrices were computed in WAMIT

for the six DoF, considering 50 angular frequencies in the range 0.0628-3.1416 rad/s, which corresponds to periods in the range 2-100 s. The sum-frequency loads were not included as they are expected to have negligible effects on the semisubmersible considered here (see [12], [8]). Taking advantage of symmetry, one quarter of the floater was discretized with 3719 panels (see Figure 64, right).

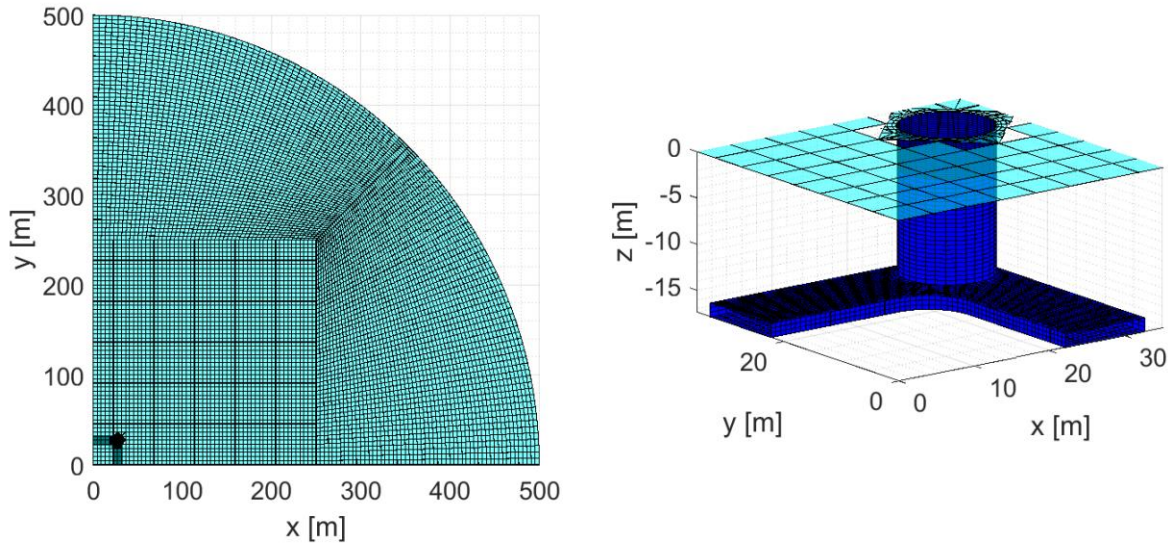


Figure 64: Panel discretization of the free surface (left) and the floater (right) for the WAMIT analysis.

The discretization of the free surface required a convergence study, where two parameters were varied: the radius of the partition inside which the integration of the quadratic forcing over the free surface is done numerically, RINNER; and the size of the free-surface panels relative to the body panel size at the free surface, SCALE. Results for RINNER values of 100, 300, 500 and 1000 m and SCALE values of 1, 2, 4 and 8 were compared for angular frequencies corresponding to 1.00, 1.05, 1.10 and 1.35 rad/s [13]. The convergence study suggested that, although the effect of the free surface was small, a discretization with RINNER=500 and SCALE=4 was appropriate (see Figure 64, left). The agreement between the QTF results obtained with direct and indirect methods was also interpreted as a sign of numerical convergence with respect to panel resolution [14].

7.3.6 Viscous drag forcing

To compute the viscous drag forcing term \mathbf{F}_{vis} , the floater (see Figure 33) was divided into four vertical columns and four rectangular horizontal members (square pontoon), as shown in Figure 65. The geometry simplification adopted preserves the total area of the square pontoon, but leads to 2.76% error in the moment of area. The error in the computation of viscous drag forcing is expected to be in the same order of magnitude, and negligible in the overall dynamics due to the hydrodynamic loads being inertia-dominated.

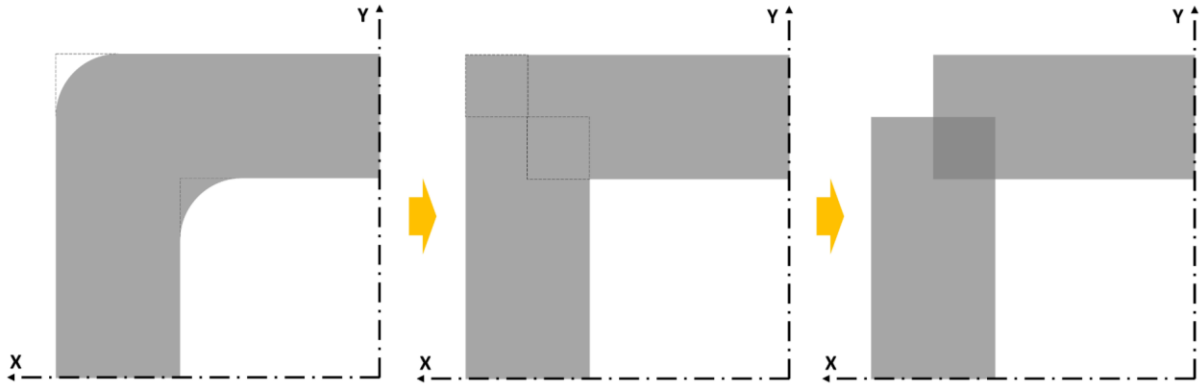


Figure 65: Simplification of the square pontoon geometry (bottom view) for calculating viscous drag loads on the NAUTILUS-10 floater.

Each of the eight members were discretized, and for each element the pure viscous drag forcing normal to the member axis was computed as $dF = \frac{1}{2} \rho C_D D |v_f| v_f dl$, where the wave particle velocity v_f at each location was computed internally in the model based on Airy wave kinematics [61] up to $z = 0$. The drag coefficients were estimated as $C_D = 0.68$ for the columns based on lab-scale Reynolds and Keulegan-Carpenter numbers at the still water level, and as $C_D = 2.05$ for the rectangular members due to flow separation in the sharp corners.

7.3.7 Mass, gravity and hydrostatics

The symmetric matrix of mass and inertia, referred to the entire structure, is built as

$$\mathbf{M} = \begin{bmatrix} m & 0 & 0 & 0 & mz^{CM} & -my^{CM} \\ & m & 0 & -mz^{CM} & 0 & mx^{CM} \\ & & m & my^{CM} & -mx^{CM} & 0 \\ & & & I_x^O & -I_{xy}^O & -I_{zx}^O \\ & & & & I_y^O & -I_{yz}^O \\ & & & & & I_z^O \end{bmatrix}, \quad (7.16)$$

where m is the total mass, I_x^O , I_y^O and I_z^O are the mass moments of inertia referred to the flotation point O , (x^{CM}, y^{CM}, z^{CM}) is the position of the centre of mass (CM) and I_{xy}^O , I_{yz}^O and I_{zx}^O are the products of inertia. Note that due to symmetry in this case, $x^{CM} = y^{CM} = 0$ and $I_{xy}^O = I_{yz}^O = I_{zx}^O = 0$. All the non-zero values are taken as reported in [37]. The hydrostatic restoring matrix \mathbf{C}_{hst} including contributions from waterplane and centre of buoyancy was imported from WAMIT, and the contribution from gravity was added internally in the model.

7.3.8 Mooring loads

The mooring loads \mathbf{F}_{moor} were computed externally by MoorDyn at each time step and coupled to the model via a DLL. MoorDyn [56] is a dynamic lumped-mass mooring model that includes dynamic effects such as mass inertia, buoyancy and Morison-based hydrodynamic forces resulting from the motion of the lines in calm water (i.e. the mooring lines do not see the wave kinematics). As mentioned before, even though the aim of this study is to have all damping effects lumped into the linear damping matrix, the drag forces on the mooring lines were enabled to avoid unphysical mooring line vibrations. The drag coefficient was estimated as $C_D = 2$ based on the lab-scale Reynolds and Keulegan-Carpenter numbers. The damping effect of mooring drag loads on the floater motion was quantified by carrying out decay simulations in the model with all the linear damping coefficients set to zero. Table 10 shows

the linearized damping ratios estimated from these decay simulations, compared to the linearized damping ratios extracted from decay tests [37]. As observed in the table, the effect of mooring viscous drag on the floater motion is smaller for pitch and heave, while it is significant for surge and yaw. This will be taken into account when discussing the damping levels in the different operational sea states.

Table 10: Damping effects on the floater motion resulting from drag loads on the mooring lines, compared to the linearized damping ratios in the decay tests [37].

	Surge	Heave	Pitch	Yaw
$\zeta_{moor}[\%]$	1.7	0.4	0.9	2.2
$\zeta_{test}[\%]$	4.0	3.9	10.6	2.9

7.4 Results and discussion

We now compare to the test data the numerical results with calibrated damping ratios for the four sea states shown in Table 9. To avoid a minor offset in the heave response, the displaced volume in the model was adjusted to 98.77% of the value reported in [37]. Given that the motion signals were not zeroed between tests, the initial value in each time series was subtracted for comparison to the numerical output. For each environmental condition, the response in each of the six DoFs is shown in terms of a representative portion of the time series (left column), a PSD plot (central column) and an exceedance probability plot (right column). For both the PSD and the exceedance probability analysis the first 1080 s were discarded to avoid initial transient effects. The PSD signals were smoothened by applying a moving-average filter with 20 points. The red vertical dashed lines in the PSD plots indicate the natural frequency in each DoF reported in [37]. The exceedance probability plots were obtained from peaks extracted from the time series, which were sorted and assigned a probability based on their position in the sorted list. To better compare the dynamics of the system, the mean was removed before carrying out the probability analysis, and the mean responses are included in the plots of time series and are compared later in this section. The red horizontal dashed lines in the probability plots correspond to the 95% percentile. Each response plot is followed by a table comparing test and model response in each DoF in terms of the mean $\bar{\xi}$, standard deviation σ and value at the 95% percentile $\xi^{95\%}$. The relative error in σ and $\xi^{95\%}$ is also shown.

7.4.1 Response to pink-noise waves

The response to the pink-noise sea state P1 is shown in Figure 66 and Table 11. All the DoFs but heave are dominated by resonance at the natural frequency, while the linear wave loads dominate the heave response and are also visible in roll and pitch. The model predicts well the motion in surge, sway and heave, with overpredictions up to 7% in the 95% percentile. The rotational motions show underpredictions up to 10%, with the yaw motion also showing error in the standard deviation. It was observed that the yaw motion was underpredicted for all sea states, and a match of σ_6 was never possible even if the modal damping ratio ζ_6 was set to zero. However, $\zeta_6 = 0$ does not mean that the yaw motion is completely undamped, since the drag on the mooring lines introduces significant damping in yaw, surge and sway (see Table 10). Thus, the yaw underprediction is believed to arise from missing wave excitation.

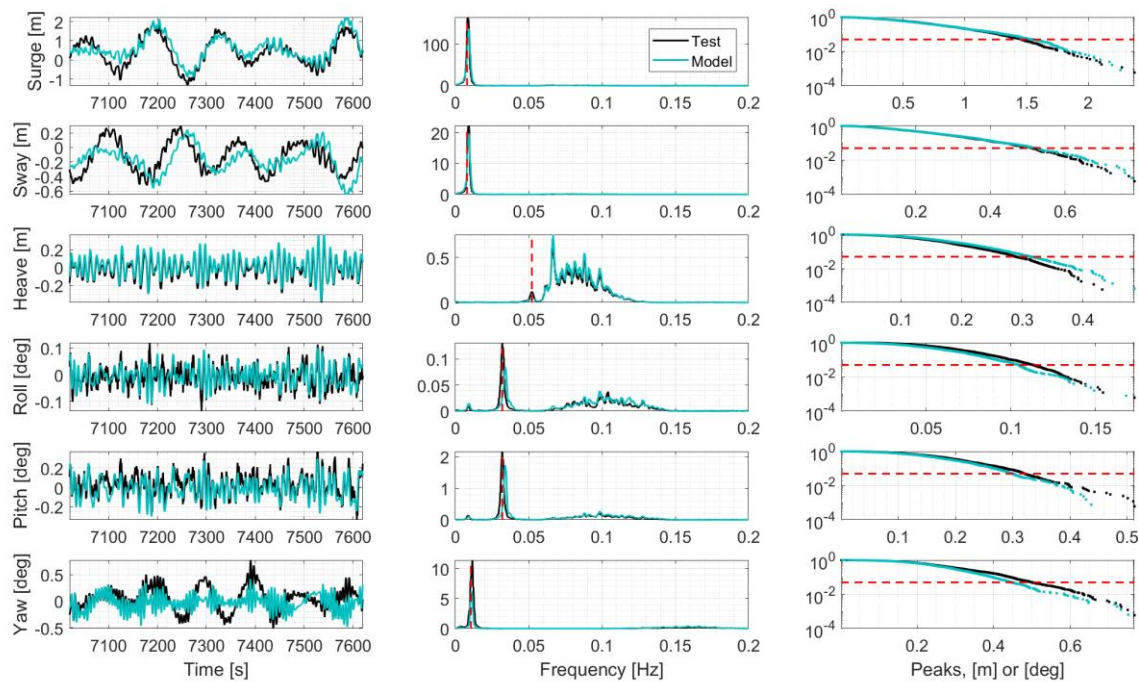


Figure 66: Time, frequency and exceedance probability plots for case P1.

Table 11: Results statistics for case P1.

	$\bar{\xi}_{test}$	$\bar{\xi}_{model}$	σ_{test}	σ_{model}	err. [%]	$\xi_{test}^{95\%}$	$\xi_{model}^{95\%}$	err. [%]
Surge [m]	0.40	0.54	0.69	0.69	0.0	1.46	1.55	+6.2
Sway [m]	-0.13	-0.16	0.24	0.24	0.0	0.51	0.53	+3.9
Heave [m]	-0.02	0.01	0.12	0.12	0.0	0.29	0.31	+6.9
Roll [deg]	-0.01	0.00	0.04	0.04	0.0	0.11	0.10	-9.1
Pitch [deg]	0.03	-0.01	0.12	0.12	0.0	0.32	0.30	-6.3
Yaw [deg]	0.04	-0.03	0.21	0.17	-19.0	0.50	0.45	-10.0

Figure 67 and Table 12 show the response to the pink-noise sea state P2. The observations reported for P1 also apply to P2, although a better match of the 95% percentile is obtained in this case, with errors up to 5% in all DoFs but yaw. The yaw motion, on the other hand, is again significantly underpredicted with errors larger than those reported for P1.

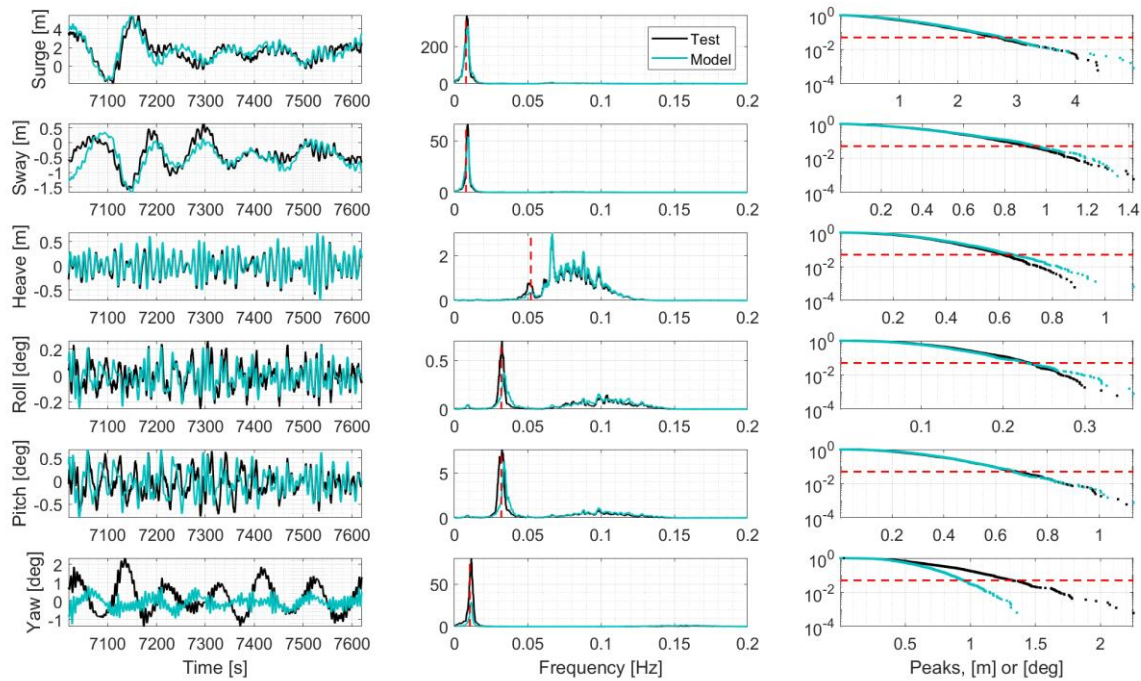


Figure 67: Time, frequency and exceedance probability plots for case P2.

Table 12: Results statistics for case P2.

	$\bar{\xi}_{test}$	$\bar{\xi}_{model}$	σ_{test}	σ_{model}	err. [%]	$\xi_{test}^{95\%}$	$\xi_{model}^{95\%}$	err. [%]
Surge [m]	1.47	1.61	1.24	1.24	0.0	2.69	2.76	+2.6
Sway [m]	-0.35	-0.49	0.45	0.45	0.0	0.91	0.95	+4.4
Heave [m]	-0.01	0.02	0.25	0.25	0.0	0.62	0.65	+4.8
Roll [deg]	0.00	-0.01	0.09	0.09	0.0	0.23	0.23	0.0
Pitch [deg]	-0.04	-0.04	0.26	0.26	0.0	0.68	0.67	-1.5
Yaw [deg]	0.08	-0.09	0.57	0.38	-33.3	1.32	0.95	-28.0

7.4.2 Response to Pierson-Moskowitz waves

The response to the Pierson-Moskowitz sea state M1 is shown in Figure 68 and Table 13. Surge, sway and yaw are still dominated by resonance, while heave is dominated by linear wave loads and roll and pitch show similar response at the wave range and at the natural frequency. Although a good match is observed in the exceedance probability plots, the spectral comparison seems less good than for the pink-noise cases discussed above, especially for roll and pitch. This is a consequence of the calibration criterion, since the standard deviation σ relates to the response spectrum through $\sigma_{\xi,j}^2 = \int_0^\infty S_{\xi,j}(\omega) d\omega$. Hence, matching σ ensures that the area under the response spectrum between test and model is the same, although local differences may exist. The 95% percentile values deviate up to 6%, with the yaw motion showing a worse prediction than for P1 and P2. The standard deviation of the surge response could not be matched in this case, even if $\zeta_1 = 0$. Still, a good match is observed in the exceedance probability plot and the 95% percentile. As discussed for the yaw motion earlier, the drag on the mooring lines introduces significant damping in the horizontal DoFs, thus this level of damping combined with missing wave excitation forces leads to a mismatch in σ_1 .

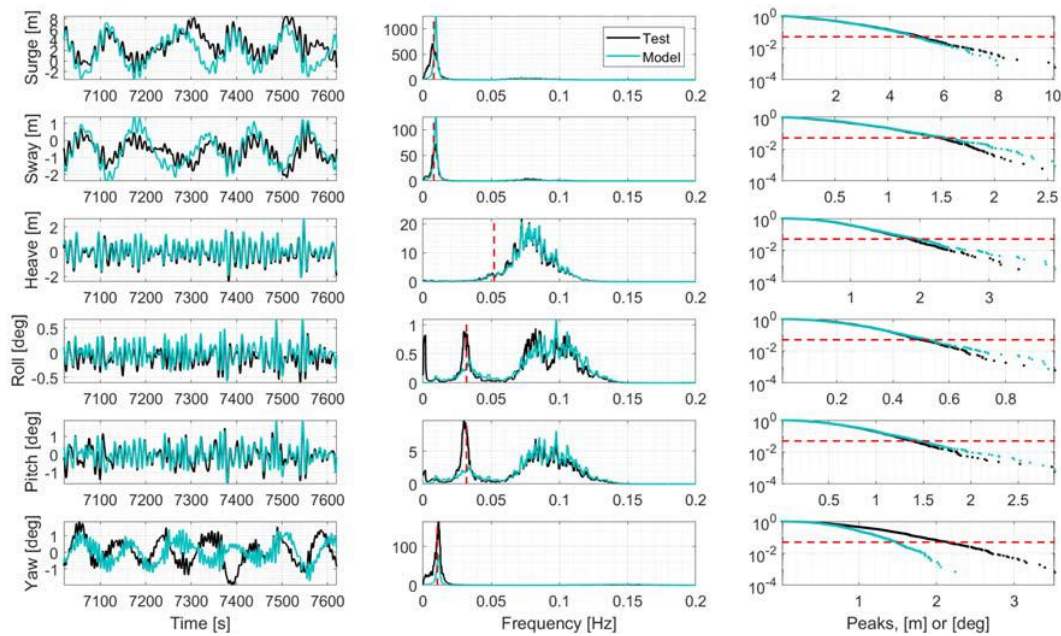


Figure 68: Time, frequency and exceedance probability plots for case M1.

Table 13: Results statistics for case M1.

	$\bar{\xi}_{test}$	$\bar{\xi}_{model}$	σ_{test}	σ_{model}	err. [%]	$\xi_{test}^{95\%}$	$\xi_{model}^{95\%}$	err. [%]
Surge [m]	3.03	1.86	2.38	2.14	-10.1	5.09	4.92	-3.3
Sway [m]	-0.64	-0.54	0.68	0.68	0.0	1.49	1.54	+3.4
Heave [m]	-0.10	0.06	0.73	0.73	0.0	1.85	1.96	+5.9
Roll [deg]	-0.11	-0.01	0.19	0.19	0.0	0.50	0.52	+4.0
Pitch [deg]	-0.09	-0.05	0.53	0.53	0.0	1.39	1.45	+4.3
Yaw [deg]	0.00	-0.02	0.96	0.59	-38.5	2.15	1.49	-30.7

Figure 69 and Table 14 show the response to the Pierson-Moskowitz sea state M2. The observations reported for M1 also apply to M2, with errors within 10% in the 95% percentile for sway, heave, roll and pitch. The yaw prediction keeps getting worse with increasing sea state severity, with errors in σ_6 above 50%. In this case, although $\zeta_1 = \zeta_2 = \zeta_6 = 0$ the standard deviation of surge, sway and yaw could not be matched, likely due to the combination of mooring drag damping and missing wave excitation. It is believed that this underprediction of wave excitation loads arises from the simplification of the QTFs (see Section 5.5), where the effect of the first-order motion on the second-order solution was neglected. As expected, the consequences of this approximation led to underprediction of the second-order wave excitation loads. The underprediction becomes more apparent as the sea state severity increases, given that the first-order motion also increases with the wave height. This effect is only obvious in the horizontal DoFs (surge, sway and yaw), because these are always dominated by resonance and thus are more sensitive to the prediction of second-order loads. Heave is always dominated by linear wave loads, and roll and pitch are only dominated by resonance for mild sea states (P1 and P2), whereas for M1 and M2 they are also largely influenced by linear wave loads.

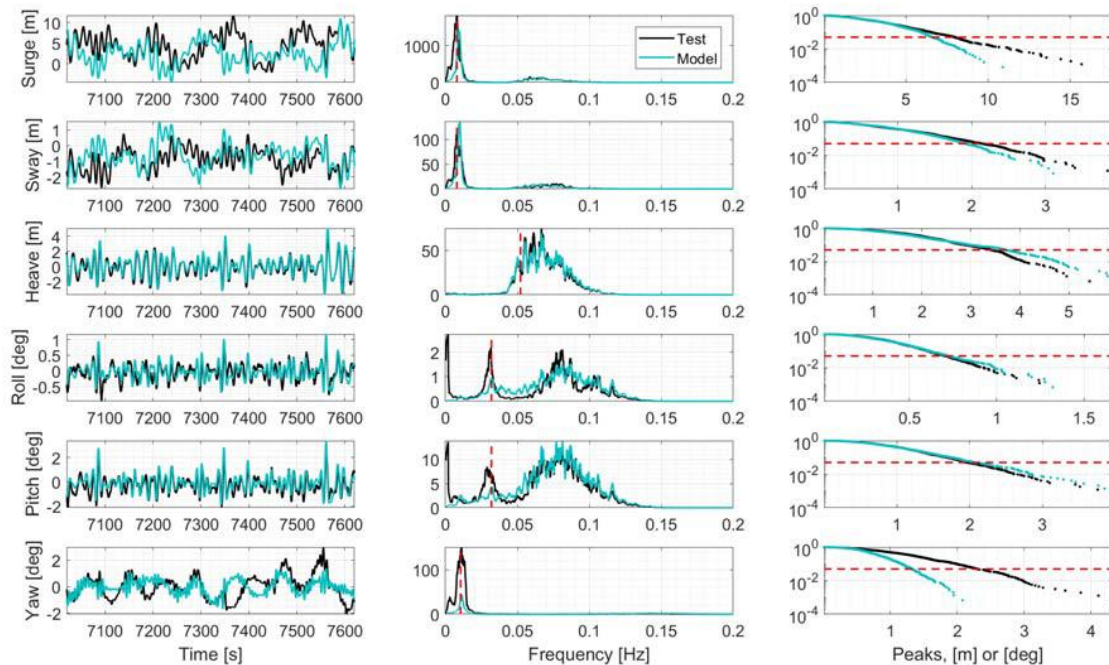


Figure 69: Time, frequency and exceedance probability plots for case M2.

Table 14: Results statistics for case M2.

	$\bar{\xi}_{test}$	$\bar{\xi}_{model}$	σ_{test}	σ_{model}	$err. [\%]$	$\xi_{95\%}^{test}$	$\xi_{95\%}^{model}$	$err. [\%]$
Surge [m]	4.05	1.99	3.64	2.92	-19.8	7.97	6.59	-17.3
Sway [m]	-0.80	-0.58	0.95	0.84	-11.6	2.13	1.93	-9.4
Heave [m]	-0.14	0.08	1.36	1.36	0.0	3.41	3.72	+9.1
Roll [deg]	-0.06	-0.01	0.27	0.27	0.0	0.71	0.72	+1.4
Pitch [deg]	-0.19	-0.04	0.76	0.76	0.0	1.95	2.06	+5.6
Yaw [deg]	0.03	-0.04	1.05	0.52	-50.5	2.29	1.32	-42.4

7.4.3 Mean-drift response

Figure 70 shows the measured and modelled mean-drift responses in surge and sway for the four sea states. The predictions are slightly overestimated for mild sea states P1 and P2, while considerably underestimated for sea states M1 and M2 (especially in surge, where the error is -51%). This underprediction is likely due to the missing second-order wave excitation loads associated to the simplification in the QTFs, as well as to viscous drag forces being integrated only up to $z = 0$ (see Section 7.3.6). Viscous mean drift is a third-order effect that occurs when the viscous forces are integrated up to the instantaneous free surface, or when they are applied to the instantaneous floater position (see Faltinsen [62]). Thus the model does not include these third-order effects.

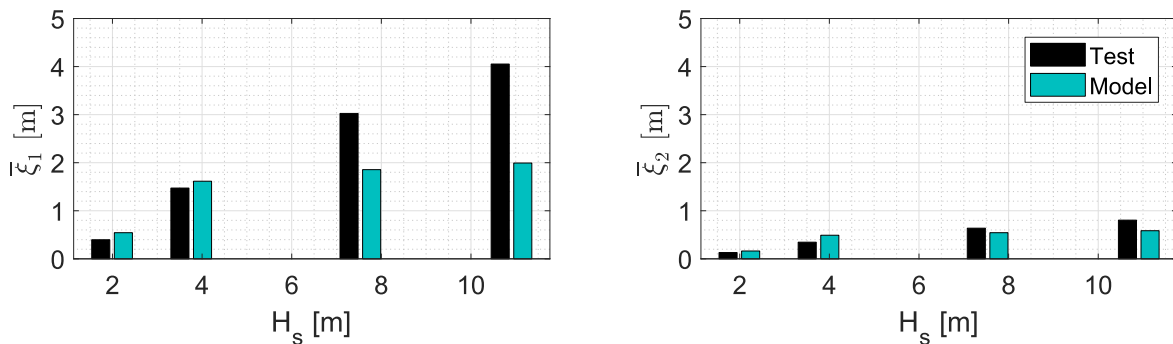


Figure 70: Mean-drift surge and sway responses for different sea states.

7.4.4 Comparison of OMA and calibrated damping

Figure 71 shows the damping ratios as a function of significant wave height. The damping ratios estimated with OMA (black) generally increase with H_s , as reported in Sall [52]. The increasing trend is clear for all modes but yaw up to M1, but a drop between the last two sea states is seen for surge, sway and heave. This observation can be linked to the assumptions OMA works under: i) linear system; ii) lightly-damped motions (10-15% damping); and iii) white noise excitation loads. The three assumptions are likely to be fulfilled for pink-noise mild sea states (P1 and P2). For Pierson-Moskowitz spectra (M1 and M2), however, assumption (iii) may only be fulfilled if the wave peak frequency is far enough from the system natural frequencies, which is more likely to be true for M1 than for M2. This is consistent with the observations reported in Ruzzo et al. [51]. Further, for case M2 (50-year sea state) the system is less likely to behave in a linear manner, thus (i) may also be violated. In other words, OMA may not be able to reliably detect the damping levels for M1 and M2. In addition, Bajrić et al. [63] reported that the damping estimated by OMA may not be reliable when the system has closely-spaced modes. This may also play a role in this case, since surge-sway and pitch-roll have the same natural frequencies due to symmetry.

The calibrated damping ratios (blue) are close to the OMA predictions for case P1. The prediction is worse for P2, and completely deviates for M1 and M2 in all DoFs. Here, the above discussion on the OMA assumptions and how they are less likely to be fulfilled for M1 and M2 is also applicable. In addition, the missing second-order wave excitation plays an important role here. As discussed above, neglecting the first-order motion in the computation of the QTFs leads to underprediction of the second-order loads for severe sea states, and its effect is more visible in the DoFs that are dominated by resonance — namely surge, sway and yaw. In a dynamic system, the same level of response can be maintained if both excitation and damping are reduced. In the model, the missing second-order wave loads for M1 and M2 are compensated by a drop in the damping level, as seen for surge and sway in the first two panels of Figure 71. The yaw DoF is missing excitation in all sea states, hence the best possible

match is obtained with $\zeta_6 = 0$, which still leads to underpredicted motion due to the damping effect of the mooring lines.

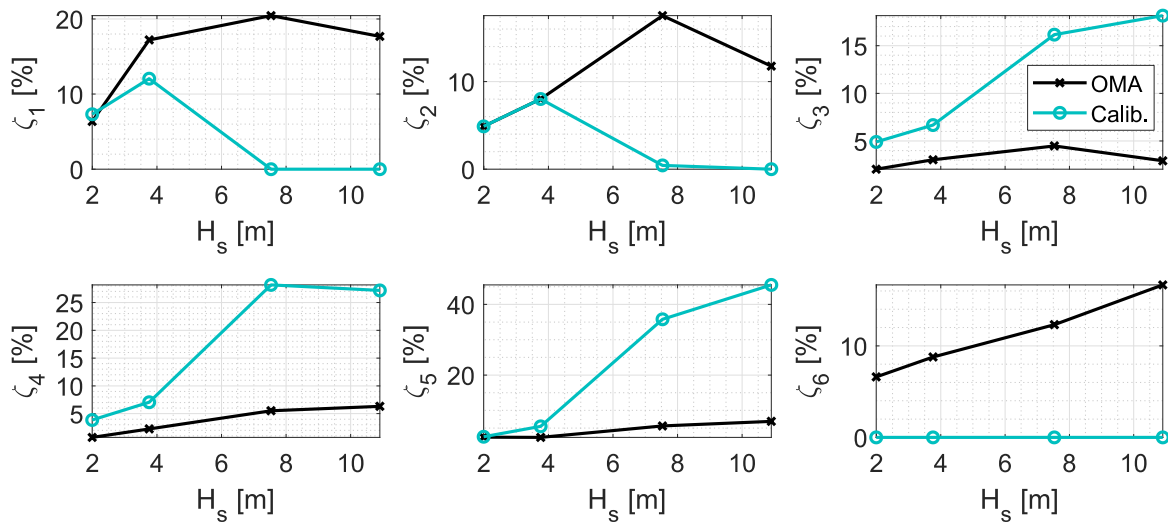


Figure 71: Damping ratios for different sea states, estimated with OMA and calibrated.

In operational cases with wind, however, the aerodynamic loads (which introduce both forcing and damping) are expected to dominate the low-frequency motion (see, for example, [64]), and may also change the applicability of OMA for estimation of damping properties.

7.5 Conclusions

Slow-drift forcing and damping are important for an accurate reproduction of the low-frequency motion of floating offshore wind turbines. Here we developed a numerical model that includes both inviscid slow-drift forcing through full QTF and viscous forcing. The model was set up to accommodate a linear damping matrix that represents all the damping effects on the floater. For that purpose, the classical Morison formulation of the drag forcing with relative velocity was simplified into a pure forcing term and a linear constant damping term, which can be calibrated to match the experiments. The linear damping representation enables a linear response formulation, which is attractive due to the easy calibration and later speed-up possibilities. Further, in the interest of numerical efficiency and with little error, the frequency-dependent radiation properties were replaced by constant added mass and damping matrices. Next, we investigated the possibilities of applying OMA to estimate the damping ratios. An alternative calibration of the damping ratios to fit the standard deviation of the measured response was further pursued. These damping ratios were identified and calibrated in the modal space, and later transformed to the physical space before applying them in the model.

The model was validated with wave basin data for four sea states with increasing severity, including the 50-year sea state. All the cases considered included waves misaligned with the structure's axes of symmetry, hence inducing three-dimensional response. Comparison to test data was made in terms of time series, PSD, and exceedance probability plots. The OMA damping estimates were found to be acceptable for the mild pink-noise sea states, while they needed significant calibration for the severe sea states with Pierson-Moskowitz spectra. For these cases no additional damping was needed in the horizontal degrees of freedom, since the damping induced by the mooring lines already produced underestimation of the response. Since the dynamic mooring description only included viscous damping

from the motion of the lines in calm water, we anticipated that the underpredicted response level is due to the neglect of the first-order motion effects in the applied QTFs.

For the operational sea state with $H_s = 7.7$ m, the damping calibration method of matching the standard deviation of the response gave quite good results with the surge motion being within 3.3% at the 95% quantile level. Similarly, heave and pitch was reproduced with a relative error of 5.9% and 4.3% respectively at the 95% level. The yaw response was always underpredicted, since even zero damping added in yaw implied an underprediction in yaw response. This underprediction even at zero added damping also occurred in the 50-year sea state of $H_s = 10.9$ m, where at the 95% quantile level a surge underprediction of 17.3% was obtained. At the same quantile, heave, pitch and yaw was obtained with a relative error of 9.1%, 5.6% and 42.4% respectively. As mentioned, the underpredictions are anticipated to be associated with the omission of certain QTF contributions. The error in the mean surge and sway responses was found to increase significantly with the sea state, likely due to missing third-order mean viscous loads in the model.

While calibration to the experiments is thus still needed, the linear format of the present model improved computational efficiency and was found capable of matching the response generally well, at least at the spectral and exceedance probability levels. The model can be further combined with more efficient ways of computing the QTFs found in the literature.

8 Validation of aerodynamic models

In the case of floating offshore wind turbines (FOWT) complexity in terms of aerodynamics of the wind turbine rotor is increased compared to fixed bottom wind turbines. This originates in the added 6 degrees of freedom of the platform which induce displacement and corresponding velocity and acceleration to the wind turbine rotor. Additional or more pronounced unsteady aerodynamic effects at the rotor are the result. For an efficient and accurate design of FOWT the aerodynamic loads must be calculated correctly requiring appropriate simulation tools. In this section, three different aerodynamic tools of varying fidelity are compared to measurement data acquired in a wind tunnel. It is aimed to identify aerodynamic phenomena occurring at FOWT and to give an estimation which tool fidelity gives the best results in the prediction of aerodynamic loads. This validation study is based on the deliverable “D4.7: Models for advanced load effects and loads at component level” from the LIFES50+ project [43]. In D4.7 the theoretical basis and methodology of the applied tools was presented.

8.1 Experimental Data Basis

The validation is based on experiments conducted at Politecnico di Milano within the LIFES50+ project and described in [65] and [66]. The setup consisted of a scaled version of the DTU 10MW [67] wind turbine which is referred as POLIMI 10MW – model scale (used scaling factors are $\lambda_L = 75$, $\lambda_v = 3$). The turbine was mounted on an actuator and could be moved in surge- and pitch-direction simulating the wave motions which are acting on the platform (Figure 72). In the experiments the aerodynamic thrust force of the rotor was measured building the data basis for this validation. Hence, all results are presented at model scale.

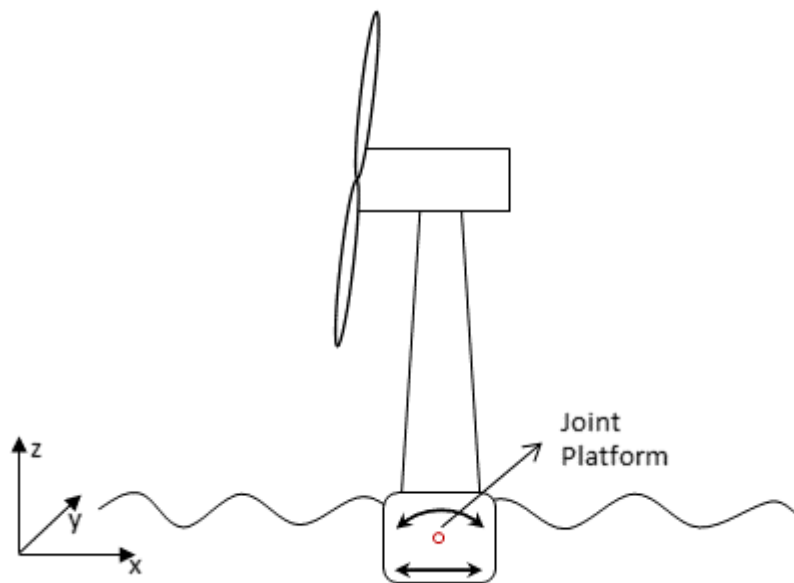


Figure 72: Schematic sketch describing degrees of freedom of platform for analysing aerodynamic effects

8.2 Simulation Model and Setup

The data of simulation model of the POLIMI 10MW – model scale can be found in [65]. The model with its structural properties was set up in the multi body simulation software SIMPACK. Hereby, turbine was modelled by using rigid bodies in order to isolate aerodynamic effects. This approach is considered to be reasonable because the experimental model was also built very stiff. On the aerodynamic side different models are used: Aerodyn v13 applying the generalized dynamic wake model (GDW) [68], ECN BEM based on the blade element momentum theory (BEM) and ECN AWSM which is a

Lifting-Line Free Vortex Wake (LL-FVM) code [69]. All investigated aerodynamic models are coupled to SIMPACK. The setup of the aerodynamic tools is listed in

. The underlying theory and the coupling to SIMPACK is explained in [43].

Table 15: Setup of aerodynamic tools for validation

Tool Setup	Aerodyn v13	ECN Aeromodule BEM	ECN Aeromodule AWSM
Time step	1deg rotor rotation per timestep		10deg rotor rotation per timestep
Finite number of blades	Generalized Dynamic Wake [68]	Prandtl Tip Loss	Intrinsic
Turbulent wake state		Linear Relationship tangential to quadratic relation of induction factor and thrust coefficient	Intrinsic
Dynamic inflow		ECN dynamic inflow model [70]	Intrinsic
Stall delay	3D correction model [71]	3D correction model [72]	
Dynamic stall	Not activated	Snel dynamic stall model [73]	

8.2.1 Analysis Method

The results are analysed by using the measure of the so-called dynamic thrust as defined by [65]. The term is used to describe the dynamic part of the thrust force meaning the portion of thrust force which is induced by the motion of the floating platform. The dynamic thrust is dependent on the velocity of the rotor hub. The shown plots of the dynamic thrust versus the rotor hub velocity can basically be described with the amplitude and area of hysteresis.

8.3 Model Check

8.3.1 Steady State Validation

In a first check the general capabilities of the models in reproducing the integral forces must be examined. Therefore, the thrust force of the rotor was measured for different operation points in the experiments at POLIMI [65].

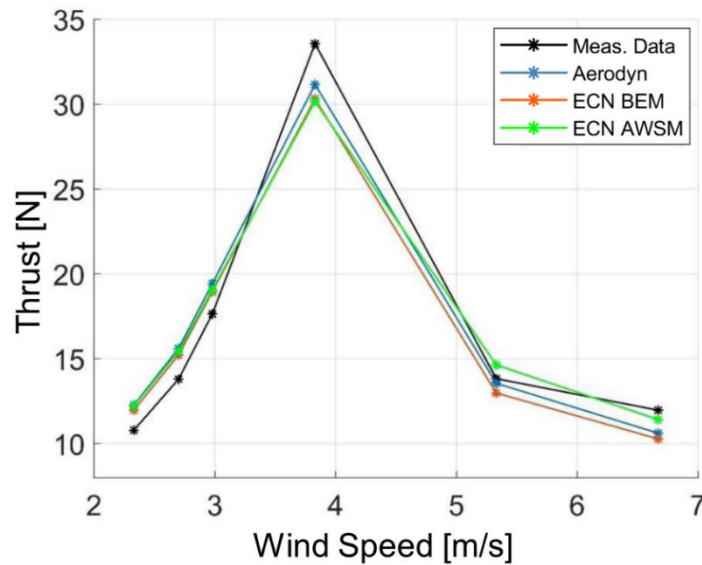


Figure 73 Comparison of thrust force for fixed platform

In Figure 73 the results of the different aerodynamic models are presented and compared to the measurement data. It can be seen that the tools are in good agreement to each other for wind speeds below 4 m/s (below rated). At above rated wind speeds, where blade pitch is active (see **Error! Reference source not found.**) the thrust force calculation of the tools is still close to each other but not as close as for below rated wind speeds. When compared to the measurement data the thrust force prediction of the tools is in acceptable agreement although there is a bigger discrepancy of about 10% at rated wind speed. Bearing these results in mind it is concluded that the tools are set up correctly and can be used for the unsteady calculations with a moving platform.

Table 16: Operational Points of POLIMI 10MW – model scale [66]

Wind Speed [m/s]	Blade Pitch Angle [°]	Rotor Speed [rpm]
2.33	0	150
2.70	0	161
2.98	0	181
3.83 (rated)	0	221
5.33	12.5	240
6.67	17.6	240

8.3.2 Free Vortex Wake Discretization

The results of a LL-FVM method are dependent on the discretization of the wake. The amount of wake points can be varied in the tool ECN AWSM with corresponding change in accuracy and calculation time. In order to verify that the solution is independent on the number of wake points two resolutions of the wake were investigated in Figure 74. It was found that a coarser discretization of the wake is sufficient for the calculation and hence is used for the studies in order to save computation time.

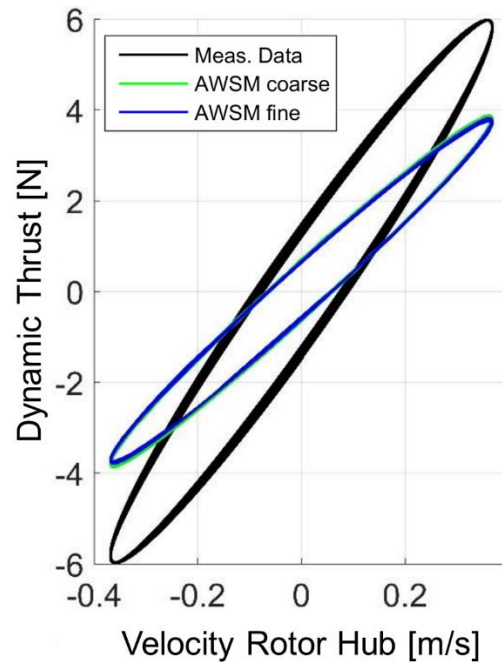


Figure 74: Influence of varying discretization of the wake within ECN AWSM, Platform pitch motion ($Frequency (F) = 0.65\text{Hz}$, $Amplitude (A) = 1^\circ$) above rated wind speed ($v_{wind} = 6.67\text{m/s}$)

8.4 Model Validation for Moving Platform

The model validation was conducted with isolated platform motions. The excitations of the platform were performed by using sinusoidal functions with different amplitudes and frequencies for surge and pitch direction. An overview of analysed motions is given in **Error! Reference source not found..**

Table 17: Overview of investigated platform motions

Motion	Amplitude	Frequency	Wind Speed [m/s]
Slow surge	0.1 m	0.25 Hz	2.33; 3.67; 5.33; 6.67
Fast surge	0.01 m	2.1 Hz	
Slow pitch	3°	0.65 Hz	
Fast pitch	1°	2.1 Hz	

8.4.1 Surge Motion of Platform

A comparison of the aerodynamic tools versus measurement data is made in Figure 75 for surge motions during below rated wind speed $v_{wind} = 2.33\text{m/s}$. In general, for this type of plots, amplitude and area of the hysteresis loop are of main interest for comparison (see also section 8.5.1). With that regard it is shown that the best agreement in both amplitude and area of hysteresis is reached between the LL-FVM code ECN AWSM and measurement data for the slower motion (Figure 75 left). The results of lower fidelity models Aerodyn and ECN BEM are in good agreement to each other but show discrepancies for the amplitude and area of hysteresis when compared to measurement data. For the faster excitation (Figure 75 right) all models show good agreement with measurement data.

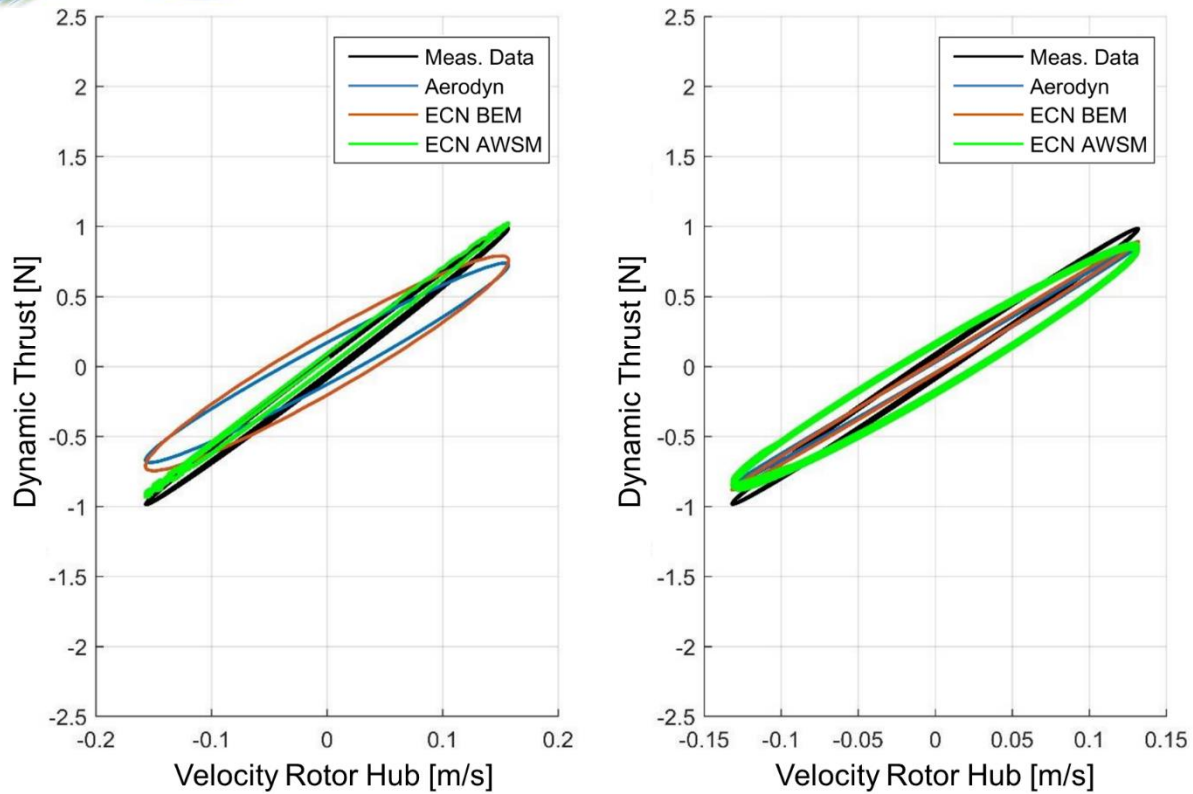


Figure 75: Comparison of measurement data and different aerodynamic tools for platform surge-motions
(left: $F = 0.25\text{Hz}$, $A = 0.1\text{m}$; right: $F = 2.1\text{Hz}$, $A = 0.01\text{m}$) below rated wind speed ($v_{wind} = 2.33\text{ m/s}$)

In Figure 76 it is focused on above rated wind conditions during surge motion of the platform where the blades are pitched by 17.6° . It is observed in the measurements that the faster motion (Figure 76 right) results in a large hysteresis loop whereas for the slower motion (Figure 76 left) hardly any hysteresis loop exists. This general feature is predicted by all aerodynamic tools qualitatively. In particular, the LL-FVM code ECN AWSM predicts the largest hysteresis loop compared to the other tools for the faster motion but is not able to match the measurement data. For the slower motion the best match in terms of amplitude is given by ECN AWSM. For both motions Aerodyn and ECN BEM are calculating nearly the same dynamic thrust.

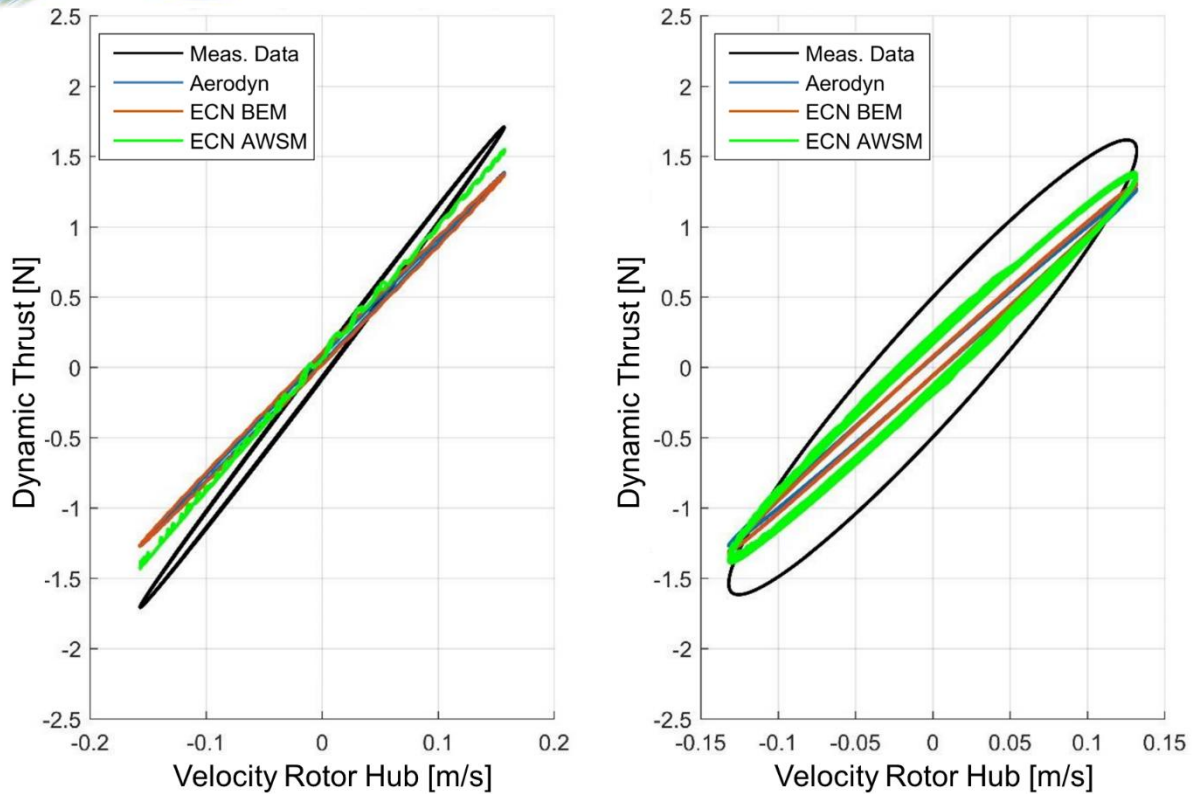


Figure 76: Comparison of measurement data and different aerodynamic tools for platform surge-motions (left: $F = 0, 25\text{Hz}$, $A = 0.1\text{m}$; right: $F = 2.1\text{Hz}$, $A = 0.01\text{m}$) above rated wind speed ($v_{wind} = 6.67\text{ m/s}$)

8.4.2 Pitch Motion of Platform

In additional tests the platform was moved in pitch direction during the wind tunnel experiments. The resulting dynamic thrust for a slow and fast pitch motion below rated wind is shown in Figure 77. It is observed that all aerodynamic tools are in good agreement to each other for the slower motion (Figure 77 left) but fail to predict the correct amplitude. Similar observations are made for the faster motion in Figure 77 right where again all tools are not able to calculate the amplitude measured in the experiments. However, discrepancy in terms of the area of hysteresis is observed between the LL-FVM method and the other tools Aerodyn and ECN BEM. Hereby, the LL-FVM method shows better agreement with the measurement data.

Figure 78 shows the results for platform pitch motion during above rated wind speeds. Basically, similar observations can be made compared to the cases at below rated wind speed. All considered tools are not able to calculate the amplitude of dynamic thrust as seen in the measurements. It is remarkable that ECN AWSM gives predictions in terms of the area of hysteresis for the faster pitch motion (Figure 78 right), which are closer to the measurement data. In this case, Aerodyn and ECN BEM are nearly not calculating any hysteresis which is more deeply investigated in section 8.5.3.

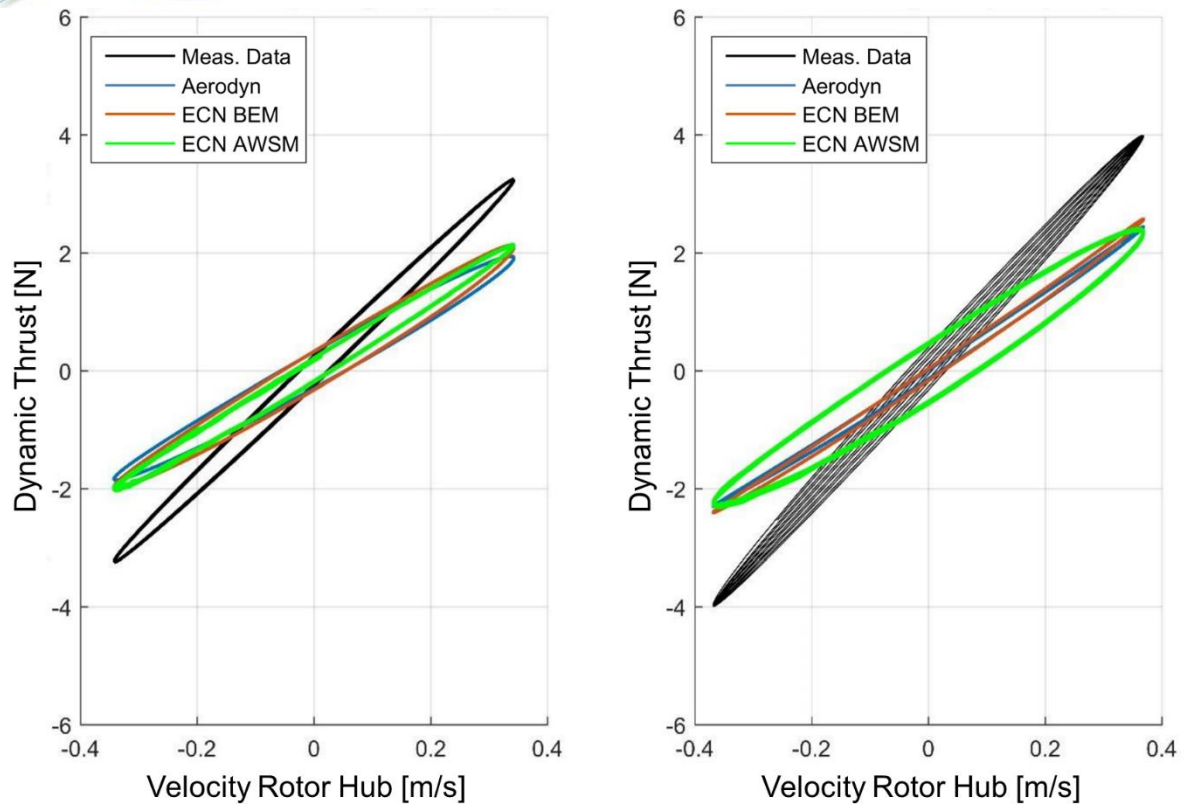


Figure 77: Comparison of measurement data and different aerodynamic tools for platform pitch-motions (left: $F = 0.65\text{Hz}$, $A = 3^\circ$; right: $F = 2.1\text{Hz}$, $A = 1^\circ$) below rated wind speed ($v_{\text{wind}} = 2.33\text{ m/s}$)

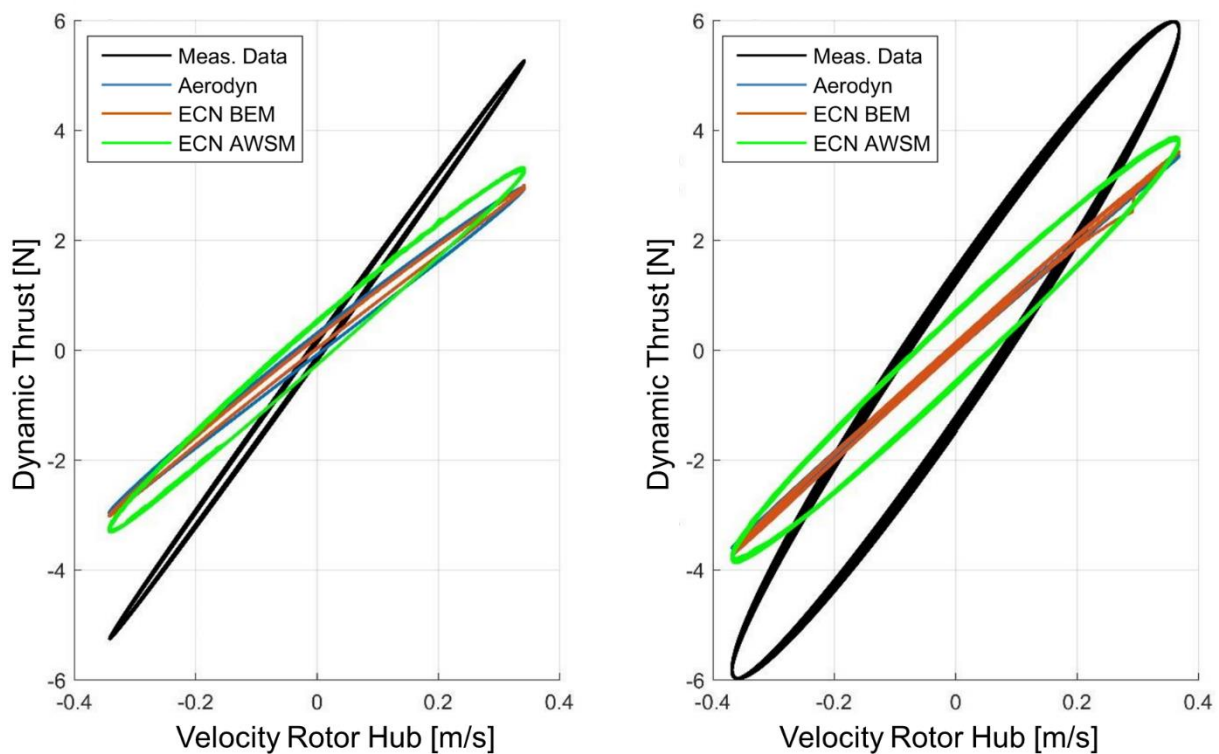


Figure 78: Comparison of measurement data and different aerodynamic tools for platform pitch-motions (left: $F = 0.65\text{Hz}$, $A = 3^\circ$; right: $F = 2.1\text{Hz}$, $A = 1^\circ$) above rated wind speed ($v_{\text{wind}} = 6.67\text{ m/s}$)

8.5 Identification of Phenomena

Multiple aerodynamic phenomena are relevant for the observations made in the model validation of the previous chapter. A few phenomena were picked for further analysis in the following section.

8.5.1 Dynamic Inflow

Dynamic inflow relates to the effect which occurs when the aerodynamic load at the wind turbine rotor changes unsteadily. In particular, higher structural loads and a delay in the structural response are observed when the aerodynamic load is changed instantly. In the case of the conducted experiments and the corresponding plots, dynamic inflow can be seen as a hysteresis loop in dynamic thrust and a change in amplitude compared to a steady variation of the rotor hub velocity. In order to illustrate dynamic inflow effect calculations were made with the lower fidelity tools Aerodyn and ECN BEM which offer the capability in turning on/off the dynamic inflow models; results are presented in Figure 79. It can be clearly seen that without activated dynamic inflow model no hysteresis of dynamic thrust is calculated. In contrast, having the dynamic inflow model activated hysteresis of dynamic thrust and a change in amplitude are predicted.

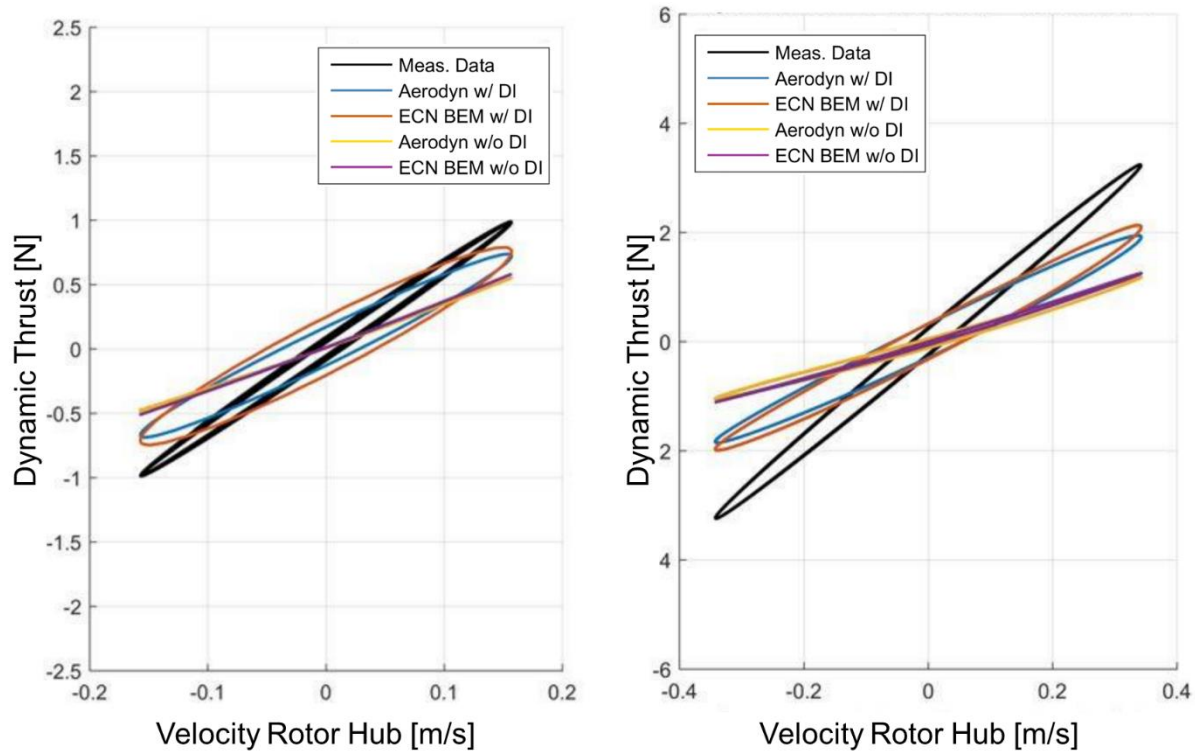


Figure 79: Comparison of measurement data and aerodynamic tools having dynamic inflow model active (w/ DI) and inactive (w/o DI), left (surge): $F = 0.25\text{Hz}$, $A = 0.1\text{m}$; right (pitch): $F = 0.65\text{Hz}$, $A = 3^\circ$ below rated wind speed ($v_{wind} = 2.33\text{m/s}$)

8.5.2 Dynamic Stall

Dynamic stall refers to a local phenomenon at the blade/airfoil itself where a dynamic change of angle of attack leads to increased lift forces followed by a hysteresis loop. Although dynamic stall plays a role at timescales below the investigated platform motions calculations with activated and deactivated dynamic stall model were performed for one surge motion at below rated wind speed. Hereby the mean value of angle of attack was around $\alpha_{AoA} = 4^\circ$. Figure 80 shows the results for the calculations with ECN AWSM and ECN BEM because in both tools a robust dynamic stall model [70] is implemented which is not requiring further airfoil parameters as it is the case for Aerodyn.

The plots in Figure 80 show not significant influence of the dynamic stall model on the dynamic thrust for both ECN BEM and ECN AWSM. However, slight improvement of the results with activated dynamic stall model is found when comparing to the measurement data. According to the authors further investigation regarding the dynamic stall effect especially for model scale wind turbines may be helpful in order to estimate the importance of dynamic stall for FOWT.

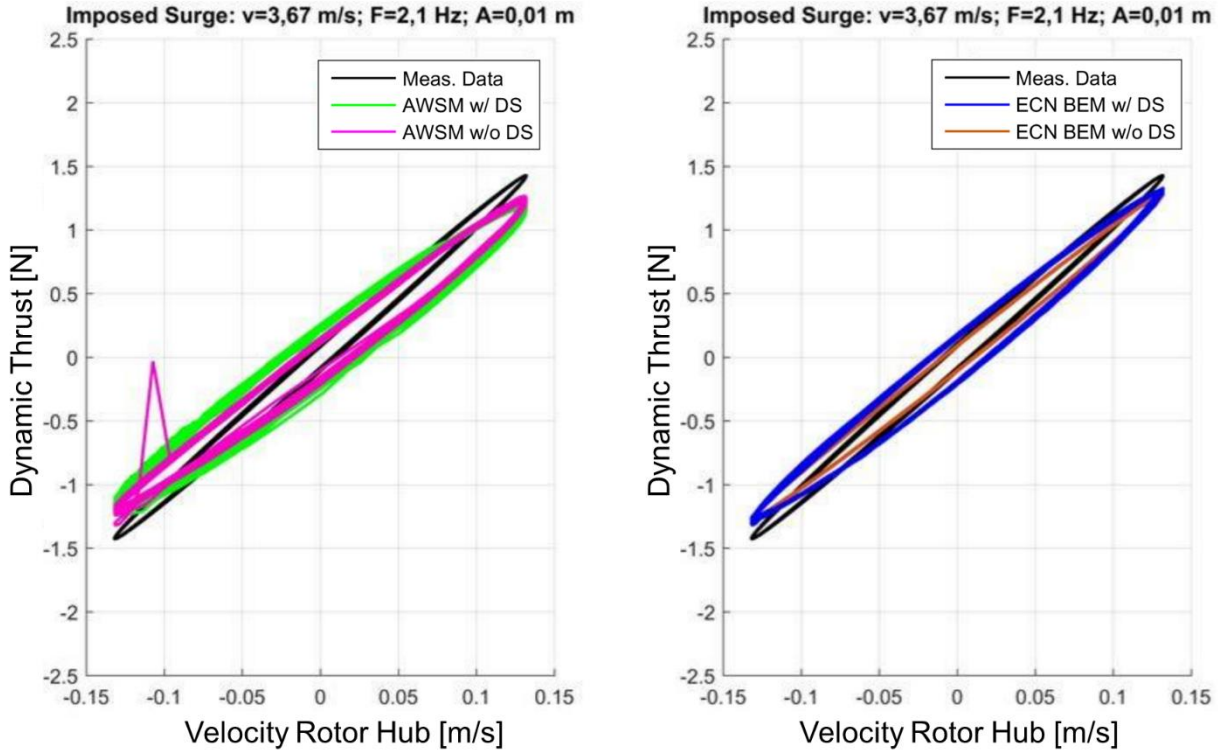


Figure 80: Comparison of measurement data and aerodynamic tools having dynamic stall model active (w/ DS) and inactive (w/o DS); left: ECN AWSM, right ECN BEM; surge motion with $F = 2.1 \text{ Hz}$, $A = 0.01 \text{ m}$, wind speed ($v_{\text{wind}} = 3.67 \text{ m/s}$)

8.5.3 Wake Reduced Velocity

A measure for characterising the unsteadiness of operational conditions for a FOWT is the so-called dimensionless wake reduced velocity (introduced in [74]) which is defined as:

$$V_W^* = \frac{U_\infty}{f * D}$$

where U_∞ is the incoming wind speed, f the frequency of motion and D the turbine diameter. Higher values (approximately $V_W^* > 5$) indicate steady or quasi-steady behavior. At low values of the wake reduced velocity (approximately $V_W^* < 5$) it is likely that an unsteady behavior exists where the wind turbine rotor is influenced by its own wake directly. In

the wake reduced velocity for operational conditions analyzed in chapter 8.4 is calculated.

Table 18: Calculation of the wake reduced velocity for investigated operational conditions

	Wind Speed [m/s]			
Frequency [Hz]	2.33	3.67	5.33	6.67
0.25	3.9	6.1	8.9	11.2
0.65	1.5	2.4	3.4	4.3
2.1	0.5	0.7	1	1.3

The results for a surge motion with a relatively low and high wake reduced velocity are shown in Figure 81. When analysing the results of the lower fidelity tools ECN BEM and Aerodyn the differences are clearly seen; for a low V_W^* the area of hysteresis is bigger than for the high V_W^* . Additionally, the amplitude for the high V_W^* is not changed when compared to a steady variation of the incoming wind speed. However, the lower fidelity tools are not able to predict the measurement data in the unsteady case whereas ECN AWSM shows good agreement with the measurement data.

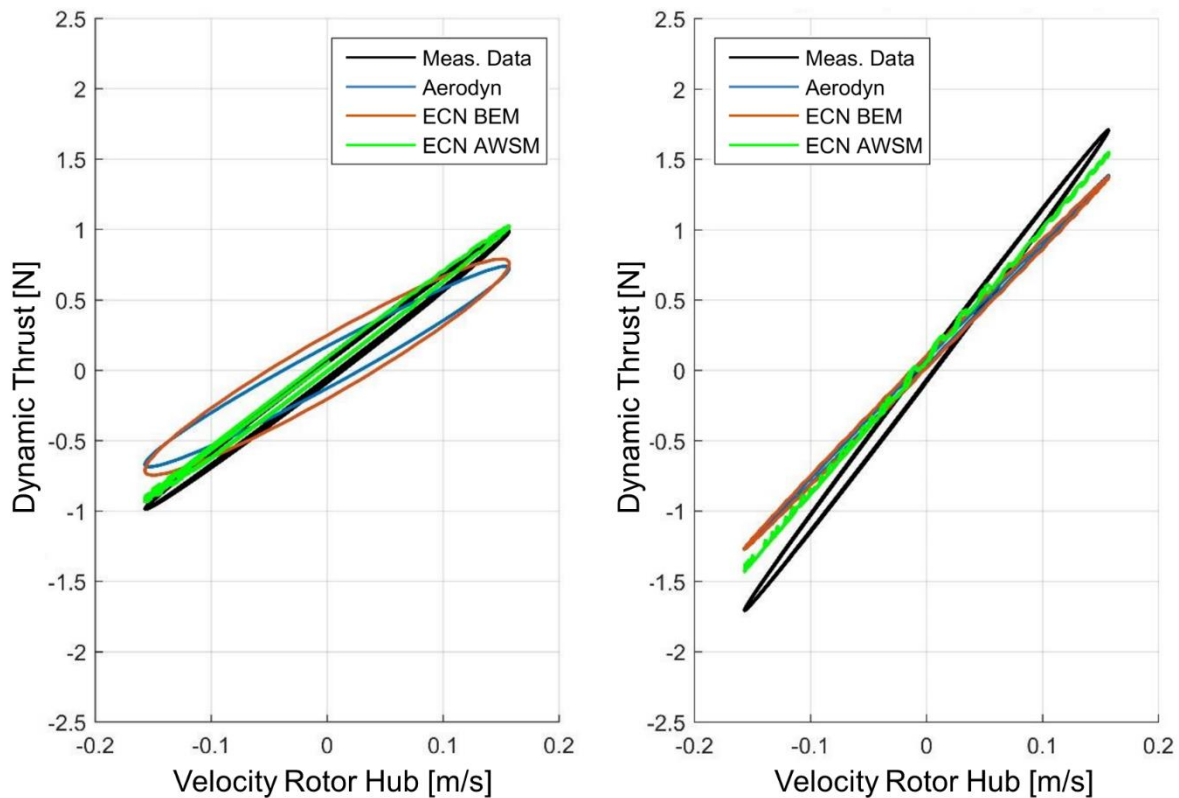


Figure 81: Influence of wake reduced velocity V_W^* on dynamic thrust for surge motion; left: $V_W^* = 3.9$, $F = 0.25\text{Hz}$, $A = 0.1\text{m}$, $v_{wind} = 2.33\text{m/s}$; right: $V_W^* = 11.2$, $F = 0.25\text{Hz}$, $A = 0.1\text{m}$, $v_{wind} = 6.67\text{m/s}$

In order to support the definition of the wake reduced velocity calculations were conducted where a low V_W^* was initiated (see Figure 82). There is a big discrepancy between the lower fidelity tools and ECN-AWSM. In the case of ECN AWSM a big hysteresis loop is calculated which cannot be seen in the results of Aerodyn and ECN BEM.

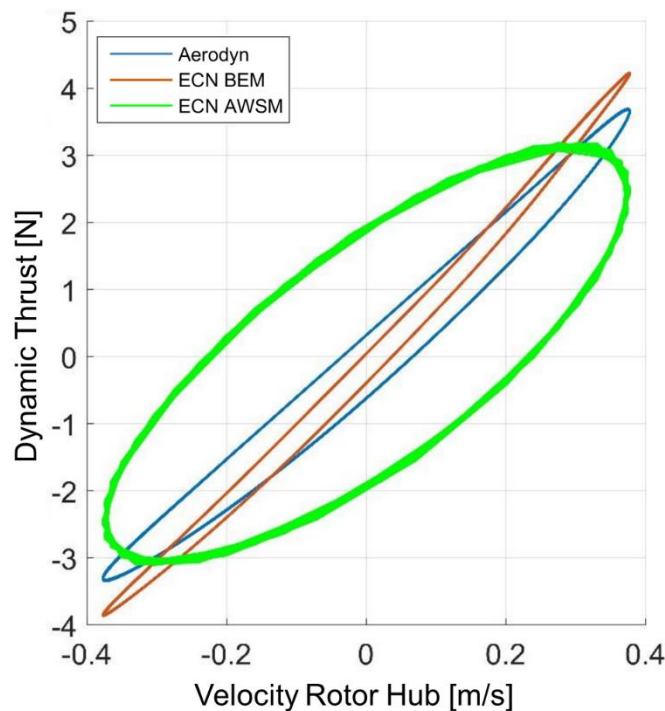


Figure 82: Comparison of aerodynamic tools for surge motion with increased oscillation frequency of platform, $V_W^* = 0.16$, $F = 6\text{Hz}$, $A = 0.01\text{m}$, $v_{wind} = 2.33\text{m/s}$

8.6 Simulation-Time

Besides result quality the tool choice is often dependent on the calculation time. In

average calculation times for the considered aerodynamic tools are presented. The simulations were run on a state-of-the-art CPU utilising one core. It is remarkable that the calculation time for ECN AWSM is much higher compared to the lower fidelity tools. The better results of ECN AWSM have a high price in terms of computational time. Due to the developing wake in the LL-FVM method the calculation time increases also with longer simulation times. However, it must be mentioned that the LL-FVM method offers a high parallelisation potential making it suitable for GPU-acceleration on many cores which eventually would drop the computational time drastically.

Table 19: Average simulation times for the different aerodynamic tools

Simulation time	Aerodyn	ECN BEM	ECN AWSM coarse	ECN AWSM fine
10s	1 min	4-5 min	5-7 h	12-15 h
20 s	2 min	6-7 min	12-15 h	35-40 h

8.7 Summary of Aerodynamic validation

Calculations of the aerodynamics at the rotor of a floating offshore wind turbine were made. In particular, the investigations were focused on the POLIMI 10MW – modelscale rotor for which wind tunnel measurement data exist; this includes especially data, where the platform was moved to simulate floating

platform motions due to waves. Aerodynamic tools of varying fidelity were used (low fidelity: Aerodyn, ECN BEM; higher fidelity: ECN AWSM) and coupled to the multi body simulation software SIM-PACK.

Overall it was found that the higher fidelity tool ECN AWSM delivers better agreement with the measurement data than Aerodyn and ECN BEM. In particular, distinctions must be made between platform surge motions and platform pitch motions. For platform surge motions ECN AWSM calculates results having good agreement with the measurement data even for operational states where highly unsteady aerodynamics are expected. In contrast, Aerodyn and ECN BEM are not able to predict the measurement results accurately for highly unsteady conditions. It was shown that most likely the dynamic inflow models fail in such conditions. For platform pitch motions, all tools are not able to calculate close results compared to the measurement data. Platform pitch motions are more complex compared to surge motions in terms of the aerodynamics at the rotor.

For future investigations it is recommended to further analyse platform pitch motions. Therefore, experiments with sensors for visualising the flow field and CFD-calculations can help to better understand the occurring phenomena. Additionally, dynamic stall effects should be analysed in more detail for creating more accurate input conditions for simulations.

9 Conclusions

We have presented the validation of different advanced models against generic or experimental data from the LIFES50+ project. Further, we have demonstrated methods for application of the advanced model results within models of lower CPU cost. The conclusions of the different studies are summarized below:

Validation of elastic modes against flexible monopile tests

The results show that, in a generic setting, the coupled HAWC2-WAMIT approach for flexible substructure modes is able to predict sectional loads in the substructure for irregular wave forcing. The model accuracy is limited due to the omission of nonlinear wave forcing effects and the omission of viscous drag loads. Despite these limitations, response outside of the primary wave spectrum was observed, thus illustrating that the flexible solver does predict dynamic response at the natural frequency of the structure.

Validation of second-order hydrodynamics in a state-of-the-art model of the OO-Star Wind Floater Semi 10MW

From the comparison study of the full second-order solution and the Newman's approximation, and using the same calibrated global diagonal damping matrices in both models, the responses are similar for mild sea states. However, it was also shown that for a more severe sea state the larger second-order loads introduced by the full QTF solution generally counteract the negative damping needed for the Newman-based model.

It was further shown how the 2nd-order wave forces calculated by the full second-order solution are much higher than the ones calculated from the Newman's approximation. This has a huge impact on the resonant responses located far from the diagonal in the QTF matrix. However, the surge response is matched very well by both models with only a slight difference in the calibrated damping ratio, and this is most likely related to the large natural period of surge (i.e. close to the diagonal in the QTF matrix).

A deviation in the heave and pitch responses was observed for DLC 6.1 (1), which might arise from an increased resonant motion in heave, which may be too far from the diagonal in the QTF matrix to be properly captured by the Newman approximation.

It was also observed that a faster calibration can be achieved if the damping matrix is calibrated by adjusting the modal damping ratios. However, both the modal approach and the approach where a diagonal linear damping matrix is calibrated are capable of reproducing the responses observed in the tests, if the calibration is properly done.

Validation of OpenFOAM CFD for the OO-Star Wind Floater Semi 10MW

The CFD setup was applied to a free heave decay test and showed a good match to the experimental results. An approximate mooring representation was developed and compared to the full mooring setup of a FAST model in a quasi-static setting. A regular wave forcing case was next compared to the model test results. The comparison includes the transient low-frequency response, where the floater is moved from its initial rest position towards the wave-drift driven offset. A good match in surge is seen for both the low-frequency transient and the motion at the primary wave frequency. For heave, a deviation in the low-frequency heave response was seen. This was discussed in terms of wave generation effects.

The effects of flow viscosity, turbulence modelling and wall boundary conditions was also demonstrated for selected test cases. Upon convergence, CFD simulations can give invaluable information on the flow physics.

Validation of second-order hydrodynamics in a state-of-the-art model of the NAUTILUS-DTU10

The use of difference-frequency full QTFs increased the response of the platform for the low-frequency region (below the wave excitation region), especially for pitch and roll, when compared to Newman's approximation. The response in this low-frequency region for the extreme irregular wave test was, however, below that of the experimental data for the model tuned to the decay tests. A better comparison was achieved for the surge and sway degrees of freedom under the pink noise test, but the simulation still under-predicted the low-frequency responses for the other degrees of freedom.

It was shown that, for tests with pink-noise waves, the model with the full QTFs can reproduce all the measured responses but yaw if the vertical drag coefficients are properly calibrated. Adjusting the drag coefficients, however, was not sufficient for complete replication of the response in all the platform degrees of freedom for the irregular wave tests and the pink-noise tests. For the extreme irregular wave case, it was also seen that as the vertical drag coefficients were reduced, the pitch response at the wave frequency range was also reduced. This is due to the fact that the Morison drag introduces both damping and forcing.

Validation of CFX for the NAUTILUS-DTU10

Forced heave oscillation tests using the MBS-CFD simulation environment was used to deliver added mass and damping coefficients. Predictions of added mass were in line with data from linear potential flow theory, like WAMIT. Damping includes viscous effects in CFD because of the nature of the underlying Navier-Stokes equations. Engineering models include Morison drag or global damping matrices for compensation of missing viscosity. The MBS-CFD analysis demonstrated the dependency of damping on oscillation amplitude and frequency. Grid resolution, temporal discretisation as well as solver parameters, like applied turbulence model for RANS simulation or time stepping scheme, influenced the numerical solution process and thus the derived hydrodynamic parameters like damping. Thus, it is crucial to perform sensitivity studies in CFD in advance for model calibration.

Decay tests in heave were performed and a good correlation to the experiment was found for the natural period. The damping behaviour of the MBS-CFD simulation can be increased by application of smaller time steps and better grid resolution, especially in the vicinity of the platform.

In general, the high-fidelity MBS-CFD methodology is suitable for determination of hydrodynamic characteristics, execution of design studies and assessment of extreme loads.

Damping detection by Operational Modal Analysis for the NAUTILUS-DTU10

The damping ratios were found to be acceptably predicted by Operational Modal Analysis for mild sea states, while they deviated from the calibrated values for larger sea states. This was linked to the assumption of white-noise forcing within the OMA theory, which is violated in the general wave-forcing case, where the natural frequency is placed outside the primary wave spectrum.

Both OMA-based and calibrated damping ratios were found to depend on the sea state. The model generally captured well the response after proper calibration of the damping. For larger sea states, the response in some degrees of freedom is under-predicted. This was linked to missing second-order inviscid loads and third-order viscous loads.

Validation of aerodynamic models

Overall it was found that the higher fidelity tool ECN AWSM delivers better agreement with the measurement data than Aerodyn and ECN BEM. In particular, distinctions must be made between platform surge motions and platform pitch motions. For platform surge motions ECN AWSM calculates results having good agreement with the measurement data even for operational states where highly unsteady aerodynamics are expected. In contrast, the BEM based methods are not able to predict the measurement results accurately for highly unsteady conditions. It was shown that most likely the dynamic inflow models fail in such conditions. For platform pitch motions, all tools are not able to calculate close results compared to the measurement data. Platform pitch motions are more complex compared to surge motions in terms of the aerodynamics at the rotor.

10 References

- [1] H. Bredmose, P. Slabiak, L. Sahlberg-Nielsen and F. Schlutter, “Dynamic Excitation of Monopiles by Steep and Breaking Waves: Experimental and Numerical Study,” in *Proc. ASME 2013 32nd International Conference on Ocean, Offshore and Arctic Engineering (OMAE 2013)*, Nantes, 2013.
- [2] H. Bredmose, J. Mariegaard, B. T. Paulsen, B. Jensen, S. Schløer, T. J. Larsen, T. Kim and A. M. Hansen, “The Wave Loads Project,” in *DTU Wind Energy, Report E-0045*, 2013.
- [3] A. N. Robertson, F. Wendt, J. M. Jonkman, W. Popko, M. Borg, H. Bredmose, F. Schlutter, J. Qvist, R. Bergua, R. Harries, A. Yde, T. A. Nygaard, J. B. de Vaal and L. Oggiano, “OC5 Project Phase Ib: Validation of Hydrodynamic Loading on a Fixed, Flexible Cylinder for Offshore Wind Applications,” *Energy Procedia*, vol. 94, pp. 82-101, 2016.
- [4] F. Madsen, A. Pegalajar-Jurado, H. Bredmose, R. Faerron-Guzman, K. Müller and F. Lemmer, “LIFES50+ D4.6: Model validation against experiments and map of model accuracy across load cases,” 2018.
- [5] M. Thys, H. S. Andersen, T. Landbø, G. P. Moran and J. G. Fernandez, “LIFES50+ D3.4: Ocean Basin Test Report,” SINTEF Ocean, 2018.
- [6] J. Pinkster, “Low-frequency second-order wave exciting forces on floating structures,” 1980.
- [7] A. Simos, F. Ruggeri, R. Watai, A. Souto-Iglesias and C. Lopez-Pavon, “Slow-drift of a floating wind turbine: An assessment of frequency-domain methods based on model tests,” *Renewable Energy*, vol. 116, pp. 133-154, 2018.
- [8] S. Gueydon, T. Duarte, J. Jonkman, I. Bayati and A. Sarmento, “Comparison of second-order loads on a semisubmersible floating wind turbine,” in *Proceedings of the ASME 33rd International Conference on Ocean, Offshore and Arctic Engineering (OMAE 2014)*, 2014.
- [9] J. Newman, *Marine hydrodynamics*, 3rd ed., The MIT Press, 1980.
- [10] C. Lee, “WAMIT Theory Manual,” Cambridge, Massachusetts, 1995.
- [11] J. Jonkman and B. Jonkman, “NWTC Information Portal (FAST v8),” 2016. [Online]. Available: <https://nwtc.nrel.gov/FAST8>.
- [12] T. Duarte, A. Sarmento and J. Jonkman, “Effects of second-order hydrodynamic forces on floating offshore wind turbines,” in *Proceedings of the 32nd ASME Wind Energy Symposium*, 2014.
- [13] L. Roald, J. Jonkman and A. Robertson, “The effect of second-order hydrodynamics on a floating offshore wind turbine,” 2014.



- [14] V. Matos, A. Simos and S. Sphaier, “Second-order resonant heave, roll and pitch motions of a deep-draft semi-submersible: Theoretical and experimental results,” *Ocean Engineering*, vol. 38, pp. 2227-2243, 2011.
- [15] P. A. Berthelsen, E. Bachynski, M. Karimirad and M. Thys, “Real-time hybrid model tests of a braceless semi-submersible wind turbine. Part III: Calibration of a numerical model,” in *Proceedings of the ASME 35th International Conference on Ocean, Offshore and Arctic Engineering*, Busan, Korea, 2016.
- [16] F. Lemmer, A. Pegalajar Jurado, W. Yu, M. Borg, R. Mikkelsen, P. W. Cheng and H. Bredmose, “The Triplespar campaign: Validation of a reduced-order simulation model for floating wind turbines,” Vols. Proceedings of ASME 2018 37th International Conference on Ocean, Offshore and Arctic Engineering, no. OMAE2018-78119, 2017.
- [17] M. Kvittem, P. Berthelsen, L. Eliassen and M. Thys, “Calibration of hydrodynamic coefficients for a semi-submersible 10MW wind turbine,” in *37th International Conference on Ocean, Offshore and Arctic Engineering*, Madrid, Spain, 2018.
- [18] A. Pegalajar-Jurado and H. Bredmose, “Reproduction of slow-drift motions of a floating wind turbine using second-order hydrodynamics and Operational Modal Analysis,” *Marine Structures* (in review), 2018.
- [19] S. Mayer, A. Garapon and L. S. Sørensen, “A fractional step method for unsteady free-surface flow with applications to non-linear wave dynamics,” *International Journal for Numerical Methods in Fluids*, vol. 28, no. 2, pp. 293-315, 1998.
- [20] N. G. Jacobsen, D. R. Fuhrman and J. Fredsøe, “A wave generation toolbox for the open-source CFD library: OpenFoam®,” *International Journal for Numerical Methods in Fluids*, vol. 70, no. 9, pp. 1073-1088, 2012.
- [21] N. Bruinsma, “Validation and Application of a Fully Nonlinear Numerical Wave Tank,” p. 144, 2016.
- [22] J. Palm, C. Eskilsson, G. M. Paredes and L. Bergdahl, “Coupled mooring analysis for floating wave energy converters using CFD: Formulation and validation,” *International Journal of Marine Energy*, vol. 16, pp. 83-99, 2016.
- [23] A. J. Dunbar, B. A. Craven and E. G. Paterson, “Development and validation of a tightly coupled CFD/6-DOF solver for simulating floating offshore wind turbine platforms,” *Ocean Engineering*, vol. 110, pp. 98-105, 2015.
- [24] O. S. Petersen and N. F. Heilskov, “State-of-the-Art and Implementation of Design Tools for Floating Wave Energy Converters Part 2: Implementation and Results,” no. March, 2015.
- [25] I. R. Arreba, “Computation of Nonlinear Wave Loads on Floating Structures,” no. July, 2017.
- [26] H. G. Weller and G. Tabor, “A tensorial approach to computational continuum mechanics using object-oriented techniques,” *Computers in Physics*, vol. 12, no. 6, pp. 620-631, 1998.

- [27] H. Rusche, "Computational Fluid Dynamics of Dispersed Two-Phase Flows at High Phase Fractions," Imperial College London, 2002.
- [28] A. Pegalajar-Jurado, H. Bredmose, M. Borg, J. G. Straume, T. Landbø, H. Andersen, W. Yu, K. Müller and F. Lemmer, "State-of-the-art model for the LIFES50+ OO-Star Wind Floater Semi 10MW floating wind turbine," *Journal of Physics: Conference Series*, 2018.
- [29] A. Pegalajar-Jurado, F. Madsen, M. Borg and H. Bredmose, "LIFES50+ D4.5: State-of-the-art models for the two LIFES50+ 10MW floater concepts," 2018.
- [30] W. Yu, K. Müller and F. Lemmer, "LIFES50+ D4.2: Public definition of the two LIFES50+ 10MW floater concepts," 2018.
- [31] J. Galván, M. Sánchez-Lara, I. Mendikoa, G. Pérez Morán, N. Vincenzo and R. Rodriguez Arias, "NAUTILUS-DTU10 MW Floating Offshore Wind Turbine at Gulf of Maine: Public numerical models of an actively ballasted semisubmersible," *Journal of Physics; Conference series*, Vols. 10.1088/1742-6596/1102/1/012015, 01 October 2018.
- [32] J. N. Newman, "Second-order, slowly-varying forces on vessels in irregular waves," in *Proceedings of International Symposium on Dynamics of Marine Vehicles and Structures in Waves*, London, 1974.
- [33] D. Matha, "Impact of aerodynamics and mooring system on dynamic response of floating wind turbines," 2016.
- [34] J. Azcona, "Computational and experimental modelling of mooring line dynamics for offshore floating wind turbines," 2016.
- [35] M. Thys, V. Chabaud, T. Sauder, L. Eliassen, L. O. Sæther and Ø. B. Magnussen, "Real-Time Hybrid Model Testing of a Semi-Submersible 10MW Floating Wind Turbine and Advances in the Test Method," in *Proceedings of the 1st International Offshore Wind Technical Conference*, 2018.
- [36] NWTC, *NWTC information portal (FAST v8)*, 2016.
- [37] M. Thys, "LIFES50+ D3.4: Ocean basin test report," 2018.
- [38] A. Robertson and a. et, "OC5 Project Phase II: Validation of Global Loads of the DeepCwind Floating Semisubmersible Wind Turbine," *Energy Procedia*, vol. 137, 01 10 2017.
- [39] F. Lemmer, W. Yu and P. W. Cheng, "Iterative frequency-domain response of floating wind turbines with parametric drag," *Journal of Marine Science and Engineering*, vol. 6, 2018.
- [40] T. Duarte, A. J. Sarmento and J. Jonkman, "Effects of Second-Order Hydrodynamic Forces on Floating Offshore Wind Turbines," in *AIAA SciTech*, National Harbor, U.S.A, 2014.
- [41] J. G. J. M. I. M. M. S. N. B. G. K. M. S. G. M. K. Azcona, "Models for offshore wind turbines (IRPWind project - PP deliverable No. 63.1), Work Package 6.3.," 2017.

- [42] J. M. J. Journée and W. W. Massie, “Offshore Hydromechanics,” Delft University of Technology, 2001.
- [43] M. Borg, A. Pegalajar-Jurado, H. Sarlak, F. Madsen, H. Bredmose, F. Lemmer and F. Borisade, “LIFES50+ D4.7: Models for advanced load effects and loads at component level,” 2018.
- [44] H. P. Piehl, “Ship Roll Damping Analysis,” 2016.
- [45] F. Borisade, T. Choynet and P. W. Cheng, “Design study and full scale MBS-CFD simulation of the IDEOL floating offshore wind turbine foundation,” *Journal of Physics: Conference Series*, vol. 753, p. 092002, 2016.
- [46] M. Arnold, Simulation and Evaluation of the Hydroelastic Responses of a Tidal Current Turbine, München: Verlag Dr. Hut, 2017.
- [47] R. Brincker and C. Ventura, Introduction to Operational Modal Analysis, 1st ed., Wiley, 2015.
- [48] S. Ibrahim and E. Mikulcik, “A method for direct identification of vibration parameters from the free response,” *The Shock and Vibration Bulletin*, vol. 47, pp. 183-196, 1977.
- [49] S. Ibrahim, “Random decrement technique for modal identification of structures,” *Journal of Spacecraft and Rockets*, vol. 14, no. 11, pp. 696-700, 1977.
- [50] S. Ibrahim, “Modal confidence factor in vibration testing,” *Journal of Spacecraft and Rockets*, vol. 15, no. 5, pp. 313-316, 1978.
- [51] C. Ruzzo, G. Failla, M. Collu, V. Nava, V. Fiamma and F. Arena, “Operational Modal Analysis of a spar-type floating platform using Frequency Domain Decomposition method,” *Energies*, vol. 9, 2016.
- [52] P. W. Sall, *Modal identification of damping for floating wind turbines. MSc thesis, DTU.*, 2017.
- [53] C. Ruzzo, G. Failla, M. Collu, V. Nava, V. Fiamma and F. Arena, “Output-only identification of rigid-body motions of floating structures: a case study,” *Procedia Engineering*, vol. 199, pp. 930-935, 2017.
- [54] V. Nava, J. Galván, M. Sánchez-Lara, C. Garrido-Mendoza, G. Pérez-Morán, M. Le Boulluec, B. Augier and R. Rodríguez-Arias, “Hydrodynamic identification of NAUTILUS FOWT platform from small-scale tests,” in *Proceedings of RENEW2018*, 2018.
- [55] A. Krieger, G. Ramachandran, L. Vita, G. Gómez-Alonso, J. Berque and G. Aguirre, “LIFES50+ D7.2: Design basis,” 2015.
- [56] M. Hall, “MoorDyn,” 2017. [Online]. Available: <http://www.matt-hall.ca/moordyn.html>.
- [57] W. Cummins, “The impulse response functions and ship motions,” *Schiffstechnik*, vol. 9, pp. 101-109, 1962.

- [58] T. Ogilvie, “Recent progress toward the understanding and prediction of ship motions,” in *Fifth Symposium on Naval Hydrodynamics*, 1964.
- [59] C. Lee and J. Newman, “WAMIT,” 2016. [Online]. Available: <http://www.wamit.com/>.
- [60] J. Morison, J. Johnson and S. Schaaf, “The force exerted by surface waves on piles,” *Journal of Petroleum Technology*, vol. 2, no. 05, pp. 149-154, 1950.
- [61] G. Airy, “Tides and waves,” *Encyclopaedia Metropolitana, Tom. V*, pp. 241-396, 1845.
- [62] O. Faltinsen, *Sea loads on ships and offshore structures*, Reprint ed., Cambridge University Press, 1993.
- [63] A. Bajrić, J. Høgsberg and F. Rüdinger, “Evaluation of damping estimates by automated Operational Modal Analysis for offshore wind turbine tower vibrations,” *Renewable Energy*, vol. 116, pp. 153-163, 2018.
- [64] A. Coulling, A. Goupee, A. Robertson and J. Jonkman, “Importance of second-order difference-frequency wave-diffraction forces in the validation of a FAST semi-submersible floating wind turbine model,” in *Proceedings of the ASME 32nd International Conference on Ocean, Offshore and Arctic Engineering (OMAE 2013)*, 2013.
- [65] I. Bayati, M. Belloli and L. Bernini, “LIFES50+ D3.1: AeroDyn validated model,” 2016.
- [66] I. Bayati, M. Belloli and L. Bernini, “LIFES50+ D3.2: Wind turbine scaled model,” 2016.
- [67] Bak C, Zahle F, Bitsche R, Kim T, Yde A, Henriksen L C, Natarajan A, Hansen M, , “Description of the DTU 10 MW Reference Wind Turbine,” *DTU Wind Energy Report-I-0092*, 2013.
- [68] P. J. Moriarty and A. C. Hansen, “AeroDyn Theory Manual (NREL/EL-500-36881),” 2005.
- [69] F. Grasso, J. G. Schepers and A. van Garrel, “Development and Validation of Generalized Lifting Line Based Code for Wind Turbine Aerodynamics,” *49th AIAA Aerospace Sciences Meeting, 30th ASME Wind Energy Symposium*, 2011.
- [70] H. Snel and J. G. Schepers, “JOULE1: Joint investigation of Dynamic Inflow Effects and Implementation of an Engineering Model,” ECN, 1994.
- [71] Z. Du and M. Selig, “A 3-D stall-delay model for horizontal axis wind turbine performance prediction,” *AIAA-98-0021*, 1997.
- [72] B. Montgomerie, A. Brand, J. Bosschers and R. Van Rooij, “Three-Dimensional Effects in Stall. Report ECN-C-96-079,” ECN, 1996.
- [73] H. Snel, “Heuristic modelling of dynamic stall characteristics,” *European Wind Energy conference*, pp. 429-433, 1997.

- [74] I. Bayati, M. Belloli, L. Bernini and A. Zasso, “Wind Tunnel Wake Measurements of Floating Offshore Wind Turbines,” *14th Deep Sea Offshore Wind R&D Conference, EERA DeepWind’2017*, pp. 214-222, 2017.